

Air Flow Through Permeable Alkali Activated Ground Granulated Blast Furnace Slag Concretes

By:

Tristan Chauvin-Bossé

Department of Bioresource Engineering

Faculty of Agricultural and Environmental Sciences

McGill University, Montreal



A thesis submitted to McGill University in partial fulfillment of the requirements of Master of Science.

© Tristan Chauvin-Bossé

Table of Contents

I. List of Figures.....	4
II. List of Tables.....	5
III. Abstract.....	6
IV. Résumé	8
V. Acknowledgments.....	10
VI. Contribution to Original Knowledge	11
VII. Contribution of the Authors	11
1. Literature Review.....	12
1.1. Introduction.....	12
1.2 Vegetation Porous Concrete	14
1.3 Permeability	15
1.4 Cements and Pozzolans.....	17
1.5 Alkali Activated Blast Furnace Slag (AGBFS)	18
1.6. Water to Binder Ratio	21
1.7. Air Drying of Porous Concretes	23
1.8. Conclusion	25
2. Effect of Water to Binder ratio on the Hydration of Slag Cements.....	27
2.0. Abstract.....	27
2.1. Introduction.....	27
2.2. Materials and Methods.....	28
2.2.1.: Alkali Activated Slag Cylinders	28
2.2.2.: Calcium Silicate Hydrate (C-S-H) Seed Preparation.....	30
2.2.3.: Monitoring the Temperature of Cement Cylinders.....	30
2.2.3.: Compressive Strength.....	30
2.3. Results.....	32
2.4. Discussion	34

2.5. Conclusion	36
Connecting Statement for Chapter 3.....	37
3. Air Permeability of Bio-receptive Porous Concrete Slabs and Cylinders	38
3.0. Abstract.....	38
3.1. Introduction.....	38
3.2. Materials and Methods.....	39
3.2.1. Quartz aggregate	39
3.2.2. Permeable Alkali Activated Concrete.....	40
3.2.3. Porosity	40
3.2.4. Bulk Density	41
3.2.5. Experimental Setup, Data Collection and Permeability	41
3.2.6: Biological Clogging.....	44
3.3. Results.....	48
3.3.1. Porosity	48
3.3.2. Air Permeability.....	49
3.3.3. Biological Clogging.....	52
3.4. Discussion	53
3.5. Conclusion	56
Connecting Statement for Chapter 4.....	57
4. The Effect of Water to Binder Ratio on the Permeability of Porous Concretes	58
4.0. Abstract.....	58
4.1. Introduction.....	58
4.2. Materials and Methods.....	59
4.3. Results.....	60
4.4. Discussion	62
4.5. Conclusion	64
Connecting Statement for Chapter 5.....	64

5. Flow Through Air-Drying of Porous Concretes	65
5.0. Abstract	65
5.1. Introduction.....	65
5.2. Materials and Methods.....	66
5.3. Results.....	68
5.4. Discussion	70
5.5. Conclusion	72
Connecting Statement for Chapter 6.....	73
6: Prototypes of Porous Concretes for Heating and Ventilation.....	74
6.0. Abstract	74
6.1. Introduction.....	74
6.2. Materials and Methods.....	75
6.2.1. Heated Porous Concrete Slabs	75
6.2.2. Evaporative Cooling from Porous Concrete Slabs	75
6.3. Results.....	76
6.3.1. Heated Porous Concrete.....	76
6.3.2. Evaporative Cooling from Porous Concrete Slab.....	77
6.4. Discussion	77
6.4.1. Heated Porous Concrete.....	77
6.4.2. Evaporative Cooling from Porous Concrete Slabs	78
6.5. Conclusion	79
Final Conclusions and Summary	80
References.....	81
Appendix.....	92

I. List of Figures

Figure 1.1.1: Cross-sectional cut of porous concrete impregnated with epoxy resin.

Figure 1.5.1: Schematic representation of hydration models for alkali-slag cements.

Figure 1.7.1: Distribution of a wetting (water) and a non-wetting (air) fluid in the pore space of a porous medium.

Figure 2.2.1: BET and BJH desorption of slag.

Figure 2.2.2: Particle size distribution of slag.

Figure 2.2.3: Experimental setup for the determination of strength and hydration temperature of cement cylinders.

Figure 2.3.1: Average 20-hour compressive strength of alkali activated slag cylinders.

Figure 2.3.2: Hydration kinetics of alkali activated ground blast furnace slag.

Figure 3.2.1: Quartz aggregate used to make the porous concrete samples.

Figure 3.2.2: Geometry and physical appearance of porous concrete slabs.

Figure 3.2.3: Experimental Setups (wind tunnels) used for measuring permeability.

Figure 3.2.4: Grass grown under high pressure sodium lighting.

Figure 3.2.5: Vertically grown grass on permeable alkali activated porous concrete.

Figure 3.3.1: Non-Darcy flow in alkali activated granulated blast furnace slag porous concretes.

Figure 3.3.2: 95 % confidence intervals for second order polynomial regressions.

Figure 3.3.3: Biological clogging of bio-receptive porous concrete samples by turfgrass.

Figure 3.4.1: View from underneath slab and cross section of roots after drying.

Figure 3.4.2: Stem and leaf plots for the pressure drop and velocity data in the range of 0.2 to 0.5 m s^{-1} .

Figure 4.2.1: Mix design and visual appearance of porous concrete at varying water to binder ratio.

Figure 4.3.1: Porosity and bulk density of porous concretes made using two different water to binder ratios.

Figure 4.3.2: The effect of w/b on the permeability of alkali activated porous concrete.

Figure 5.1.1: Microstructural profile of interfacial transition zone (quartz – alkali activated slag).

Figure 5.3.1: Removal of hydration water from alkali activated porous concrete (sample M2S2).

Figure 5.3.2: Removal of water from porous concrete sample (M2S2) after being submersed in water for 15 minutes.

Figure 5.3.3: Removal of water retained in porous concrete sample (M2S2) after being submersed in water for 1 hour.

Figure 5.3.4: Removal of water retained in porous concrete sample (M2S2) after being submersed in water for 1 day.

Figure 5.4.1: Evaporation of hydration water from an alkali activated porous concrete slab being aspirated.

Figure 6.3.1: Temperature difference of outlet and inlet air flowing through a heated porous concrete slab.

Figure 6.3.2: Evaporative cooling from a porous concrete slab.

Figure 6.4.1: Porous concrete heat exchanger concept.

Figure A.1: Comparison of permeabilities obtained for various mixes of porous concretes to published values for sphere packs.

Figure A.2: Experimental setup for the growth of grass on porous concrete.

II. List of Tables

Table 2.2.1: Chemical analysis of slag by X-ray fluorescence (XRF).

Table 2.3.1: Mix designs and performance of alkali activated slag.

Table 2.3.2: One-way ANOVA post-hoc test multiple comparisons (Tukey's honest significance test (Tukey's HSD) for alkali activated slag cement cylinders at varying w/b.

Table 2.3.3: Tests of normality for compressive strengths for all 12 observations.

Table 2.3.4: Tests of normality for compressive strengths of the 9 unseeded observations.

Table 3.2.1: 2D image analysis of top projections of 42 aggregate particles.

Table 3.2.2: Mix design for porous concretes made with alkali activated slag.

Table 3.3.1: Image processing of porous concrete cross-sections.

Table 3.3.2: The Kruskal-Wallis H test for pressure drop and average cross-sectional velocity.

Table 3.3.3: Physical properties of porous concrete samples.

Table 4.3.1: Properties of porous concrete samples with two different w/b ratios.

Table 5.3.1: Water remaining in alkali activated porous concrete samples after being sealed cured for 4 months.

Table A.1: Descriptive Statistics for alkali activated porous concrete cylinders made using different w/b.

Table A.2: One-way analysis of variance (ANOVA) for alkali activated porous concrete cylinders at varying w/b.

Table A3: Data used in Chapter 3's independent-samples Kruskal-Wallis test.

III. Abstract

Porous concrete can be used as a building material and in the soilless (hydroponic) culture of plants. Aqueous plant nutrients are supplied to roots which grow into the void content of the concrete. The optimal use of porous concrete can be determined from a study of its material properties. Porosity, permeability and bulk density of concretes made using quartz aggregate cemented with alkali activated blast furnace slag are quantified.

For this thesis, the flow of air through bio-receptive permeable concrete is investigated. Grass was grown on various inclines (0-90 degrees) over surface areas ranging from 0.0225 m² to 0.250 m² with thicknesses from 0.05 m to 0.07 m. Chapters 5 and 6 include experiments on air movement with a system for air drying and heat exchange.

The relevant findings included in the following chapters are as follows. Granulated blast furnace slag cement cylinders reached compressive strengths of ~ 25 MPa after 20 hours when activated with a solution of 6 % NaOH and 12 % sodium silicate (percent mass of binder) at a water to binder ratio (w/b) of 0.25. At a water to binder ratio of 0.30 and 0.35, compressive strengths of alkali activated slag cylinders reached approximately 17 MPa. After 40 days of growing turfgrass in bio-receptive porous concrete, the material's air permeability decreased by approximately 28 %. The inverse of permeability and the form drag (inertial resistance) of 0.5 m by 0.5 m by 5 cm thick porous concrete slabs using air was evaluated at $122 * 10^6 \text{ m}^{-2}$ & $5.24 * 10^4 \text{ m}^{-1}$, $117 * 10^6 \text{ m}^{-2}$ & $1.83 * 10^4 \text{ m}^{-1}$, and $75 * 10^6 \text{ m}^{-2}$ & $1.31 * 10^4 \text{ m}^{-1}$ for porosities of 0.26, 0.33, and 0.37, respectively. Increasing the water to binder ratio of this type of concrete from 0.25 to 0.35 decreased the inertial resistance (i.e. increased permeability) by a factor of 2. The water evaporation from porous concrete subjected to flow through drying (at a pressure drop of 8 hPa with air at 25 % relative humidity and a temperature of 22 °C) after being submersed in water for varying amounts of time indicated that the diffusion from the porous concrete's binder is dependent on submersion time and relates to the infiltration of water into the binder's micro and meso porosity. The volumetric heat-capacity of bio-receptive porous concrete was measured to be ~ 1380 kJ m⁻³ °C⁻¹ using two different methods: an equation relating mix ratios to heat capacities of individual mix components reported in the literature, and another using an energy balance equation on a heated slab subjected to an airflow cooling it.

These findings describe the potential uses for porous concrete in heating, ventilating, and air conditioning systems. The methods used along with the permeability values for various alkali activated porous concrete mixes documents a framework for the future integration of porous concrete into building systems.

IV. Résumé

Le béton poreux peut être utilisé pour la culture de plantes hors sol (hydroponie). Une solution aqueuse fournit les nutriments aux racines qui poussent dans les pores du béton. Cette pratique est optimisée par une compréhension des propriétés des matériaux. La porosité, l'imperméabilité et la masse volumique du béton formé par l'agrégat de quartz cimenté avec du laitier de haut fourneau activé aux alcalis sont quantifiées.

Cette thèse étudie le flux d'air à travers le béton poreux bio-réceptif. Du gazon a été cultivé à diverses inclinaisons (0 - 90 degrés) sur des surfaces variant de 0.0225 m² à 0.0250 m² et d'épaisseurs variant de 0.05 à 0.07 m. Les deux derniers chapitres présentent des expériences sur le mouvement d'air avec un système pour le séchage d'air et le transfert de chaleur.

Les principales conclusions présentées dans les chapitres sont les suivantes. Des cylindres de ciment de laitier de haut fourneau ont supporté des forces compressives de ~ 25 MPa après une période de durcissement de 20 heures quand activés avec une solution de 6 % NaOH et 12 % silicate de sodium (pourcentage de masse de liant) avec un ratio eau/liant (w/b) de 0.25. À des ratios w/b de 0.3 et 0.35, les forces supportées étaient de 17 MPa. La croissance de gazon sur le béton poreux bio-réceptif pendant 40 jours a résulté en une diminution d'environ 28 % de la perméabilité à l'air du matériel. L'inverse de la perméabilité et la traînée de forme (résistance inertielle) des dalles de béton poreux de 0.5 m par 0.5 m par 0.05 m, en utilisant l'air comme fluide, ont été évaluées à $122 * 10^6 \text{ m}^{-2} \& 5.24 * 10^4 \text{ m}^{-1}$, $117 * 10^6 \text{ m}^{-2} \& 1.83 * 10^4 \text{ m}^{-1}$, et $75 * 10^6 \text{ m}^{-2} \& 1.31 * 10^4 \text{ m}^{-1}$ pour des porosités de 0.26, 0.33 et 0.37 respectivement. L'augmentation du ratio w/b pour ce type de béton de 0.25 à 0.35 diminue la résistance inertielle par un facteur de 2. L'évaporation de l'eau contenue dans le béton poreux soumis à un flux d'air (chute de pression de 8 hPa, air à 25 % d'humidité relative et 22 °C) après avoir été submergé dans de l'eau pour différentes périodes de temps dénote que la diffusion de l'eau est une fonction du temps de submersion et de l'infiltration d'eau dans ses micro et meso porosités du liant. La capacité thermique volumétrique du béton poreux bio-réceptif a été estimée à ~ 1380 kJ m⁻³ °C⁻¹ par deux équations distinctes: une utilisant les capacités thermiques des composantes individuelles relevées dans la littérature pour obtenir les capacités du mélange, et une autre utilisant le bilan énergétique d'une dalle préalablement chauffée soumise à un refroidissement par un flux d'air.

Les principales conclusions suggèrent une possible utilisation du béton poreux dans des systèmes de chauffage, de ventilation et de climatisation. Les méthodologies et les données de perméabilité obtenue faciliteront l'intégration de ce matériel dans les systèmes de bâtiments actuels.

V. Acknowledgments

I would like to thank my supervisor Dr. Mark Lefsrud for his overarching support throughout my Master's and, my secondary adviser Dr. Hamid Akbarzadeh. This work would not be possible without Yasmeen Hitti who taught me the concrete recipes. Dr. Chapelat, Dr. Davide Zampini, Alexandre Guerini and Thomas Gerber and all of CEMEX Research Group AG (CRG facility, Switzerland) who I owe the setup of the experiments conducted during the summer of 2018. A special thanks goes to Markus Steiner and Cyndy A. Iñiguez who inspired me with their technical knowledge of refrigeration systems and cement chemistry respectively. A mention goes to the interns along with CEMEX research group AG Facility staff who treated me as family and friends during the summer of 2018: Ingrid Borda, Sergio Javelly, Arturo Manuel Zalles Balanza, Antonella Castellana, Rebecca Prieto Mattenberger, Cecilia Serrano and Francisco Javier Gibello Rael, the list goes on. Thanks to Samuel Bilodeau for first introducing me to the Biomass Production Laboratory, and all their transient members who we're part colleagues and part friends. Thanks to all my family and friends who have supported me along the way.

This thesis is dedicated to forwarding the research objectives of the joint venture comprising: Innovertch (Hannah McIver, Bob Campagnolo, Jonathon Roepke), McGill University and CEMEX Research Group AG (CRG).

VI. Contribution to Original Knowledge

Values for the permeability of a specific type of porous concrete are measured using various custom designs herein reported. Custom designs utilized air as a working fluid, commercially available fans, ducting and air property sensors. The studies conducted are reported and discussed as they relate to relevant material properties involved in the use of the material for the hydroponic growth of turfgrass (*Poa pratensis*) and the heating and cooling of flow-through air.

VII. Contribution of the Authors

For this thesis the contribution of the authors are as follows: (1) Tristan Chauvin-Bossé – designed and conducted all experiments, data collection, data processing, interpretation and redaction of the results. (2) Dr. Mark Lefsrud – supervised and guided the direction of all experiments, enabled all experiments and reviewed the thesis. (3) Dr. Abdolhamid Akbarzadeh Shafaroudi – provided co-supervision of the thesis and guidance. (4) Dr. Julien Chapelat – provided technical concrete knowledge and enabled the experimental set-ups devised and constructed in Switzerland. (5) Dr. Sarah MacPherson – reviewed various parts of the thesis.

1. Literature Review

1.1. Introduction

Permeable concretes (Figure 1.0.1), also called porous concretes (PCs), have similar composition to traditional structural concrete but differ in regards to aggregate particle size distribution (PSD) (narrow), amount of sand (little to no sand) and binder (significantly less binder) (Sun et al., 2018). Narrow PSD are particles retained between two consecutive standard-sized sieves (Marolf et al., 2004). Concretes having this composition present substantial networks of interconnected pores. Permeability is a property that quantifies the resistance of flow through a material. This value is commonly expressed by stating its hydraulic permeability which takes dimensions [length time⁻¹]. It is determined in the laminar flow regime using water as outlined in ASTM standard D2434 (2019) (Standard test method for permeability of granular soils (constant head)). However, extending to other permeation flows that are geometrically similar (laminar flow of a Newtonian liquid), the intrinsic permeability (k or α referred to as Darcy's permeability) which has dimensions [length²] can be used. Both values are used in cement and concrete material literature. Conversion from one to another depends on the fluid's density and viscosity (Hall and Hoff, 2012). In contrast to conventional concrete mixes, PCs permeability's are higher by several orders of magnitude (Zhong and Wille, 2016). Permeable concretes offer their use as construction material for surfaces where drainage of water is desired. Used in the construction of parking lots, low traffic routes and cement piping, it can be functionalized with water management systems (Huang et al., 2016). The main disadvantage of using PC is its lower strength and resistance to abrasion.

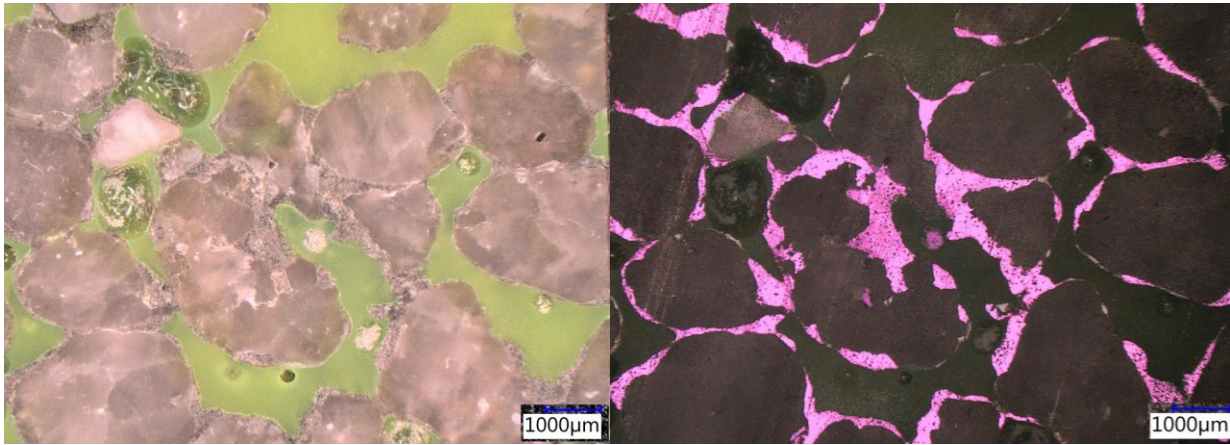


Figure 1.1.1: Cross-sectional cut of porous concrete impregnated with epoxy resin. Porous concrete was made using CEMII with quartz aggregate. The green on the left is the void space (normally occupied by air or water). The purple in the right image is the cement binding the aggregate together.

Notably, Hitti (2018) placed a prime focus on porous concretes as a hydroponic substrate. It was determined that a type of permeable concrete made using quartz aggregates on the mm length scale and an alkali activated ground blast furnace slag (AGBFS) cement can be used as a growing medium for the soilless culture of plants. Roots permeate into the pore network which hold plants in place. The concrete is then irrigated to supply plants with aqueous salts in the form of a hydroponic solution. Using this technique, grass has been grown on a vertical surface. As a stride towards lessening our environmental impact and developing building components reminiscent of natural environments, this porous concrete substrate is now being considered for building facades.

This thesis involves a description of a porous concrete mix capable of supporting plant growth. It is targeted towards developing its use in engineering designs. The literature review will focus on various concepts covered in later chapters. This thesis begins with a section on vegetation concrete describing the previous efforts made to incorporate plants and concrete. A chapter on PCs' defining property; permeability is included, followed by the chemistry of AGBFS because it is the most commonly reported cementitious material used for plant related porous concrete mix designs. Chapters on the water to binder ratio of cements and one on the drying of porous concrete finalize the literature review.

1.2 Vegetation Porous Concrete

Various publications have discussed incorporating vegetation into permeable concretes. The systems typically studied were discontinuous, vertically stacked layers of material. The researchers often included a superficial soil layer and focused on the composite effect of grass, soil, and concrete layers on slope stabilization, water drainage or water remediation (Kim and Park, 2016; Lee and Yang, 2016; Oh et al., 2014; Tang et al., 2018; Zhao et al., 2019). Oh et al. (2014) discussed a non-cement alkali-activated porous vegetation block. This block consisted of growing grass on a topsoil layer over a slab of jute reinforced porous concrete, using AGBFS. The focus was the change in 5-day biological oxygen demand, chemical oxygen demand, suspended solids, total phosphorus, and total nitrogen of the water flowing through the slab. Lee & Yang (2016) described promising results for alpha-calcium sulfate hemihydrate cements. They highlighted that the lower pH of their samples, as determined by thermogravimetry, established that they were in a range that could support plant growth. Tang et al. (2018) tested the growth of various native Australian grasses in soil occluded permeable concretes. Their binder consisted of calcium aluminate with varying proportions of fly ash. Zhao et al. (2019) reported using high portions of fly ash and slag in traditional concrete along with the addition of biochar aggregate to germinate various grass species. Plant tests in this case involved the use of inner pore soil, along with a 5 cm layer of soil on top. Kim & Park (2016a) (2016b) discussed the use of permeable prefabricated vegetation concrete blocks in drainage applications. Their preferred mix design consisted of AGBFS along with 6 kg m^{-3} of latex. This cement was used to bind 25 mm quartz aggregate. Higher void contents (undefined in the paper) were stated as beneficial in relation to plant growth. A field test was conducted where 5 cm of soil and mesh were added superficially prior to sowing. Others have investigated the composite use of concrete and vegetation systems (Sudimac Budimir et al., 2018). Their experimental study consisted in determining the energy savings of a modular perlite concrete façade element having dedicated holes for “plant shells” (dedicated growth containers). Long et al. (2017) profiled the microbial community of soil occluded in the porous concretes. They determined that microbial richness, diversity and structure in porous concrete is influenced by both plantation (the presence of plants or not) and plant species type, where *Proteobacteria* dominated the bacterial communities.

1.3 Permeability

Porosity, density and permeability are distinct physical material properties which have wide reaching implications in various fields such as air diffusers, filtering media and chemical engineering (Howe and Hudson, 1927). These properties are the ones most often cited for PCs after strengths. Darcy's Equation (1.3.1) is a fundamental law which describes pressure drop in fluid flowing through porous media. It incorporates permeability as a proportionality constant relating flow rate to a pressure gradient.

$$-\frac{\partial p}{\partial x} = \frac{\mu}{k} v \quad (\text{Equation 1.3.1})$$

Where: p is pressure (Pa), x is a coordinate along which the pressure drop occurs (m), k is Darcy's permeability coefficient (m^2), μ is the dynamic viscosity coefficient of the fluid ($\text{kg m}^{-1} \text{s}^{-1}$) and v is the filtration velocity (m s^{-1}). This equation is adequate for the description of flow through porous media at low Reynolds numbers (Sobieski and Zhang, 2014). This is often the case for experimental setups testing the falling or constant head permeability of porous concretes with water as the working fluid (Yinghong et al., 2015).

In scenarios described by high Reynolds numbers, such as the flow of air in large porous media, the regime is turbulent (Ferdos and Dargahi, 2016). For turbulent flows through porous media, permeability cannot be described using Darcy's equation. Instead, Forchheimer's extension to Darcy's equation can be used to model its behavior. Forchheimer's Equation (1.3.2) establishes a non-linear dependence between the drop in pressure across the porous media and the resulting fluid velocity (Innocentini et al., 2004).

$$-\frac{\partial p}{\partial x} = \frac{\mu}{k_1} v_s + \frac{\rho}{k_2} v_s^2 \quad (\text{Equation 1.3.2})$$

The first term to the left of Equation 1.3.2 is the pressure gradient across the porous sample. v_s is the surface velocity of the fluid (the volumetric flow rate divided by the total cross-sectional area, normal to the flow). The terms μ and ρ are the dynamic viscosity and the density of the fluid respectively. The constants k_1 and k_2 are named the Darcian and non-Darcian permeabilities (Innocentini et al., 2005). Fluent's (Fluid simulation software by Ansys) (Ansys, Pennsylvania, United States) version 12.0 user's guide on porous media establishes a method for deriving porous coefficients based on experimental pressure and velocity data resembling Forchheimer's equation. It refers to the two coefficients k_1^{-1} and k_2^{-1} as the viscous inertial resistance factor (the inverse of permeability; α^{-1}) and the inertial resistance factor (C_2) having units (m^{-2} and m^{-1} respectively)

(Xiao et al., 2010). They characterize linear and non-linear pressure behavior (drop) along the porous material (Nowak, 2016).

It is desirable to predict the flow rate obtainable for a given energy input without having to derive it experimentally. A review of this topic regarding unconsolidated materials statistically compares two friction factor-Reynolds number correlations: the nondimensional Forcheimer equation of Ahmed and Sunda and the modified Ergun equation (Equation 1.3.3) (Macdonald et al., 1979). It was determined that the modified Ergun Equation can be expected to predict the required energy for flow through unconsolidated media with results having an accuracy of $\pm 50\%$ when compared to experimental data. Ergun and Orning were the first to bring forth an equation relating both the viscous and the kinetic permeability terms to geometric parameters of the media (Quinn, 2014). Factors influencing the pressure loss through columns of packed granular materials are typically subdivided into four categories: The rate of fluid flow, viscosity and density of the fluid, closeness and orientation of the packing and size, shape and surface of the particles (Ergun, 1952).

$$F_k' \frac{\epsilon^3}{1-\epsilon} = B + \frac{A(1-\epsilon)}{N_{Re}'} \quad (\text{Equation 1.3.3})$$

Where

$$F_k' \equiv -\frac{\text{grad } P}{\rho V_0^2} D_{eq} \quad (\text{Equation 1.3.4})$$

And

$$N_{Re}' \equiv \frac{\rho V_0^2 D_{eq}}{\mu} \quad (\text{Equation 1.3.5})$$

In the original equation, specific constants 150 and 1.75 take the place of A and B. In this equation, ϵ is porosity of the porous medium and D_{eq} is a characteristic length of the medium. It is often chosen to be $\equiv 6 \frac{v_p}{s_p}$ where $\frac{v_p}{s_p}$ is the volume to surface ratio. The modified Ergun equation can be used to relate A and B to Forchheimer's Equation (2).

$$\text{By } \frac{1}{k_1} = A \frac{(1-\epsilon)^2}{\epsilon^3 D_{eq}^2} \quad (\text{Equation 1.3.6}) \quad \text{and} \quad \frac{1}{k_2} = B \frac{(1-\epsilon)}{\epsilon^3 D_{eq}} \quad (\text{Equation 1.3.7})$$

Many more equations have been established to express both permeability terms as functions of porous media properties. They are applicable to water flow through sand and gravel

at low Reynolds numbers. Perhaps the most common equation for the first permeability term k_1 is the Kozeny-Carman Equation (1.3.8) (Berryman and Blair, 1987), (Sobieski and Zhang, 2014).

$$k_1 = \frac{\epsilon^3}{c\tau^2 S^2 (1-\epsilon)^2} \quad (\text{Equation 1.3.8})$$

Where k_1 = permeability, $\tau = \frac{L_e}{L}$ = tortuosity (L_e = effective path length and L = sample path length), C = Kozeny's constant and S is the specific surface σ with respect to the unit volume of the solid matrix (Schulz et al., 2019).

While porosity is one of the most important properties of porous concrete, it alone cannot determine pore structure and the performance of the material. For PC samples of equivalent porosities, increasing aggregate size from 2.36 mm to 9.5 mm was found to increase permeability twofold. Efforts in establishing the validity of Equation 1.3.8 when employed for porous concrete mix designs were performed with water in the laminar to transitional flow regimes (Kia et al., 2018; Montes and Haselbach, 2006). Equation 1.3.9 was suggested for PCs (Zhong et al., 2016).

$$K = \frac{d_a^2 \epsilon_e^3}{72 (1-\epsilon_e) \tau^2} \quad (\text{Equation 1.3.9})$$

Where d_a^2 = aggregate size. Zhong et. Al. (2016) also proposed equations to derive tortuosity based on the relative mean pore size for three different sized aggregates.

It is possible for two porous media of the same porosity to have entirely different permeabilities. If a correlation function between the two quantities (fluid velocity and column pressure drop) is sought after, it cannot be unique. Therefore, most empirical correlations contain some other factors, usually vaguely identified with alleged geometrical quantities. They are undetermined factors used in order to make the data fit the desired equations (Quinn, 2014).

1.4 Cements and Pozzolans

Silicates are the most abundant matter in Earth's crust. On an elemental basis, oxygen and silicon predominate with 45-50% and 28% by mass respectively. Silicates are covalent atomic solids containing silicon, oxygen and various other metals. Rocks, clays and soils are all examples of materials containing silicates (Tro et al., 2014). Cements contain silicates and are the main ingredient of concrete. Concretes are typically made by mixing ordinary Portland cement (OPC) and water with sand and aggregate. Tricalcium silicate is responsible for the early age strength of concrete. It is the major characteristic phase of OPCs and is referred to as alite, $3\text{CaO} \cdot \text{SiO}_2$ or C3S in cement chemist notation (Brunauer and Copeland, 1964). The formation of alite requires the calcination of carbonate rocks, typically limestone. This is a high temperature, energy intensive

process that releases carbon dioxide as a byproduct of the decarbonation of limestone. Because of this, Cement production accounted for 5% of global CO₂ emissions from all industrial and fossil fuel combustion in 2013 (Xi et al., 2016).

Cement is the second most consumed product after water and its demand is projected to rise in forthcoming years. It is estimated that cement production could represent 10-15% of global CO₂ emissions by 2020 (Cancio Díaz et al., 2017). Because of this, efforts in reducing its carbon footprint is necessary. Partial substitution of calcined carbonate rocks by fly ash and metallurgical slag is a viable way of reducing the materials ecological footprint. Both are waste byproducts having cementitious behavior. Portland cements that do not contain a significant proportion of secondary materials are favored due to their more predictable material properties and hydration kinetics. However, on account of environmental and economic matters there is a tendency towards the use of cements containing granulated blast furnace slags, fly ashes and other natural pozzolans (Hewlett, 2004).

Slag is a waste byproduct of ore smelting and refining. When ground, this material is used as a filler in cements which reduces the carbon dioxide footprint of concretes. Pozzolans are the most commonly used cement admixture (Hasan and Hanifi, 1995). They are siliceous or siliceous and aluminous materials that possesses little or no cementitious value in themselves. In a finely divided form they will chemically react with calcium hydroxide and moisture at room temperature to form compounds having cementitious properties (Institute, 2005). Slag which has been rapidly cooled is typically a more reactive pozzolan. The addition of an alkali solution to finely ground slag particles will partially dissolve them. Through time, the various ionic species react, and the product hardens. They form a hydration product comparable to geological feldspars. The result of introducing an alkali solution to ground granulated blast furnace slag is a pasty material which behaves like a thermosetting organic polymer. Irreversible hardening of a soft solid or liquid prepolymer is achieved through chemical reactions cross-linking polymer chains into a network. For this reason AGBFS are often erroneously referred to as geopolymers (Khale and Chaudhary, 2007).

1.5 Alkali Activated Blast Furnace Slag (AGBFS)

Finely divided blast furnace slag combined with alkali activators produce a hardened binder called alkali activated material (AAM) (Provis, 2018). There is ambiguity in the scientific literature regarding alkali activated materials being classified as geopolymers. One of the initial

scientific disseminators of AAM research is a proponent that alkali activated slag is not a geopolymer (Provis et al., 2015). His work forwarded the hypothesis that AGBFS does not covalently bind the alkali metals which he considers should be the case for geopolymerization. This discussion is beyond the scope of this thesis. Geopolymers are often considered synonymous with low-temperature aluminosilicate glass, alkali-activated cement, geocement, alkali-bonded ceramic, inorganic polymer concrete and hydroceramic in various publications (Duxson et al., 2006).

Glassy blast furnace slags with CaO/SiO_2 ratios between 0.5 and 2.0, and $\text{Al}_2\text{O}_3/\text{SiO}_2$ ratios between 0.1 and 0.6 are considered suitable for alkali activation. ECOCEM (ECOCEM, France) is a blast furnace metallurgical slag with value added processing marketed to the cement industry. It has a ratio for CaO/SiO_2 of 1.14 and for $\text{Al}_2\text{O}_3/\text{SiO}_2$ of 0.30. The reaction mechanisms involved in the hardening of AAM has been a long-standing debate. Hydration differs from traditional Portland cement and will vary depending on feedstock composition, and alkali activator formulation (Chindaprasirt and Cao, 2015).

The process by which ground slag become an interconnected material begins with the partial dissolution of the its particles when an alkali solution is introduced. This releases ions in the solution phase which react and form the hydration products by nucleating on surfaces. At a certain point the particles become bound together in clustered networks. During the formation of these networks, the paste goes from a viscous liquid like slurry (in which particles are dissolved) to an interconnected solid phase (Jansson et al., 2015). Most of the literature agrees that the mechanisms involved in the hydration of alkali activated slag proceeds as such: Silica dissolution, transportation and then polycondensation (Pacheco-Torgal et al., 2008). The overall process is like OPCs', however, differing precipitation mechanisms have been reported. Dissolution-precipitation is the main chemical mechanism occurring during the early reactions in AAMs. Space originally occupied by the liquid phase is then largely filled with hydration products. Reacted "rims" around slag particles suggest that some in situ hydration products are formed during the later stages of hydration (Wang, 2000). The water retained in the hydration products of AAS in the saturated state is higher than that of OPCs at about 0.44 g/g of cement reacted (Chen and Brouwers, 2007), of which 0.20 g/g is non evaporable (chemically incorporated into hydration products determined on a stoichiometric basis).

C-S-H(I) with a C/S ratio of 1-1.2 is the major hydration product of alkali activated slag pastes (Wang et al., 1995). Upon hydration, Si-O, Al-O and Ca-O bonds on the surface of slag

particles are dissociated under the polarization effect of hydroxides. The dissolved species exist as $(\text{H}_2\text{SiO}_4)^{2-}$, $(\text{H}_3\text{SiO}_4)^-$, $(\text{H}_4\text{AlO}_4)^-$ and Ca^{2+} . The concentration of calcium cations is greater due to the comparatively weaker Ca-O bonds. It was observed that a rich Si-Al layer forms quickly on the surface of slag particles (Shi et al., 2006).

Alkali activated materials were first introduced in 1940. The issues regarding the handling of caustic sodas, the sensitivity of alkali solution dosage and the cost are important impediments for large scale adoption but have not prevented its use in major infrastructure. The study of reaction kinetics for alkali activated materials is nowhere near as complete as for Portland cement. (Juenger et al., 2011). The hydration of OPCs is divided into various periods: Initial pre-induction, induction, acceleration, deceleration and diffusion (I-V). Differences in cement composition can affect hydration peaks. For AAMs, hydration falls within one of three classes (type I, type II and type III) as depicted in Figure 1.5.1 (Shi and Day, 1995).

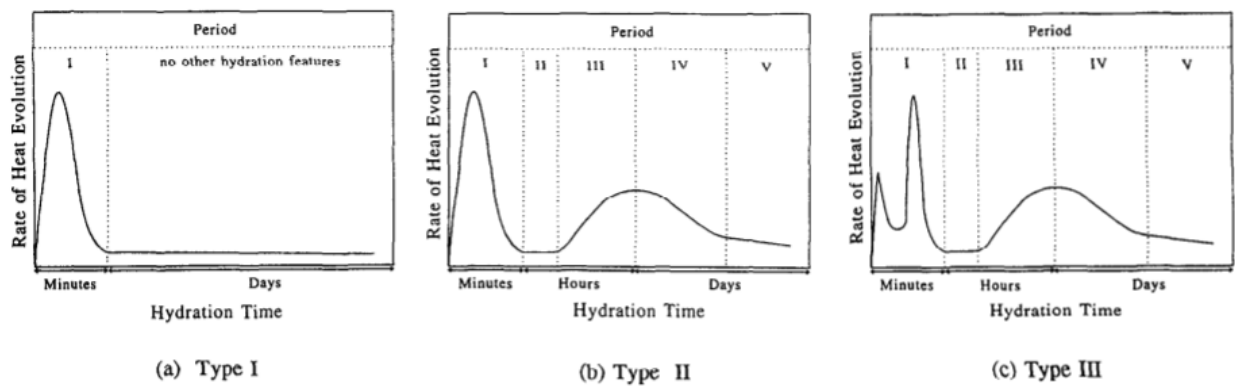


Figure 1.5.1: Schematic representation of hydration models for alkali-slag cements.

The varying characteristic curves are the result of hydrating slag in water or with a Na_2HPO_4 solution (type I), a NaOH solution (type II) and solutions of Na_2SiO_3 , Na_2CO_3 , Na_3PO_4 or NaF (type III). At high concentrations of OH^- , $\text{Ca}(\text{OH})_2$ does not precipitate from the activation solution. Instead, a thin layer of C-S-H with a low calcium to silicon ratio, C_4AH_{13} and C_2ASH_8 (which have comparatively lower solubility's) precipitates quickly. Slags with higher calcium to silicon ratios (more basic) typically result in an expansion of the glass network, facilitating the splitting of existing Si-O-bonds with a dependency on the activator employed (Tänzer et al., 2015). For solutions of Na_2SiO_3 , C-S-H is the main result. The delayed reaction peak is attributed to the time Ca^{2+} takes to reach a critical value (Shi and Day, 1995).

The effect of alkali activator dosage (made by combining varying ratios of sodium silicate and sodium hydroxide) has been reported to effect the properties of alkali activated slag pastes at a constant water to binder ratio of 0.35 (Jiao et al., 2018). Strength, initial setting time, chemical composition and compressive strength are not only affected by the pH of the water used for hydration. The chemical composition, defined as the water glass modulus (molar or mass ratio of $\text{SiO}_2/\text{Na}_2\text{O}$) is also an important factor (Jansson et al., 2015). Winnefeld et al. (2014) conducted various tests on the influence of slag moduli (oxide ratios) and activator chemical composition. It was determined that slag having a $(\text{CaO} + \text{MgO}) / \text{SiO}_2$ ratio between 1.25 and 1.30 had capillary porosity below 2.5 % when activated with sodium silicate. When activated with sodium hydroxide, the capillary porosity remained above 10 percent (Winnefeld et al., 2014).

1.6. Water to Binder Ratio

In cement chemistry, the addition of water to non-hydrated cement particles is associated with chemical and physico-mechanical changes of the system. Setting and hardening is the most notable effect (Hewlett, 2004). Water to binder ratio (w/b) referred to as water to cement ratio (w/c) or water to solid ratio (w/s) by unit mass is an important parameter when formulating concrete recipes and mix designs. For OPCs this ratio directly influences the rheology of the produced suspensions and the progress of hydration. The resulting properties of the hydrated (hardened) material, such as compressive strength, specific surface area and porosity will vary at differing ratios (Hewlett, 2004). For AAMs the w/b ratio is typically higher than that of OPCs. Experiments at water to binder ratios of 0.27 to 0.52 have been reported (Provis and Van Deventer, 2014).

The workability of a concrete mix is measured before setting/hardening and usually defined as the slump according to ASTM standard C143 (2015) (standard test method for slump of hydraulic-cement concrete). The value has the units of length and refers to the distance a predetermined volume of concrete placed inside a standard slump cone will fall once it is removed. Drier mixes with lower workability will have correspondingly lower values. This can hinder the final strength of a concrete element if it cannot fully and evenly fill a mold. The water required for the hydration of cement represents approximately 0.25 mass fraction of the binder, the rest is added to achieve the optimal consistency. Chemical admixtures have a long-standing use in cement formulations. They are mainly used for prolonging the setting time and reducing the amount of water necessary. Both plasticizers and superplasticizers are considered water reducing agents.

Plasticizers are organic surfactants which modify the electrostatic forces between the cement's particles. Superplasticizers work by adsorbing to the cement particles and reduce the attractive forces of Van der Waals interparticle interactions (Khudhair et al., 2018). By reducing the required amount of water to achieve an equivalent workability, strength of the final product increases. The rheological properties of fresh cement and concrete have been extensively described (Banfill, 2003).

Concrete mixes with lower water to binder ratios result in higher strength (Jorge de et al., 2018). Decreasing water to binder ratio from 0.35 to 0.25 can increase compressive strength by as much as 26 MPa for traditional concretes (Piasta and Zarzycki, 2017). This is due to the higher density and correspondingly lower micro and meso-porosity of the final product.

With regards to porous concretes, the effect of this ratio is less significant. In one instance w/b was found to have no significant influence from 0.25 to 0.35 (Kovac and Sicakova, 2017). Others have reported that increasing w/b from 0.28 to 0.33 increased strength but decreased it after further increasing this ratio to 0.34 (Neamitha and Supraja, 2017). The discrepancy is possibly linked to a trade-off in between the strength of the binding material and the coating of the aggregate.

The composite effect of aggregate size, water to binder ratio and porosity on permeability was investigated for traditional cement mixes (Tun Chi et al., 2014). Connected porosity was found to increase as the aggregate size increased. Connected porosity is an important parameter which relates to permeability. The connected pores are the paths through which a fluid may permeate. Connected porosity was correlated to filled percentage of voids for permeable concretes made using alkali activated slag at a water to binder ratio of 0.35 for 2.4 - 4.8 mm aggregates (Chang et al., 2016).

Water permeability is directly proportional to connected porosity. Under equivalent connected porosities, mean void size paths decreases for smaller aggregate sizes. This increases tortuosity which inversely affects permeability. At a w/b ratio of 0.45 with 30% porosity or lower, the sagging in the paste was too pronounced to obtain permeability measurements on 10 cm diameter by 20 cm thick cylindrical specimens using the constant head permeability test for aggregate sizes of 4.8, 6.4, 9.7 and 12.7 cm. The permeability of mixes containing smaller aggregates are more sensitive to a decrease in porosity (Tun Chi et al., 2014). An increase in the workability of fresh cement paste was found to decrease hydraulic conductivity of porous concretes due to the influence on pore tortuosity (Zhong et al., 2016).

Porous concretes made using different supplementary cementitious materials (varying portion of silica-fume and or fly ash) with a maximum aggregate size of 10 mm at approximately 20 % of voids were found to have discrepancies in their water permeabilities. Traditional Portland cement mixes were found to have up to 42 % higher permeability (approximately 6 mm s^{-1}) than binder mix compositions containing 8 % silica fume and 8 % fly ash (Rasiah and Kassis, 2014).

1.7. Air Drying of Porous Concretes

The water content of porous concretes affects its permeability and is involved in the hydroponic growth of plants on PCs. Like most building materials, alkali activated slag is hygroscopic. A certain percent of moisture remains within the PC samples when in contact with unsaturated damp air. The definite relationship between the amount of hygroscopically bound water and the relative humidity of the surrounding atmosphere is referred to as the water vapor or sorption isotherm (Johansson et al., 1958). These values have been investigated for a range of alkali activated cement pastes (fly ash and ground granulated blast furnace slag (GGBFS) mixes of varying proportions). It was determined that increasing the GGBS content along with curing at ambient temperatures resulted in an increase in the amount of water layers adsorbed on the internal surfaces of the paste pores (Babae and Castel, 2018). Very fine pore structure of high content GGBS mixes were prone to time-dependent microstructural changes influencing sorption kinetics.

Evaporation rates from porous media can vary considerably due to changes in internal transport mechanisms (Zami-Pierre et al., 2016) and interruption of hydraulic continuity (Shokri et al., 2010). Both are influenced by media pore space properties. As stated by Bear & Buchlin (1991), “It is unrealistic at the present time to hope for a complete physically reliable description of drying mechanisms.” Moisture transport is a multi-phase mechanism which involves both the gaseous and liquid phase. Part of this process happens in pores via adsorption and desorption of the multi-molecular water layers on pore walls (Babae and Castel, 2018). The degree to which water is held within the overall porous media varies throughout the drying period (Bear and Buchlin, 1991).

Drying kinetics will depend on pore structure (Kowalski, 2007). Binder micro porosity changes during the serviceable lifetime of alkali activated materials. The transient nature of cements’ physical properties complicates the applicability of mechanistic drying models. The porosity of traditional concrete incorporating GGBS activated by water-glass was found to decrease from ~ 13 to 10.5 % from day 7 to 365 (Al-Otaibi, 2008). After loosely bound water is

evaporated, dry shrinkage occurs. This reduced the strength and increased total porosity (Chen and Brouwers, 2007). Most authors agree that the hydration of AAMs produce calcium silicate hydrates with aluminum in its composition (C-A-S-H gel) and that the hydration products depend on the type and concentration of the alkali activation solution (Garcia-Lodeiro et al., 2015). The products of high calcium systems ($\text{CaO} > 35 \%$) are like the ones of OPCs (C-S-H gel) and they both heavily involve water. It is present in saturated-hydrated C3S paste. After reacting, the water used for chemical hydration ends up divided. It is incorporated in the structure of the C-S-H phase. It is bound in the form of OH^- ions within the crystalline lattice of calcium hydroxides. It is adsorbed to the solid surface of the hydrated phases and fills the gel and capillary pores of the hardened paste. The bonding forces by which the water molecules remain within the solid structure vary in a wide range and may overlap for distinct categories (Hewlett, 2004). Thermogravimetry is often employed to quantify various types of water during the hydration process (Tashima et al., 2013). This involves heating a sample up to $650 \text{ }^\circ\text{C}$ while monitoring mass loss.

The drying and the flow of liquids in porous media are defined by heat and mass transfer. The prediction of this process is important to the cement and concrete industry due to its involvement in the degradation of concrete exposed to extreme temperatures (building fires, frost damage and spalling of refractory concrete). A collection of relevant models can be found in *mathematical modelling of kiln and on-site drying of concrete* (Turner and Mujumdar, 1997). To be accurately described, phenomena relevant to moisture, pressure and temperature must be coupled. The classical theory of drying from porous media under constant conditions distinguishes between two phases. At first, a drying rate like that of a free liquid surface occurs. At this point, the evaporation is controlled by the vapor transport properties of the airstream (Keey, 1972). As the removal of liquid from the pores take place, the drying front recedes into the substrate. As the liquid migrates deeper, the evaporation-rate decreases. It becomes more dependent on the molecular diffusion of vapor through the pore network and less dependent on the transport properties of the airstream (Griffiths and Roberts, 1999).

Diffusion, capillary and evaporation-condensation mechanisms are relevant to the drying of lightweight concrete walls subjected to temperature gradients (Huang, 1979). During the funicular stage of the wetting, Figure 1.7.1 taken from Bear & Buchlin (1991), fluid diffusion is the main moisture transport mechanism. In the pendular stage, diffusion, capillary and evaporation-condensation are all relevantly contributing to transport. With regards to building

facade performance, the modelling of droplet evaporation from porous surfaces has been investigated using a wind tunnel and ambient air (Griffiths and Roberts, 1999).

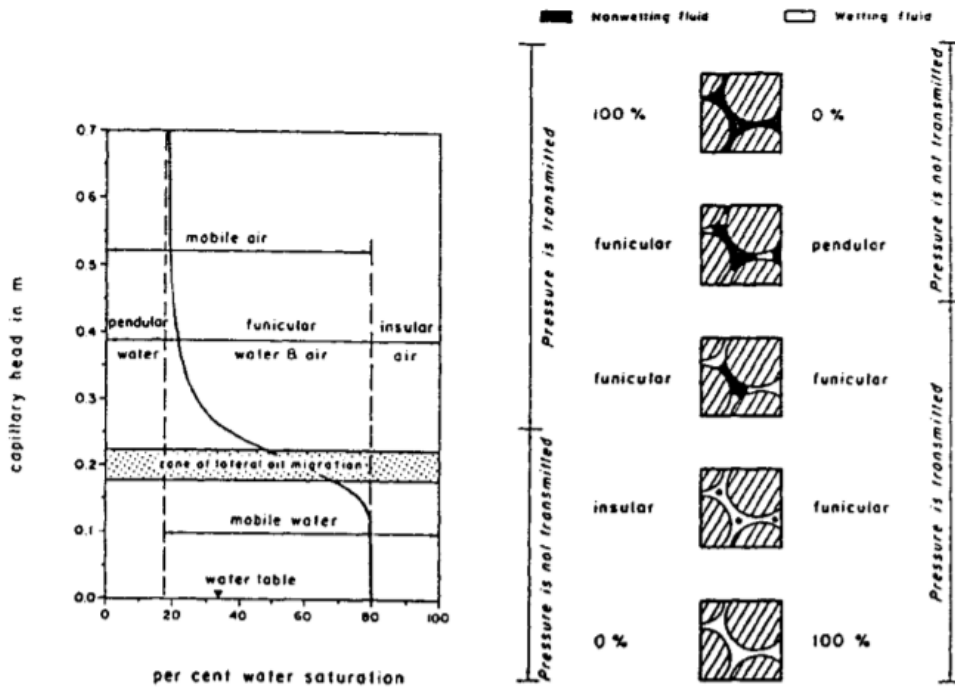


Figure 1.7.1: Distribution of a wetting (water) and a non-wetting (air) fluid in the pore space of a porous medium.

An adequate description for the drying of porous concrete requires a multiscale modelling approach. It is also a multi-physics process in which various heat and mass transfer mechanisms can take place simultaneously inside of the material and at its interface with the external environment. The processes are typically described as a series, parallel, and/or series-parallel combination of heat conduction, heat convection, heat radiation, phase change (evaporation), laminar and turbulent flow, seepage flow, gas diffusion and absorption-desorption. This makes modeling the transport physics in drying porous media one of the major challenges of drying technologies. Of current interest is the application of fractal theory in modelling the multiphase flow involved in the drying of multiscale porous media. However, there lack universal relationships in between the drying process and the fractal characteristics of materials which hampers it's practical application (Xu et al., 2019).

1.8. Conclusion

Slag is a by-product of the metallurgical industry. With value added processing, waste slag can be used as a supplementary cementitious material in concretes. Porous concretes are typically

used for reducing runoff by allowing water to permeate into the ground. Its use as a hydroponic substrate for the growth of plants is being developed. For this, ideal concrete mix designs incorporate cement made entirely of alkali activated slag from blast furnaces. Many properties other than the chemistry of the material must be considered for its functional use in engineering designs. This thesis contains experiments quantifying various properties of alkali activated porous concretes. A focus is placed on the air permeability of alkali activated slag as it is uncommonly reported in the literature. The second chapter starts off by exploring the effect of water to binder ratio on the compressive strength of AGBFS used to fabricate the porous concrete samples for which permeability is quantified in Chapter 3 and 4. Chapter 4 documents the effect of water to binder ratio on the permeability of concrete mixes. The last two chapters (Chapter 5 and Chapter 6) document flow-through drying and prototype use-cases on the samples studied in prior chapters.

2. Effect of Water to Binder ratio on the Hydration of Slag Cements

2.0. Abstract

The early age strength of alkali activated ground granulated blast furnace slag cement cylinders (ECOCEM, France) was studied to determine the extent to which the water to binder ratio (w/b) might influence the strength and the chemical kinetics of concretes made with this type of cement. For w/b ratios of 0.25, 0.3 and 0.35, activated using aqueous solutions of 6 % NaOH and 12 % sodium silicate (percent mass of binder), average compressive strengths of 26, 18 and 19 MPa after 20 hours of sealed curing were respectively obtained. For the cement mix studied, w/b ratios of 0.25 resulted in a higher mean compressive strength. A qualitative assessment on the heats of hydration is established by monitoring the exterior temperature of the cylindrical molds employed for sample preparation. The description of the device employed serves as an example for future research.

2.1. Introduction

Water to binder (w/b) ratio is a ruling factor affecting strength of cements. It is inversely proportional to strength (Aïtcin, 2000). Other properties of cement such as micro and meso porosity, and the workability of the resulting concrete mixes are discussed in Section 1.6.

Admixtures known as superplasticizers enable higher strength concretes by reducing the amount of water required to obtain rheological properties conducive to pouring. A large portion of the admixtures traditionally used in cement formulations are not applicable to alternative cementitious binders, in part because of the higher pH of the hydrating water necessary to achieve hardening (Juenger et al., 2011).

The following study qualitatively investigates the kinetics of alkali activated ground blast furnace slag cylinders hydrated with aqueous solutions of 6 % NaOH and 12 % sodium silicate (percent mass of binder) at varying water to binder ratios and the effect of C-S-H seed nucleation as described in (Hubler et al., 2011). The compressive strength after 20 hours is measured.

2.2. Materials and Methods

2.2.1.: Alkali Activated Slag Cylinders

Alkali activated slag cylinders are were cast in plastic pipe segments having a wall thickness of 7 mm, an inner diameter of 40 mm and a height of 40 mm (Figure 2.2.4, bottom left). The alkali activator was formulated by dissolving sodium hydroxide (sodium hydroxide, Pellets A.C.S., ACP Chemicals Inc., Quebec, Canada) and water glass (sodium silicate Solution, Na₂O ~ 10.6 % & SiO₂ ~ 26.5 %, Sigma Aldrich, Missouri, United States) in deionized water. 300 g of slag (ECOCEM, France) (Table 2.2.1, Figure 2.2.1 and Figure 2.2.2; slag was purchased, analyzed and provided by CEMEX Research Group AG (CRG), Switzerland) was combined with the activation solution by stirring with a metal rod until a uniform paste was obtained (approximately 2 - 3 minutes). The resulting paste was then evenly divided into three molds. Tapping their sides ensured an even consolidation of the material within. The plastic cells were sealed with parafilm.

Table 2.2.1: Chemical analysis of slag by X-ray fluorescence (XRF) (Axios advance 4.2kw, PANalytical, Malvern, United Kingdom). Major elements were determined by fused bead. Minor elements were determined by pressed pellet. For the fused bead, 1 g of calcinated sample was mixed with 8 g of CEMEX flux (70 % Li tetraborate, 30 % Li metaborate) with a fusion time 20 minutes. Loss on ignition (LOI) is carry out according ASTM C114 (standard test methods for chemical analysis of hydraulic cement), 45 minutes at 950°C. Data supplied by CEMEX Research Group AG (CRG), Switzerland.

Oxide	SiO ₂	Al ₂ O ₃	Fe ₂ O ₃	CaO	MgO	SO ₃	Na ₂ O	K ₂ O	TiO ₂	P ₂ O ₅	Mn ₂ O ₃	LOI at 950 °C
%	36.67	11.03	0.38	41.98	6.74	1.71	0.25	0.39	0.67	0.01	0.18	0.25

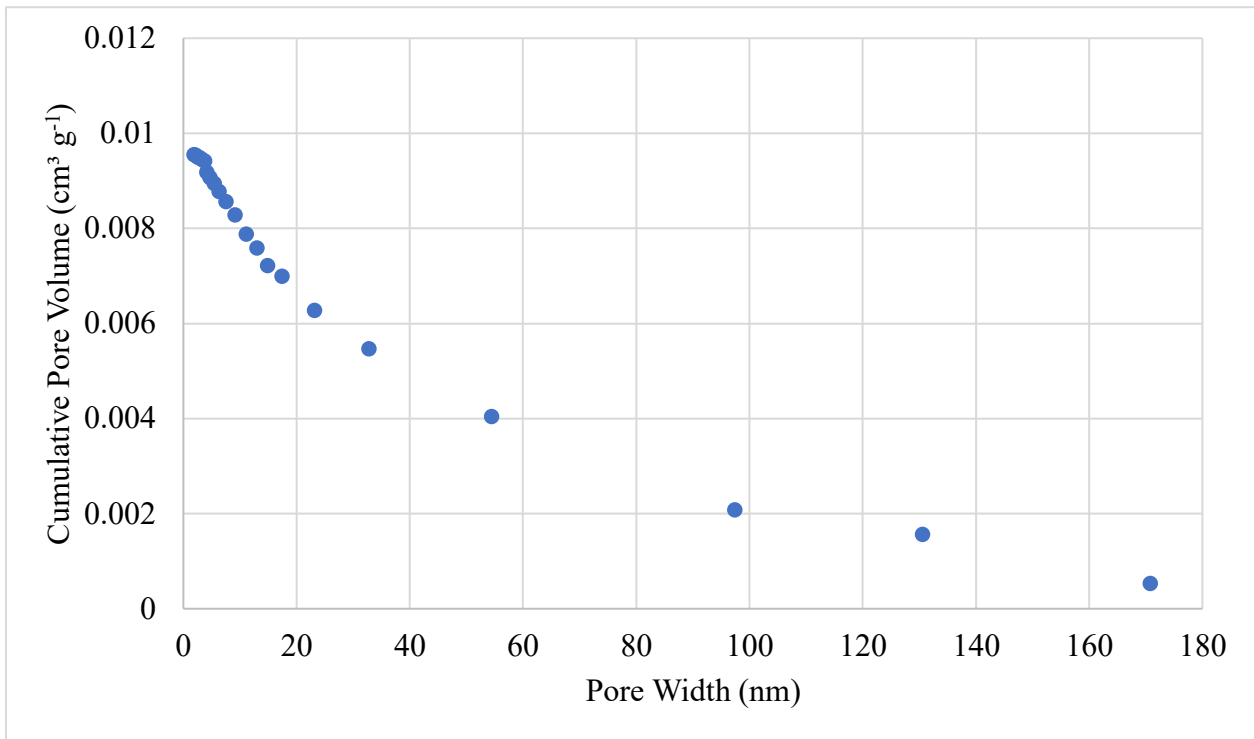


Figure 2.2.1: BET and BJH desorption of slag (ECOCEM, France). Data supplied by CEMEX Research Group AG (CRG), Switzerland.

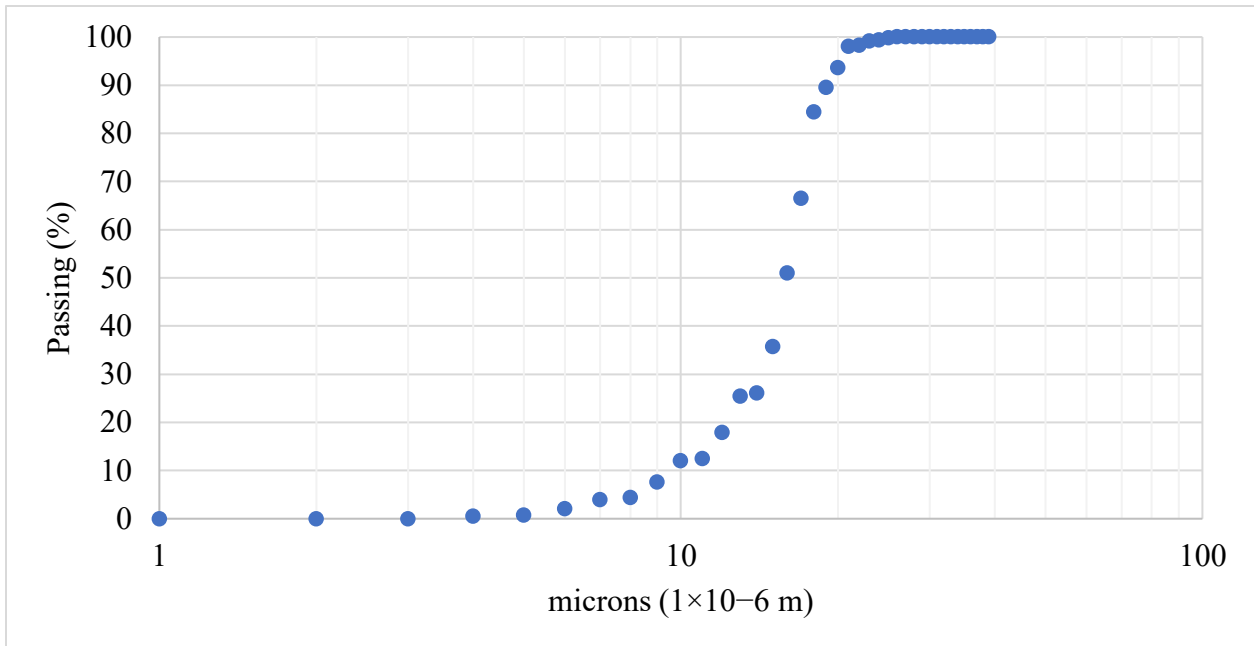


Figure 2.2.2: Particle size distribution of slag (ECOCEM, France). Data supplied by CEMEX Research Group AG (CRG), Switzerland. The density of the slag was measured at $\sim 2800 \text{ kg m}^{-3}$. Its Blaine Fineness was specified by the manufacturer at $447 \text{ m}^2 \text{ kg}^{-1}$.

2.2.2.: Calcium Silicate Hydrate (C-S-H) Seed Preparation

For seeded samples, C-S-H was isolated from precipitates of an aqueous solution of sodium silicate and calcium nitrate. The precipitates were formed by adding 1 M calcium nitrate dropwise into a diluted water glass solution. The precipitate was separated from the solution by filtration for 24 hours using a Büchner funnel with glass microfiber filter. The top translucent gel layer of the precipitate was used as the C-S-H for seeding samples r0 to r2 (Table 2.3.1).

2.2.3.: Monitoring the Temperature of Cement Cylinders

To monitor the hydration kinetics of the slag during curing, the outside centerline temperature of each cylinder was measured every minute using thermocouple wire type K (K Type thermocouple, extension wire, OMEGA, Biel, Switzerland) connected to a data logger (Data acquisition / data logger switch unit, 34970A, Keysight Technologies Canada Inc., Ontario, Canada) through an ancillary component (Multiplexer test accessory, 34901A, Keysight Technologies Canada Inc., Ontario, Canada). The samples containing the plastic molds were placed in between two perforated sheets of insulating material and left in a room at a temperature of 25 ± 5 °C.

2.2.3.: Compressive Strength

After 20 hours, the hardened slag cylinders were removed from their molds. Uneven top and bottom surfaces were filed flat. Samples were then subjected to compressive strength using a hydraulic press with minor graduations of 1 US-ton on a fitted gauge (Figure 2.2.3). Samples were compressed in between two steel plates. The hydraulic press was manually operated with a foot lever at a loading rate lower than one half of a US-ton per 30 seconds. The compressive strength was obtained using equation 2.2.1.

$$\sigma = \frac{F}{A} \quad (2.2.1)$$

Where σ was equal to the compressive strength of the sample in N m^{-2} , F was the load applied as determined by the gauge on the hydraulic press in newtons, and A was the average cross-sectional area of the cylinder in m^2 .

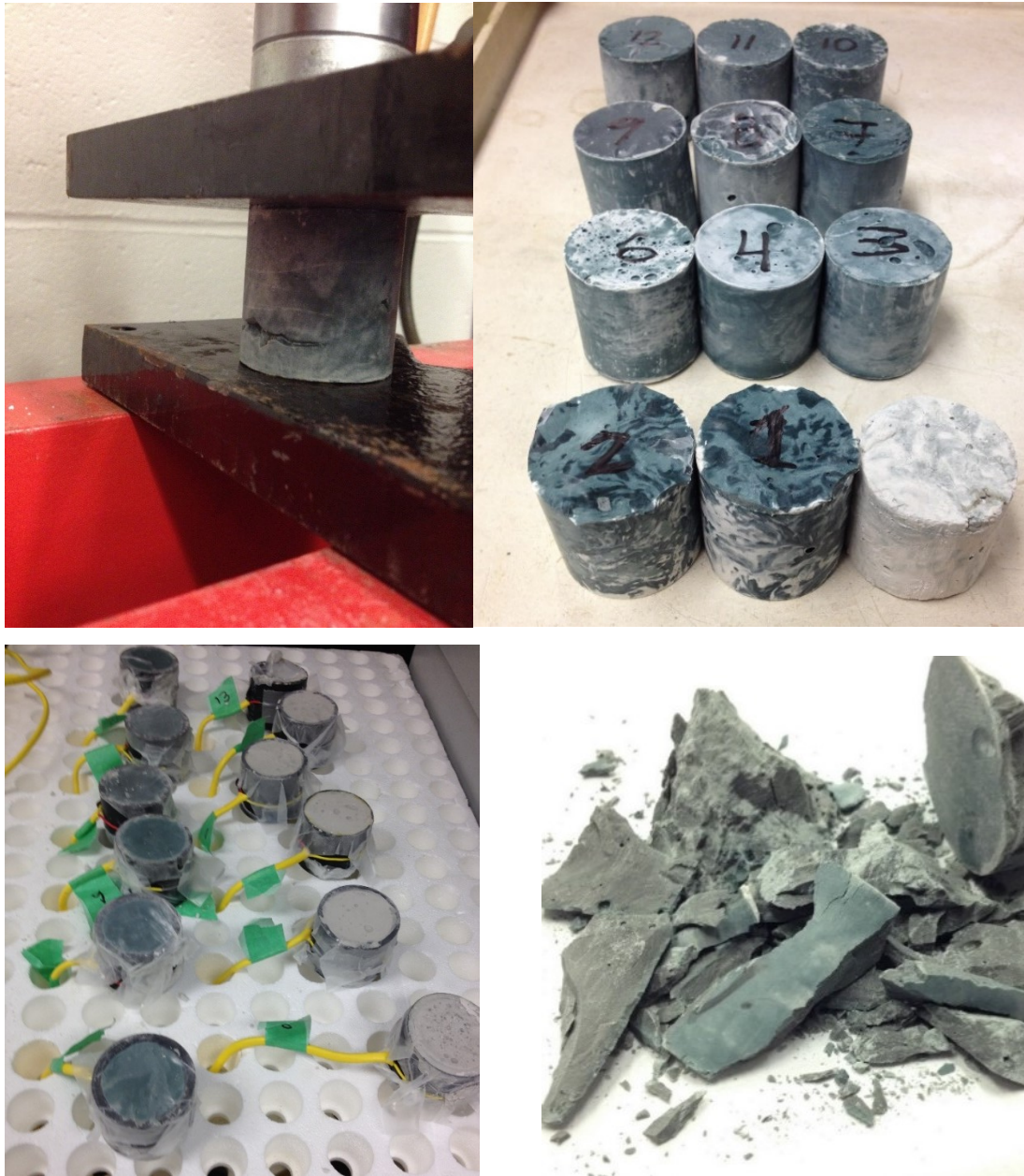


Figure 2.2.3: Experimental setup for the determination of strength and hydration temperature of alkali activated slag cylinders. Top left: Hydraulic press and steel plates used to compress samples. Top right: Samples tested. Bottom left: Samples during curing with thermocouples yellow wires (type K thermocouple extension grade). Bottom right: Sample 4 after being tested for compressive strength.

2.3. Results

Table 2.3.1: Mix designs and performance of alkali activated slag (ECOCEM, France) activated with an alkali solution of 6 % NaOH and 12 % sodium silicate (percent mass of binder). Samples are labeled according to their w/b ratio and are followed by a replicate code (r0, r1 ...).

Sample	0.30 + seed			0.35			0.30			0.25		
	r0	r1	r2	r1	r2	r3	r1	r2	r3	r1	r2	r3
ECOCEM (g)	300.0			300.0			300.0			300.0		
Water glass (g)	36.0			36.0			36.0			36.0		
Sodium hydroxide (50 % by mass of solution) (g)	36.3			36.3			36.3			36.0		
DI water (g)	50.3			64.4			49.9			40.9		
C-S-H gel (g)	0.9			-			-			-		
20-hour compressive strength (MPa)	17	17	22	17	18	23	21	18	16	24	27	27
Max temp achieved at (Min After mixing)	-	243	219	331	353	408	214	193	188	169	182	185
Max temperature of (C)	-	26.7	28.7	26.7	27.3	24.4	30.7	31.4	33.5	30.0	27.7	25.4

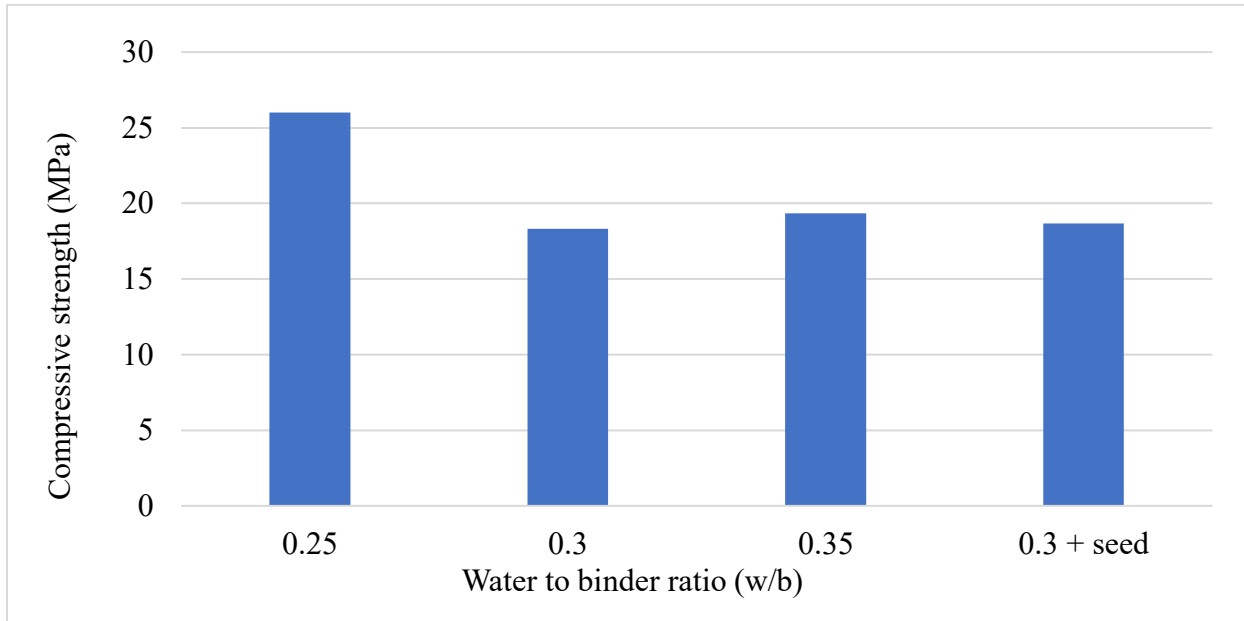


Figure 2.3.1: Average 20-hour compressive strength of alkali activated slag cylinders. + seed refers to the controlled addition of 0.9 g of C-S-H to the slag paste. w/b: water to binder ratio.

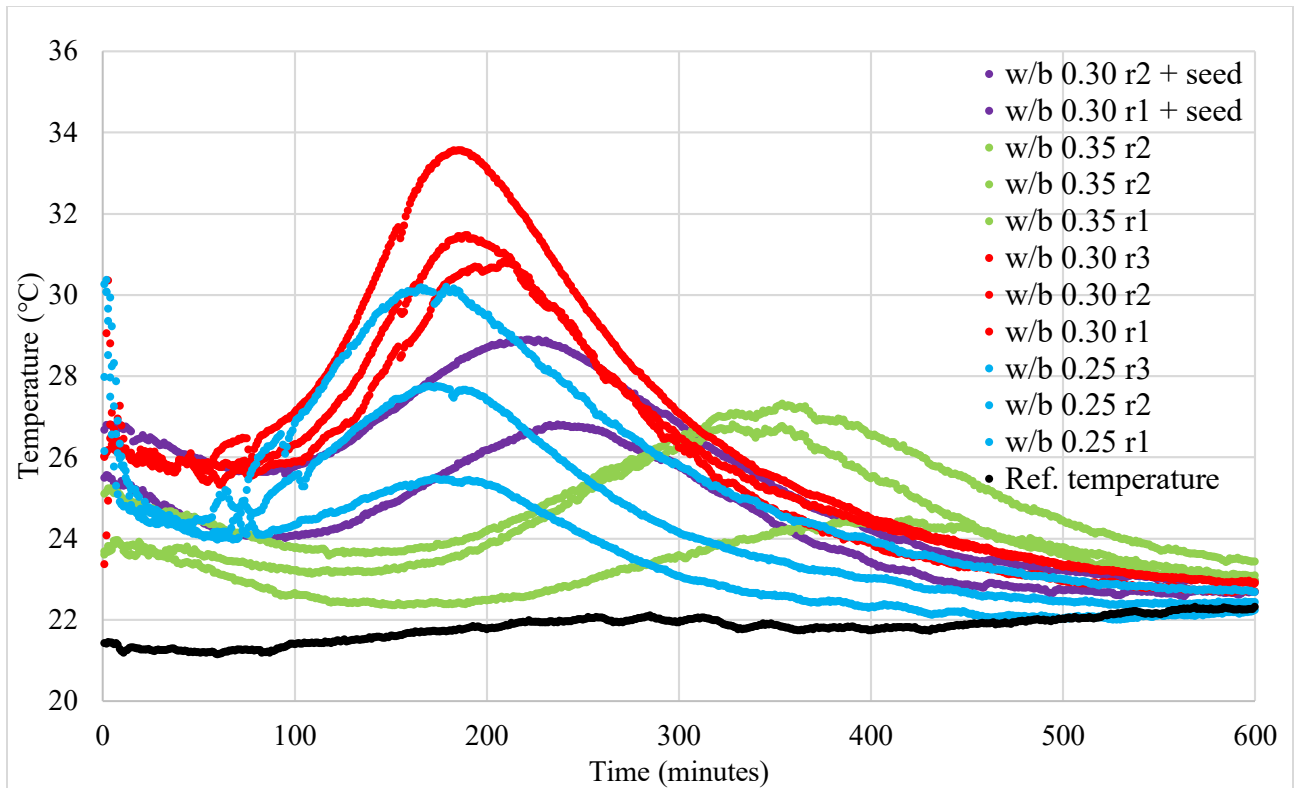


Figure 2.3.2: Hydration kinetics of alkali activated ground blast furnace slag. The alkali solution employed was 6 % NaOH and 12 % water glass (w/w %) at varying w/b. Each color is associated to a water to binder ratio. Reference temperature was measured as the temperature of an empty mold. w/b: water to binder ratio. Ref. temperature is a reference temperature measured using an empty mold.

Table 2.3.2: One-way ANOVA post-hoc test multiple comparisons (Tukey's honest significance test (Tukey's HSD) for alkali activated slag cement cylinders at varying w/b. The mean difference in the compressive strength for water to binder ratios of 0.25, 0.3, and 0.35 is considered. Analysis performed using SPSS (IBM SPSS Statistics, 23, IBM, New York, United States). An asterisk next to the mean difference indicates a P value less than 0.05.

(I) w/b	(J) w/b	Mean Difference (I-J)	Std. Error	Sig.	95% Confidence Interval	
					Lower Bound	Upper Bound
.25	.30	7.67*	2.09	.024	1.25	14.08
	.35	6.67*	2.09	.043	.25	13.08
.30	.25	-7.67*	2.09	.024	-14.08	-1.25
	.35	-1.00	2.09	.884	-7.41	5.41
.35	.25	-6.67*	2.09	.043	-13.08	-.25
	.30	1.00	2.09	.884	-5.41	7.41

Table 2.3.3: Tests of normality for compressive strengths for all 12 observations. a: Lilliefors significance correction. Analysis performed using SPSS (IBM SPSS Statistics, 23, IBM, New York, United States).

	Shapiro-Wilk ^a		
	Statistic	df	Sig.
Compressive strength	.880	12	.086

Table 2.3.4: Tests of normality for compressive strengths of the 9 unseeded observations. a: Lilliefors significance correction. Analysis performed using SPSS (IBM SPSS Statistics, 23, IBM, New York, United States).

	Shapiro-Wilk ^a		
	Statistic	df	Sig.
Compressive strength	.903	9	.267

Qualitatively: Cylinders activated at a w/b ratio of 0.30 reached a higher temperature (5 °C higher) when compared to slag activated at a w/b ratio of 0.25. Peak temperature was reached earlier for slag activated at lower w/b ratios. Peak temperatures were reached at ~ 190 minutes and 350 minutes for w/b of 0.30 and 0.35 respectively when activated with a solution of 6 % NaOH and 12 % sodium silicate (percent mass of binder).

2.4. Discussion

A one-way analysis of variance (ANOVA) was used to determine if the water to binder ratio (factors) significantly affected the compressive strength (dependent variable) of slag activated at a constant molarity of alkali. The treatments are considered to be the water to binder ratio used in mixing the concrete, the control group was the sample having w/b of 0.3. Independent observations are ensured through the use of distinct samples (3 individual cylinders per factor level). Shapiro-Wilk's (1965) test of normality (Table 2.3.3 and Table 2.3.4) verified that the compressive strengths were normally distributed ($p = 0.267 > 0.05$: Table 2.3.4). The null-hypothesis was not rejected; the data was normally distributed. Homogeneity was tested using Bartlett's test as described by Arsham and Lovric (2011). This resulted in a p-value for Bartlett's test of 0.73; the null hypothesis of no significant differences between factor variance could not be rejected (the test's p value was greater than the chosen significance level of 0.05), the variance was homogenous. The value of ω^2 as described by Tomczak and Tomczak (2014) was 0.65. The

independent variable investigated (w/b ratio) accounted for approximately 65 % of the variance in the compressive strength. The experiment was only performed once.

Alkali activated cements having a w/b ratio of 0.25 resulted in greater (by ~ 7 MPa) 20-hour compressive strengths when compared to water to binder ratios of 0.25 and 0.30 (Table 2.3.1). No significant differences (Table 2.3.2) were measured for water to binder ratios of 0.30 and 0.35. No significant differences were measured in the 20-hour compressive strength of seeded and unseeded samples (labeled 0.3 and 0.3 + seed).

Strength is greatest at a lower w/b ratio as reported for purely calcium hydroxide-based alkali-activated slag concretes (Yang et al., 2012). The greatest compressive strength measured was of 20 MPa at 20 hours for a w/b ratio of 0.25 (Figure 2.3.1). C-S-H seeding did not significantly affect compressive strength which is in contradiction with cited literature (Hubler et al., 2011). Poor technique is a possible cause of this discrepancy. Alkali activated cements were not degassed and only lightly washed. At a w/b ratio of 0.25, manually mixing samples became difficult. Dark striations immediately formed upon mixing the activation solution with the slag. Fluidity was lost within seconds especially at higher concentrations of alkali. Shear thickening pastes have highly non-Newtonian behavior. Vibrating the side of molds resulted in a high increase of paste viscosity (qualitatively observed). Higher w/b ratios will decrease the cementing strength of alkali activated concretes but might be justified in a scenario where appropriate distribution of mix is essential for the overall strength of the element. At the concentration of activators used, the onset of uncontrolled setting is due to the formation of a primary C-S-H gel in the early stages of the reaction. This is a result of the Ca^{2+} ions present in the slag binding to the silicate ions in the water glass solution (Palacios et al., 2008).

The delayed heats of hydration observed at greater w/b ratios (Figure 2.3.2) are likely due to the lower pH of water used for activation, as described in Chapter 1. However, to confirm this the initial temperature should be the same for all activation solutions. This was not achieved for this experiment which had differences in temperatures of ~ 15 °C.

2.5. Conclusion

A simple device for the study of cement hydration is described and is used to investigate the binder used in the formulation of permeable concretes. Granulated blast furnace slag (ECOCEM, France) cements reached compressive strengths of ~ 25 MPa after 20 hours when activated with a solution of 6 % NaOH and 12 % sodium silicate (percent mass of binder) at a water to binder ratio of 0.25. At w/b of 0.3 and 0.35, compressive strengths of alkali activated slag cylinders reached ~ 17 MPa. The alkali activated slag studied experienced delayed heats of hydration with equivalent 20-hour compressive strengths when hydrated with a w/b ratio of 0.35. Pastes with higher water content partially mitigated the uncontrolled setting of alkali activated slag.

Connecting Statement for Chapter 3.

The previous chapter established the physical material properties of a cementitious material capable of being used as a binder for the formulation of bio-receptive porous concretes. Chapter 3 uses the alkali activated material studied in Chapter 2 to bind quartz aggregate into various forms. The focus of Chapter 3 is on the permeability of porous concrete. The chapter documents a method for quantifying the air permeability of porous concrete and how to assess a relationship to fluid accessible porosity. This chapter serves to outline procedures which can be used to establish specification data for highly permeable bio-receptive concrete slabs (with pore sizes on the mm to cm length scale).

3. Air Permeability of Bio-receptive Porous Concrete Slabs and Cylinders

3.0. Abstract

The following experiment quantifies the air permeability of alkali activated porous concrete mixes in the turbulent regime. The viscous inertial resistance and the inertial resistance of 0.5 m by 0.5 m by 0.05 m thick porous concrete slabs was evaluated at $122 * 10^6 \text{ m}^{-2}$ & $5.24 * 10^4 \text{ m}^{-1}$, $117 * 10^6 \text{ m}^{-2}$ & $1.83 * 10^4 \text{ m}^{-1}$ and $75 * 10^6 \text{ m}^{-2}$ & $1.31 * 10^4 \text{ m}^{-1}$ for porosities of 0.26, 0.33 and 0.37 respectively. After 40 days of hydroponic turfgrass cultivation using porous concrete having a porosity of 0.37 as a root-zone media, its viscous inertial resistance and the inertial resistance increased to $103 * 10^6 \text{ m}^{-2}$ and $7.3 * 10^4 \text{ m}^{-1}$ respectively.

3.1. Introduction

To date, there is no standard methodology for measuring the permeability of porous concretes. Two commonly used methods for measuring permeability of PCs cited in the literature are the falling head and constant head method and employ water as the working fluid. Permeability is found to be affected by the applied fluid pressure, it is recommended that permeability of PCs should be reported with applied pressure and associated testing method (Andres-Valeri et al., 2018; Sandoval et al., 2017). Established correlations describing the flow through packed beds of granular material and their validity when applied to flows through porous concretes are described in Chapter 1, Section 1.3.

Clogging in permeable concrete is a major issue which causes a decrease in permeability. This consequently affects its functional serviceable lifetime (Kia et al., 2017). In Hitti's (2018) use of PCs as hydroponic substrates, an increasing portion of the pores become occupied by roots during the plant's lifetime as highlighted in Chapter 1, section 1.1. To establish the effect of root growth inside porous concrete, a device was designed to measure the permeability of concrete slabs using air. It was then used to measure the permeability of bio-receptive concrete (Hitti, 2018), prior to, and after its use as a hydroponic growth substrate for the cultivation of turf grass.

3.2. Materials and Methods

3.2.1. Quartz aggregate

Poured random packing of 300 ml of quartz aggregate (Table 3.2.1)(Quarzsand, 2 - 3.2 mm, Carlo Bernasconi AG, Berne, Switzerland) in 1 L graduated cylinder resulted in 38.6 % porosity and 1627 kg m^{-3} with a specific gravity of 2.65. At field capacity the density was measured to be 1705 kg m^{-3} .

Table 3.2.1: 2D image analysis of top projections of 42 aggregate particles (Quarzsand, 2 – 3.2mm, Carlo Bernasconi AG, Berne, Switzerland). Values in (μm).

	Max diameter	Diagonal width	Perimeter	Min diameter	Circle equivalent
Average	3835	3069	11748	2903	3224
Standard Deviation	591	443	1607	411	421
Max	5340	4284	14696	3814	4055
Min	2128	1832	6790	1793	1846

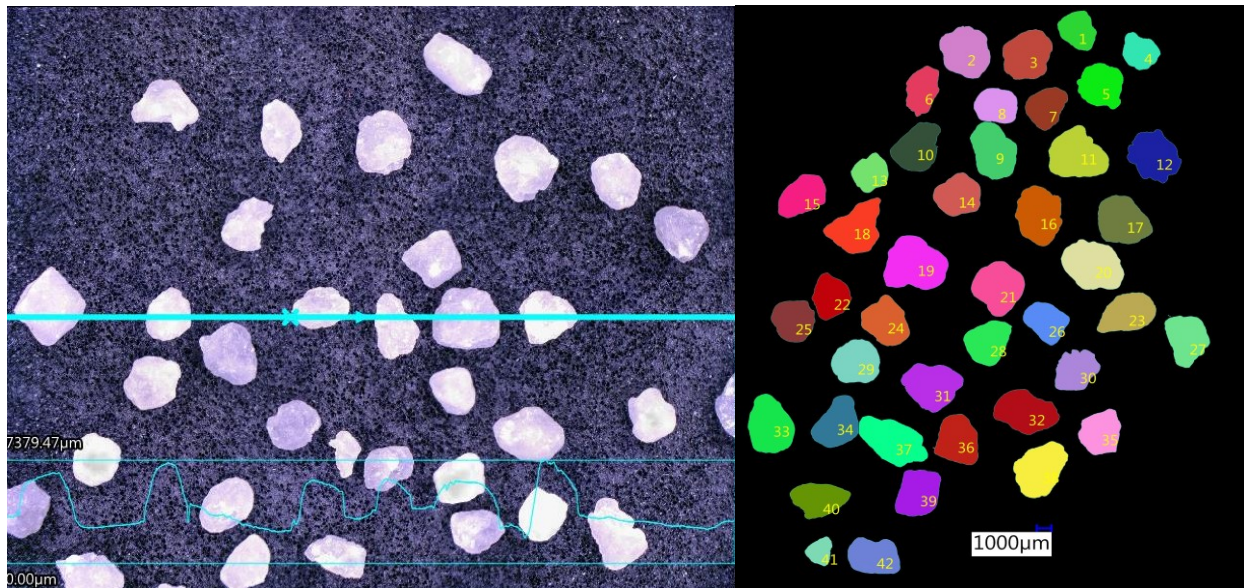


Figure 3.2.1: Quartz aggregate used to make the porous concrete samples. Left: Physical appearance of aggregate (Quarzsand, 2 – 3.2 mm, Carlo Bernasconi AG, Berne, Switzerland). Right: Overview of the 42 individuals randomly chosen for 2D image analysis.

3.2.2. Permeable Alkali Activated Concrete

Aggregate (Figure 2.3.2) and binder (Chapter 2, Table 2.2.1) mass were determined using a digital scale (defender 3000, OHAUS, New Jersey, United States). A concrete mixer (SM2 – 650, Colomix, Gaimersheim, Germany) was used for incorporating slag, aggregate and alkali solution. Activators were dissolved in water prior to being added to aggregate and slag. Aggregate and binder were mixed separately for 20 ± 10 seconds prior to adding solution. Solution was added at a constant rate not exceeding 20 ml s^{-1} . All forms were filled to desired volume at low compaction. Samples removed from molds after curing at room temperature ($25 \pm 10 \text{ }^\circ\text{C}$) or in a curing chamber set to $25\text{C} \pm 2 \text{ }^\circ\text{C}$ with relative humidity of $98 \pm 2 \%$ for a minimum of 14 days.

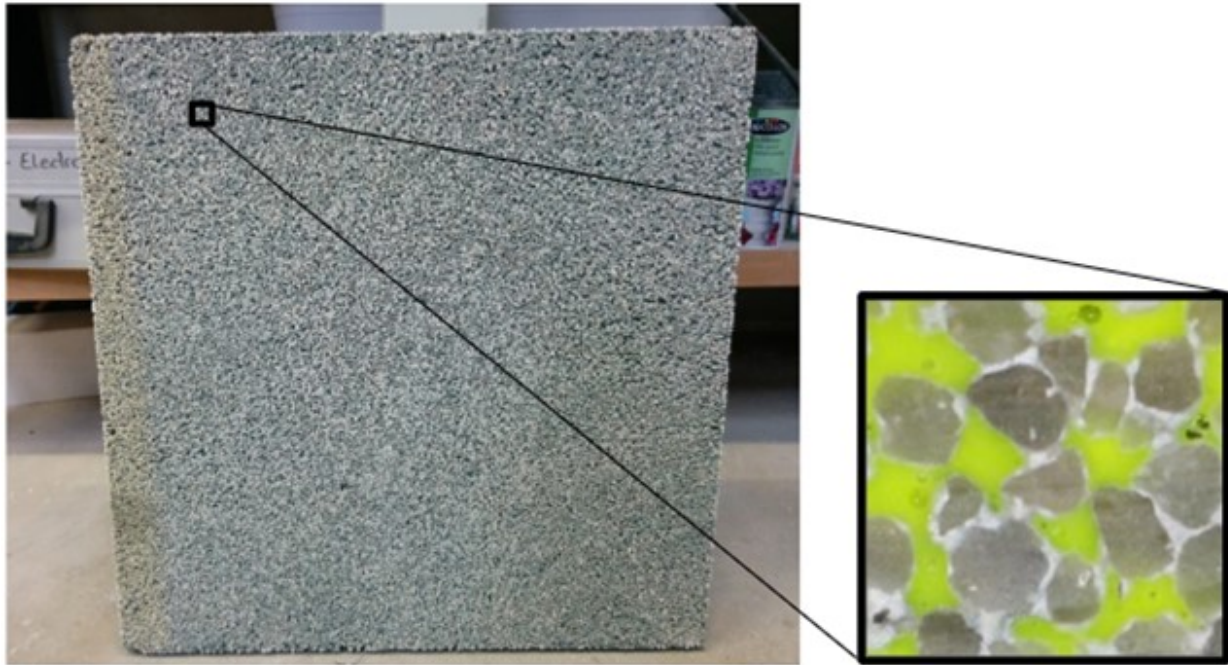


Figure 3.2.2: Geometry and physical appearance of porous concrete slabs. Samples 1 - 3 and 5 - 6 were similar to the one depicted in this photo. This sample had void fraction of 0.35. The size of the sample on the left was 0.5 m by 0.5 m by 0.05 m thick. The image on the right is a cut portion of the sample impregnated with pigmented two-part epoxy and is approximately 1.5 by 1.5 cm.

3.2.3. Porosity

Effective porosity is measured according to Equation 3.2.1:

$$\epsilon = \frac{V_V}{V_T} \quad (\text{Equation 3.2.1})$$

Where V_v is the volume of voids. This was obtained by subtracting V_{solids} as measured using the suspended water displacement method (Hughes, 2005) from V_{total} which was calculated from

sample dimensions measured using Vernier calipers (Series 530, Mitutoyo, Sakado, Japan). Samples were oven dried before submersion. In this thesis, porosity is also denoted in percent, in which case the value is equal to Equation 3.2.1 multiplied by 100 %.

Porosity by image analysis (Table 3.3.1) was performed (Mishra et al., 2013). Pieces with volumes greater than $3.8 * 10^3 \text{ mm}^3$ were placed in silicon molds and impregnated with epoxy resin. The epoxy was dyed with fluorescent pigments to increase the contrast between the concrete material and the epoxy filling its voids. Epoxy in concrete was vacuum cured to diminish the inclusion of bubbles. Samples were then sliced using a diamond disk saw (Minitom, Struers, Ballerup Denmark), the circular blade lubricated with ethanol.

3.2.4. Bulk Density

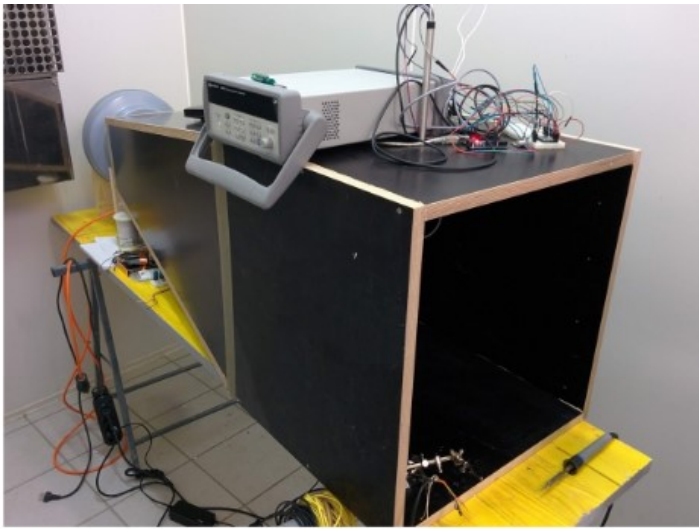
The bulk density was measured by dividing the dry mass of the porous concrete specimen by its total volume. The measurement was adapted from ASTM standard C1754/1754M (2012) (standard test method for density and void content of hardened pervious concrete). The only difference being the sample size (physical).

3.2.5. Experimental Setup, Data Collection and Permeability

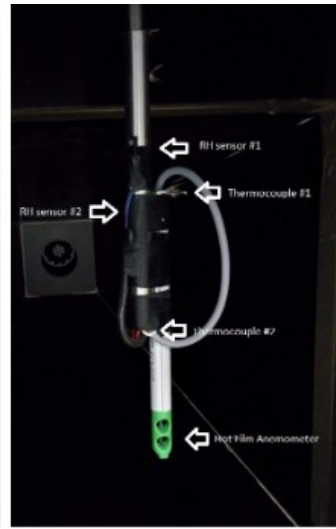
A test apparatus (also referred to as wind tunnel for the remainder of this thesis) was designed to maintain a steady pressure drop across one of the 0.5 m by 0.5 m sample sides as depicted in Figure 3.2.3. The sensors incorporated in the wind tunnel measured temperature ± 2.5 °C (Thermocouple type K extension grade, OMEGA, Biel, Switzerland), relative humidity ± 3 % (HH-4021-00, Honeywell, North Carolina, United States), pressure ± 12 Pa (BMP280, Bosch Sensortec, Reutlingen, Germany), and air velocity (with a relative accuracy of $\pm 0.01 \text{ m s}^{-1} + 5$ % of the reading) (SDL350 hot wire CFM thermo-anemometer, Extech, Massachusetts, United States). They were used to assess the change in the air properties after flowing through the PCs. The interface exposed to the air prior to flowing through was referred to as the inlet and the interface from which the air exited was referred to as the outlet. The apparatus was placed inside a curing chamber (Ineltec model CM – 50 m³, fabrication number 055/2006, 6.5 KW, Barcelona, Spain) to minimize variation of inlet temperature and humidity. A 148 W ducting fan (ERR 25/1, MAICO, Villingen-Schwenningen, Germany) was used to drive pressure drops across slabs (0.5 m by 0.5 m) of varying porosities (0.25 - 0.40) and thickness (0.05 m - 0.07 m). The size of a sample is considered adequate when they behave as representative elementary volumes (REV). Tests performed on REV's lead to equivalent averaged results (Mosthaf et al., 2014). For more

complex phenomena, large spatial discrepancies of this system (binder-aggregate-air interfaces) introduce uncertainty in equations for which properties are averaged over a representative element of volume (Perre, 2010). Sample thickness was greater than 10 times the size of the largest aggregate. Fully developed flow predominated within the matrix. The properties of air at 1 atmosphere and 20 °C were used for calculating permeability coefficients. The contribution of relative humidity was not studied.

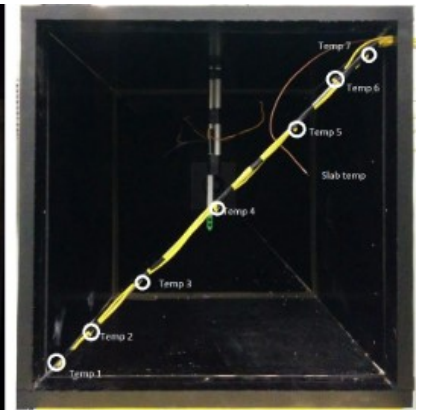
The cross-sectional velocity was determined by averaging 16 equally spaced measurements (Figure 3.2.3 bottom left) over the 0.25 m² interface exposed to atmospheric pressure (inlet). Individual measurements were time averaged over 30 ± 10 seconds and obtained using a hand-held hotwire anemometer. Individual measurements were taken 0.5 cm from the surface of the slab in the direction perpendicular to the surface. The measured pressure drop across the slab during measurements was determined by the difference in absolute pressure as measured by the sensor before fan operation and once pressure readings stabilized to ± 10 Pa over 20 seconds during fan operation. The pressure was measured 5 cm away from the top center of the back of the slab (inside the wind tunnel). Constriction of air flow downstream from the back of the slab was 0.5 m away and extended over 1 m at 9 degrees before reaching the fan. A combination of digital and analogue sensors were used to collect experimental data. The analogue sensors used were the relative humidity sensors and the thermocouples which were both connected to a data logger (Agilent data logger, 34970A, Keysight Technologies Canada Inc., Mississauga, Ontario, Canada). The digital pressure sensor was connected to a microcontroller (Arduino Uno R3, Massachusetts, United States) which logged the absolute pressure.



Wind Tunnel, 147W fan



Anemometer, RH and Temperature sensors



Air Temperature Array

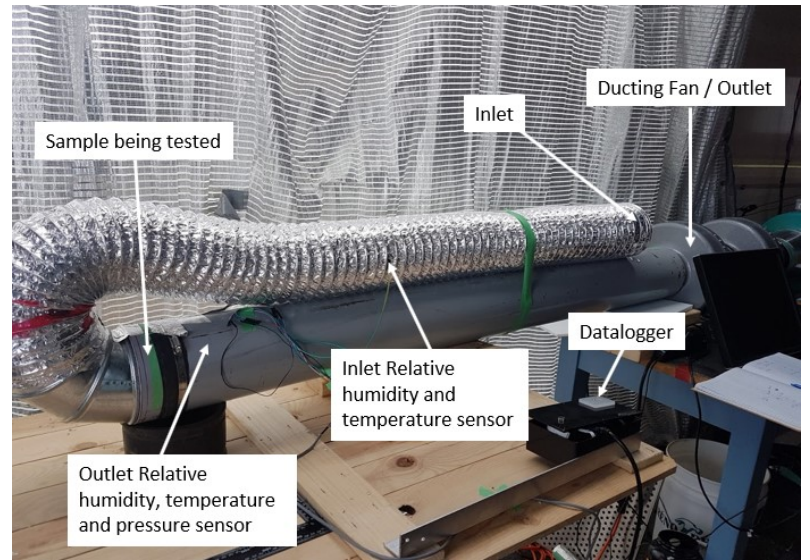


Figure 3.2.3: Experimental setups (wind tunnels) used for measuring permeability. Top and bottom left: Experimental setup for testing samples 1 - 6. Average air flow through samples was calculated by area averaging the results taken at each point where lines crossed (bottom left). Top right: Sensor placement for top left experimental setup. The array of thermocouples (top right) were located at 3.5, 9.75, 19.5, 35.5, 51.5, 61.0 and 67.2 cm from the bottom left along the diagonal line connecting the bottom left to the top right of the wind tunnel. Bottom right: Experimental setup for testing samples 12 and 13.

Table 3.2.2: Mix design for porous concretes made with alkali activated slag. Proportions of binder, aggregate and activators used were obtained using a porous concrete calculator tool (Pervia Tool, 170330, CEMEX Research Group AG (CRG), Brugg, Switzerland). Samples 1 to 3 were tested on a different wind tunnel than samples 11 and 13. N. A. stands for not available and x represents a value of 0. Bernasconi is a quartz aggregate (Quarzsand, 2 – 3.2mm, Carlo Bernasconi AG, Berne, Switzerland). Poraver is an expanded glass foam aggregate (Poraver, 2 – 4 mm, Poraver, Schlüsselfeld, Germany). Water glass is a sodium silicate solution of Na₂O ~ 10.6 % & SiO₂ ~ 26.5 % (Sigma Aldrich, Missouri, United States). ECOCEM is ground granulated blast furnace slag (ECOCEM, France). Icons for sample cross sections represent the geometry perpendicular to the flow of air.

Sample	#1	#2	#3	#4	#5	#6	#7	#8	#9	#10	#11	#12	#13
Targeted porosity	0.20	0.25	0.30	0.30	0.30	0.35	0.20	0.25	0.30	0.35	0.20	0.30	0.30
ECOCEM (kg)	4.32	3.35	2.37	3.31	x	1.40	0.680	0.521	0.460	0.22	N.A.	x	x
CEMII (kg)	x	x	x	x	2.487	x	x	x	x	x	x	N.A.	N.A.
Bernasconi 2 - 3.2 mm (kg)	18.4	18.6	18.7	26.1	18.4	18.9	2.90	2.92	3.70	2.97	x	x	x
Poraver 2 – 4 mm (kg)	x	x	x	x	x	x	x	x	x	x	N.A.	x	x
Water (kg)	1.097	0.860	0.624	0.870	0.651	0.388	0.19	0.150	0.139	0.066	N.A.	N.A.	N.A.
NaOH _(aq) : 50 % by mass (kg)	0.159	0.123	0.871	0.121	x	0.051	0.014	0.011	0.095	4.5	N.A.	N.A.	N.A.
Water glass (kg)	0.233	0.181	0.128	0.179	x	0.076	0.033	0.027	0.024	0.013	N.A.	N.A.	N.A.
Sample cross-section	■	■	■	■	■	■	●	●	●	●	●	■	■
Thickness (cm)	5	5	5	5	5	7	9.8	9.7	9.3	9.2	9.2	4.6	4.6
Side of square or diameter (cm)	50*50	50*50	50*50	50*50	50*50	50*50	15.2	15.2	15.2	15.2	15.2	33*27	33*23
Aggregate size (mm)	2-3.2	2-3.2	2-3.2	2-3.2	2-3.2	2-3.2	2-3.2	2-3.2	2-3.2	2-3.2	2-4	2-7	12.7

3.2.6: Biological Clogging

Two permeable concrete slabs having the same mix design and dimensions as sample 3 (Table 3.2.2) were casted and left to cure sealed at ambient temperatures for two weeks. Grass

(Quick Turf Royal Coat, Eric Schweizer AG, Switzerland, Steffisburg) was then seeded on the two slabs. During the growth period one slab was placed in a horizontal position (Figure 3.2.4) while the other was oriented vertically (Figure 3.2.5). The horizontally resting slab was immersed up to 85 % of its height in Hoagland solution (with salt concentrations multiplied by two) (Hoagland, 1948). The amount of grass seeds applied was 10 times greater than the amount specified by the manufacturer. Seed were covered with paper cloth until shoots were 5 mm long (Figure 3.2.4, day 3). Nutrient solution was fully changed on a weekly basis. Grass was trimmed to be 5 cm long at various times during its growth (Figure 3.2.4, day 26). For the vertically oriented slab, grass was sown in a horizontal position. The slab was placed upright and continuously irrigated from the top through a tube connected to an aquarium pump (400 / 7 W, Migros, Zürich, Switzerland). The nutrient solution was recirculated and changed on a weekly basis. Both seeded samples were grown under a high-pressure sodium (HPS) lamp as depicted in Figure A.2.

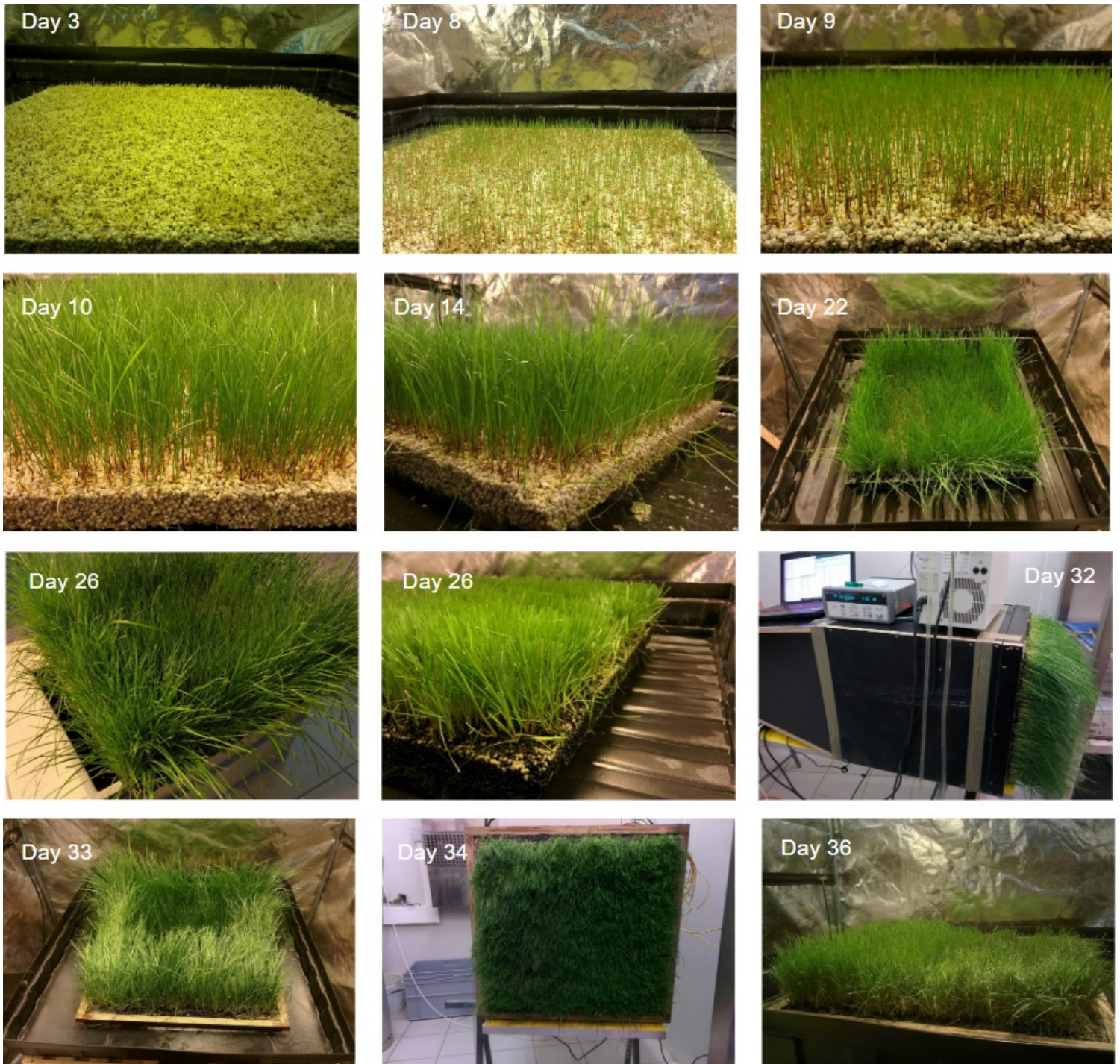


Figure 3.2.4: Grass grown under high pressure sodium lighting. Plant nutrients supplied using 2X hydroponic solution.

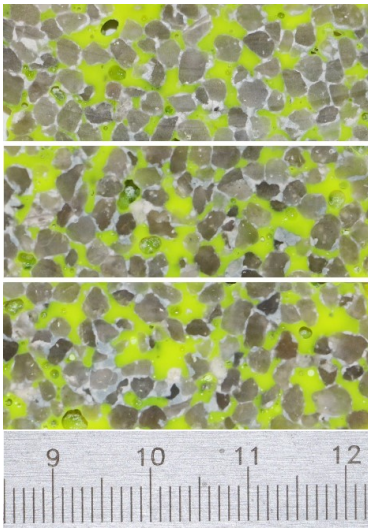
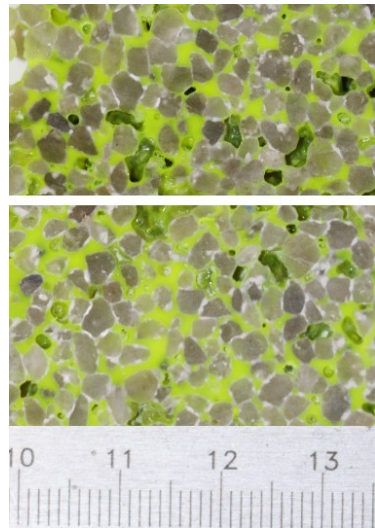
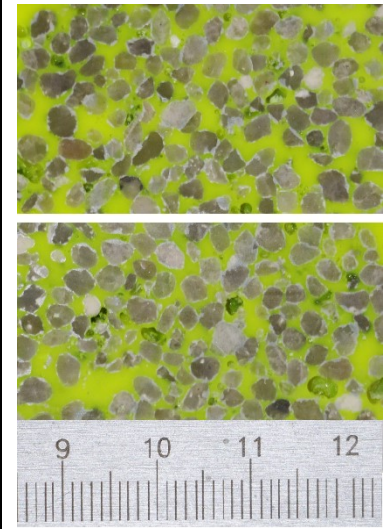

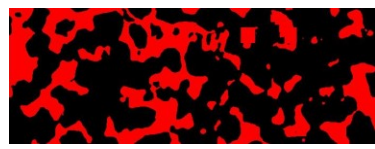
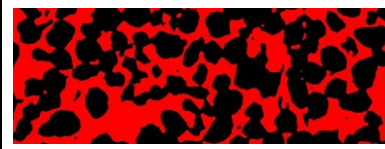


Figure 3.2.5: Vertically grown grass on permeable alkali activated porous concrete.

3.3. Results

3.3.1. Porosity

Table 3.3.1: Image processing of porous concrete cross-sections. Pictures were taken, then digitally processed to calculate void fractions. Images are not to scale. The yellow color was from the epoxy and the red color was generated using computer software (Inkscape). Shadows caused by defects (areas not filled with epoxy) were manually corrected post processing to increase precision. Values of porosities measured by water displacement agree with values measured by image processing within ± 0.02 (void fraction). All measurements were for areas greater than $(10 * \text{largest sieve})^2$.

Sample	1	2	3
Porosity by water displacement	0.25	0.33	0.37
Volume (L)	0.82	0.72	0.98
Sample images before software processing			
Monochromatic output after image processing.			
Area of processed image (cm ²)	12	16	13
Porosity by image analysis (area _{red} /area _{total})	0.263	0.334	0.350

3.3.2. Air Permeability

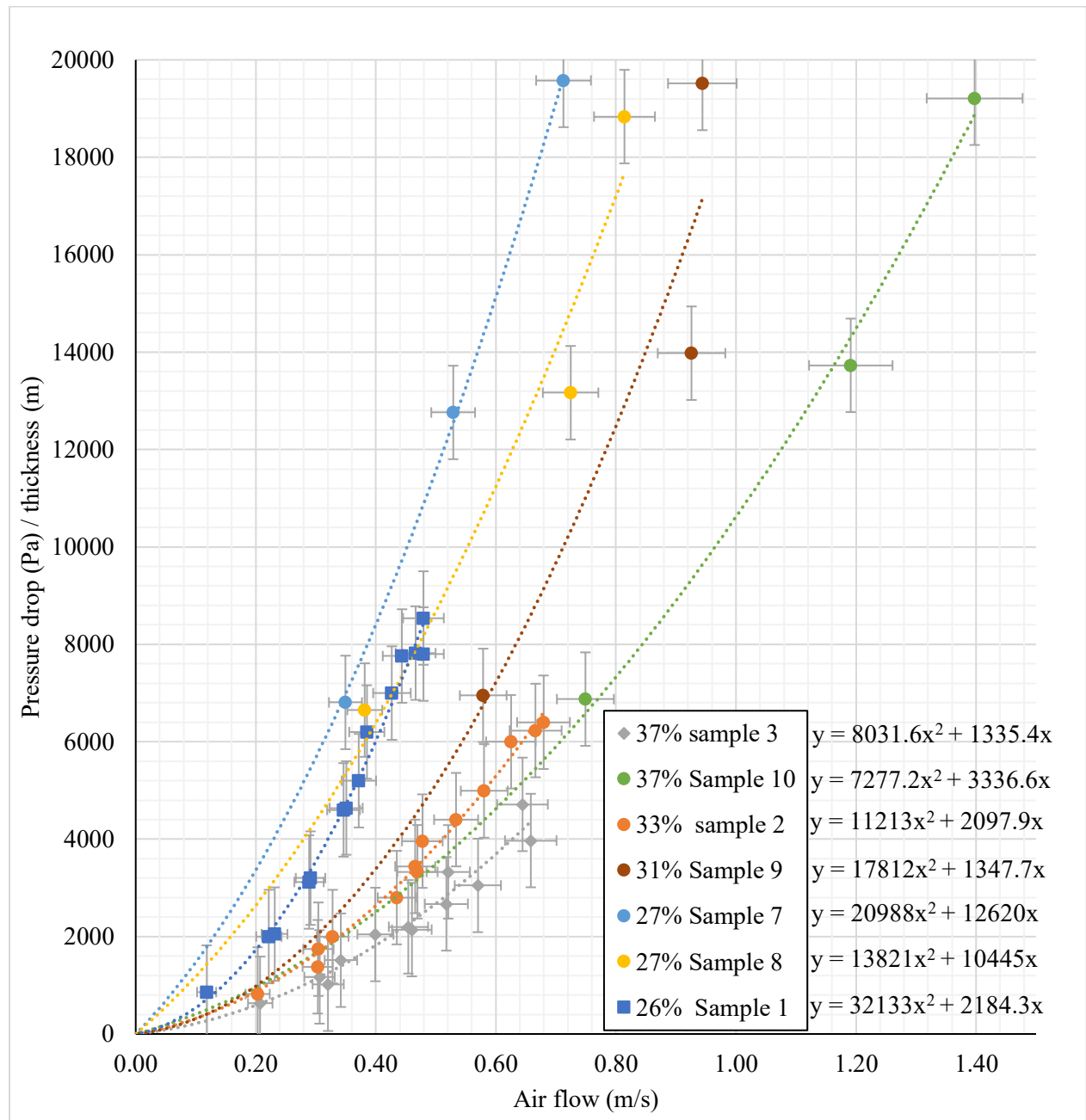


Figure 3.3.1: Non-Darcy flow in alkali activated granulated blast furnace slag porous concretes. Permeability is described as the coefficients of the second order polynomial equations. For $y = A x^2 + B x$ the inertial resistance was obtained by multiplying A by 2 and dividing by the density of the working fluid. The viscous inertial resistance was obtained by dividing B by the dynamic viscosity of the fluid. viscous inertial resistance is the inverse of permeability. The R -squared (R^2) values for sample 1, 2, 3, 7, 8, 9 and 10 are 0.986, 0.988, 0.945, 0.999, 0.939, 0.847 and 0.993 respectively. Horizontal bars show the anemometer accuracy ($\pm 0.01 \text{ m s}^{-1} + 0.05 x$). Vertical bars are \pm two times the pressure sensor's relative accuracy scaled with thickness (960 pa m^{-1}).

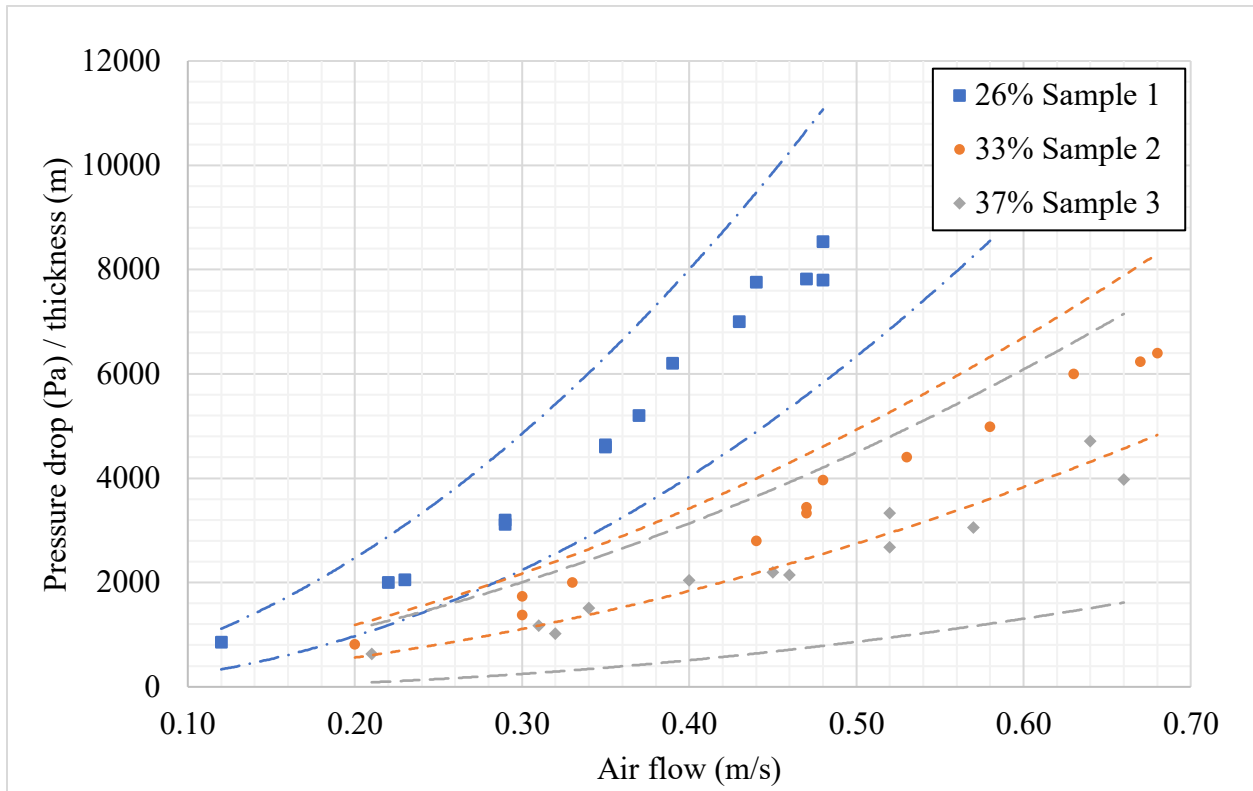


Figure 3.3.2: 95 % confidence intervals for second order polynomial regressions. The lower and upper bounds were obtained for samples 1 to 3 using SPSS (IBM SPSS Statistics, 23, IBM, New York, United States). For $y = A x^2 + B x$, A and B takes values of 26001 and -334 for the lower bound; 38263 and 4699 for the upper bound of sample 1. Likewise, the values of the bounds for sample 2 are 8952 and 1016; 13068 and 3326. For sample 3 they are 4510 and -529; 11529 and 3224.

Table 3.3.2: The Kruskal-Wallis H test for pressure drop and average cross-sectional velocity in the ranges of 0.2 to 0.5 $m s^{-1}$. The test was conducted using SPSS (IBM SPSS Statistics, 23, IBM, New York, United States).

	Pa m ⁻¹
Chi-Square	13.986
df	2
Asymp. Sig.	.001

Table 3.3.3: Physical properties of porous concrete samples.

Sample	#1	#2	#3	#4	#5	#6	#7	#8	#9	#10	#11	#12	#13
Actual porosity	0.26	0.33	0.37	N.A.	N.A.	0.40	0.27	0.27	0.31	0.37	0.46	0.25	0.31
Viscous inertial resistance factor (α^{-1}) (m^{-2})	122E6	117E6	75E6	N.A.	N.A.	N.A.	N.A.	N.A.	N.A.	N.A.	N.A.	112E6	67E6
Inertial resistance (C_2) (m^{-1})	5.24E4	1.83E4	1.31E4	N.A.	N.A.	N.A.	N.A.	N.A.	N.A.	N.A.	N.A.	5.93E3	2.36E3
Volume (L)	12.5	12.5	12.5	17.5	12.5	12.5	1.72	1.69	1.72	1.70	1.61	3.5	3.5
Bulk density ($k m^{-3}$)	1844	1665	1638	N.A.	N.A.	N.A.	1783	1775	1745	1591	N.A.	N.A.	N.A.

The viscous inertial resistance factor and the inertial resistance factor (Table 3.3.3) were determined according to the calculation procedure described by Nowak (2016) with the properties of air at 15 °C and 101.33 kPa (density equal to 1.225 kg m^{-3} and viscosity equal to $1.789 \cdot 10^{-5} \text{ kg m}^{-1} \text{ s}^{-1}$ (Çengel & Boles, 2001)).

3.3.3. Biological Clogging

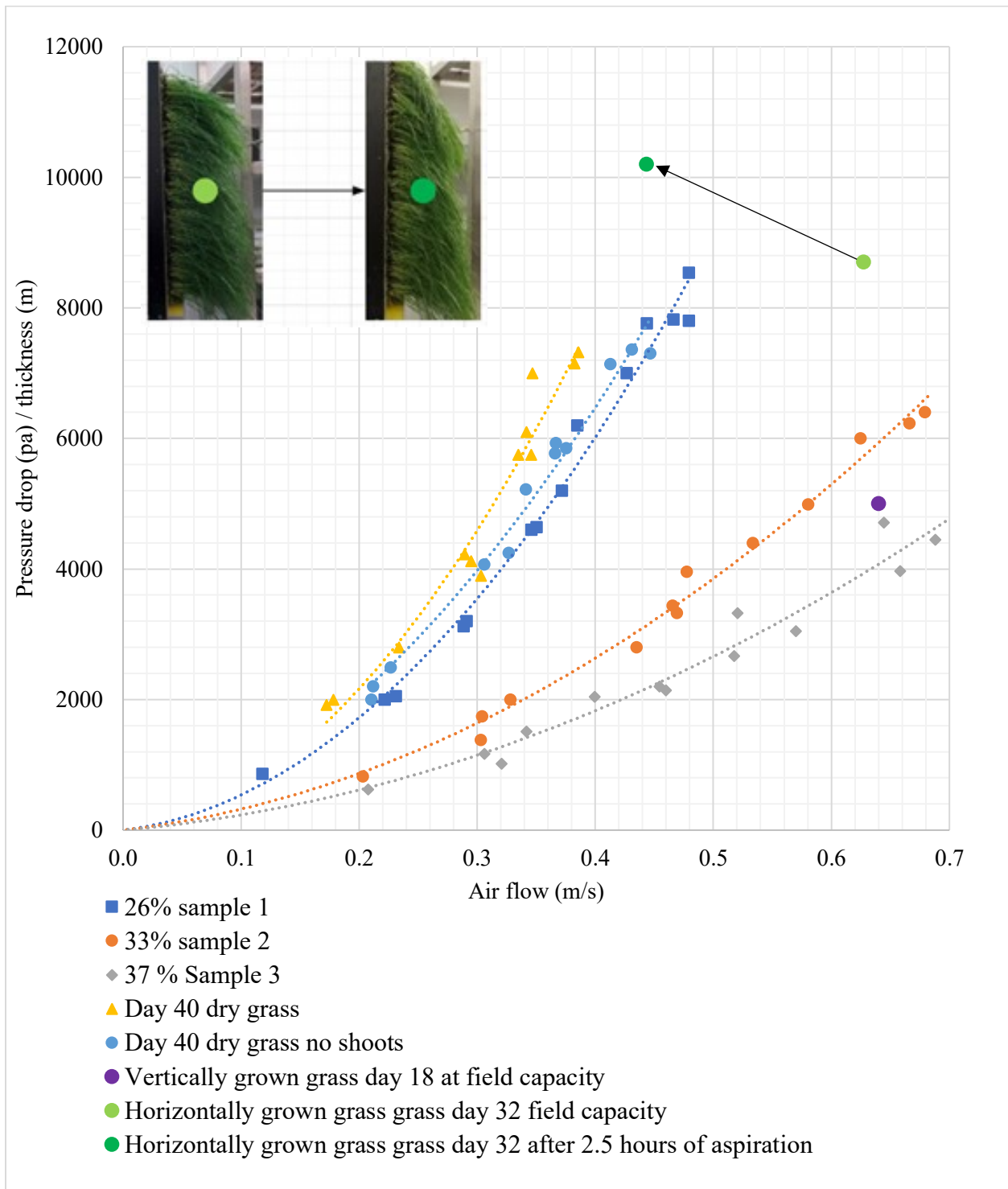


Figure 3.3.3: Biological clogging of bio-receptive porous concrete samples by turfgrass. Samples having 26 %, 33 % and 37 % porosity are included as reference points. Equations for day 40 dry grass and day 40 dry grass with no shoots are $y = 44867 x^2 + 1850.3 x$ ($R^2 = 0.954$) and $y = 29220 x^2 + 4487.2 x$ ($R^2 = 0.981$) respectively.

3.4. Discussion

The curves plotted in Figure 3.3.1 can be used to model various mix design (Table 3.2.2) permeabilities (Table 3.3.3). Sample 3 behaved like a packed bed of 3.08 mm diameter spheres as can be seen when comparing the data for columns packed with spheres (Burke and Plummer, 1928) (Appendix Figure A.1). Sample 1 behaved like a packed column of 1.48 mm spheres. Increasing the amount of binder in the porous concrete mixed resulted in permeabilities lower than the ones measured for spheres having diameters equivalent to the average diameter of the aggregates used.

During mixing of permeable concretes, spherical aggregates are surface coated with the binding material. This can result in higher than targeted porosities, if zero to low compaction is used. Spherical particles may be arranged in different ways, e.g. they may have a loose packing (cubic arrangement, $\varepsilon = 47.64\%$) or dense packing (hexagonal arrangement, $\varepsilon = 25.95\%$) as explained by (Amhalhel and Furmański, 1997). The porosity of close random packing and poured random packing of spheres range from 36 % to 39 %. These values can be achieved for PCs using spherical quartz aggregates.

The design mix of sample 3 decreased to 72 % of its original permeability after 40 days of growth (Figure 3.3.3). Grass (15 cm long) was ~ 25 % less permeable after being aspirated for 2.5 hours. After 18 days of growth the vertically oriented sample did not significantly decrease in permeability. Most loss in permeability for dried grass was a result of biomass crust (algae) on the surface of the sample and the roots within the porous matrix (Figure 3.4.1).

Values obtained for permeabilities are two orders of magnitude higher when compared to the ones from various other sources in the literature (Neithalath et al., 2010). A potential reason for this difference might be associated with the wall effect in packed columns (Mehta and Hawley, 1969). Near the container wall of a packed beds of spheres, the porosity increases exponentially which causes a tunneling effect. This can result in an increase of the overall system's permeability and is especially the cases when the ratio of the column to particle diameter is less than 50 to 1. How this translates to the effect on porous concrete columns remains to be determined. If the aggregate size was to be used as a reference, permeability would cease to decrease appreciably when increasing the diameter of a 22.5 cm (diameter) column, highlighting the fact that the permeability of porous concrete is not only dependent on pressure but also the testing methods employed (Yinghong et al., 2015).



Figure 3.4.1: View from underneath slab and cross section of roots after drying.

The significance of the coefficients describing the permeability of samples 1 to 3 as obtained from the apparatus depicted in the top of Figure 3.2.3 was assessed using an independent-samples Kruskal-Wallis test as described by Ostertagová et al. (2014) (Table 3.3.2). The independent variable (factor) for this test was the slab's label (sample 1 - 3). The depend variable was assumed to be all possible pressure drops per unit of thickness a given slab can experience over an equal range of airflows. The range was chosen to be from 0.2 to 0.5 m s⁻¹. All measurements depicted in Figure 3.3.2 which were not in this range were removed prior to conducting the statistical test (data from Table A.3). The control group was considered to be the slab labeled sample 3. All observations were independently collected. The Kruskal-Wallis test was chosen as a non-parametric alternative to an ANOVA because data for the depend variable (chosen to be pressure drop per unit of thickness) violated assumptions of normality and homogeneity as determined by Shapiro-Wilk's (1965) test of normality (significances of 0.08 for all values and 0.226, 0.753 and 0.752 for slab's 1 to 3 respectively) and Levene's (Olkin, 1960) test of equal variance (with a significance of 0.02). Post hoc pair-wise comparison of the Kruskal-Wallis test (a series of Mann-Whitney tests as implemented by SPSS (Bergmann et al., 2000)) revealed that a significant difference was observed for samples 1 and 3, and samples 1 and 2.

From the box plot (right of Figure 3.4.2) the validity of this test was determined to be compromised. The assumption of similar group distribution for the Kruskal-Wallis test is invalid (slightly) due to discrepancies in group 3 (having a relatively lower median and shorter distance in between the third quartile and the maximum value). The results indicate that the experimental device was sensitive enough to consider a meaningful difference between concrete slabs labeled sample 1 and 3, and sample 1 and 2. The same conclusions can be made by considering the curves having non overlapping 95% confidence intervals in Figure 3.3.2. The effect size is large, the value for η^2 as described by Tomczak and Tomczak (2014) was determined to be 0.538 (half way in between no relationship and a perfect relationship).

To ensure that the slabs (groups) were subjected to equal airflows within the range of 0.2 to 0.5 m s⁻¹ Welch's (1951) ANOVA (due to unequal sample sizes) was conducted prior to applying the Kruskal-Wallis' test mentioned above. Welch's ANOVA considered airflow as the dependent variable, and the sample label as the factor (group). The null hypothesis was that for the data obtained within the considered range, slabs experienced similar mean cross-sectional velocities for the pressure drops measured. In between group test for normality (significances of 0.302, 0.151 and 0.896 for samples 1 - 3) and Levene's test of equal variance (significance of 0.428) indicated that the data was normally distributed and had equal variance. From Welch's test (having a significance of 0.736: $p > 0.05$, Table 3.3.2) the null was accepted: the mean value of airflows experienced by all groups did not differ for the data included in Table A.4.

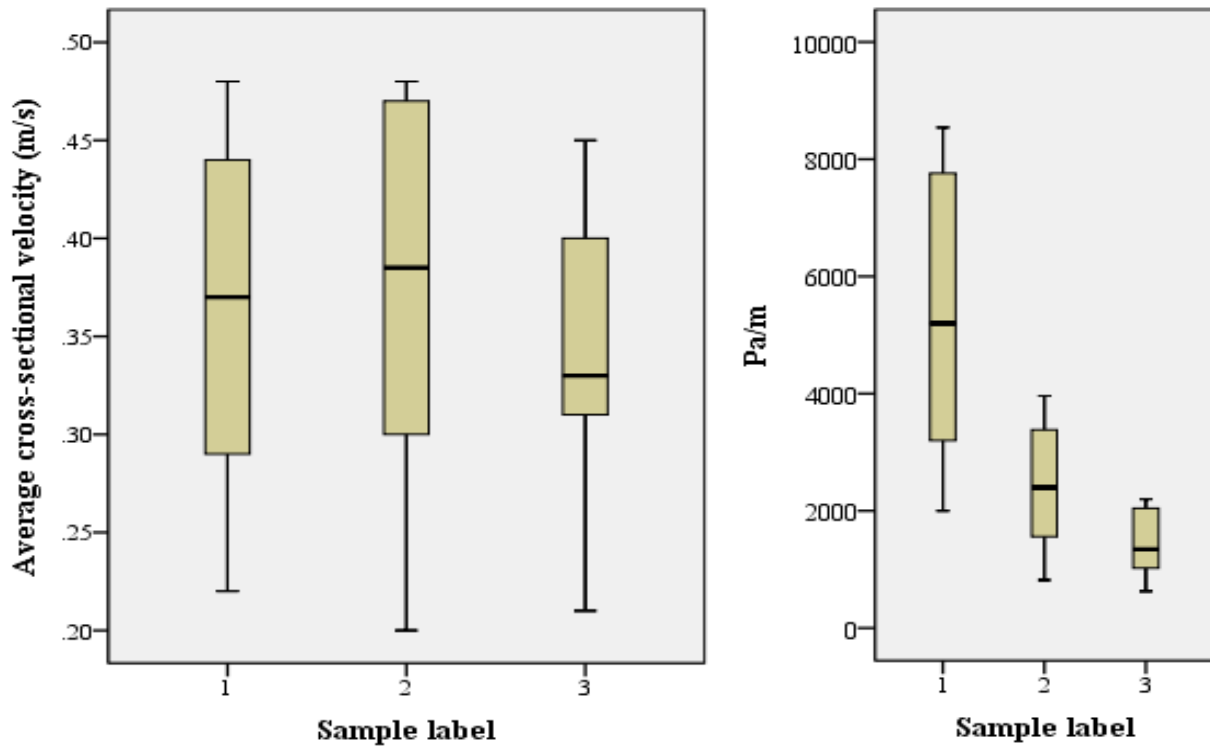


Figure 3.4.2: Stem and leaf plots for the pressure drop and velocity data in the range of 0.2 to 0.5 m s⁻¹.

3.5. Conclusion

This chapter developed the methodology for determining the permeability of porous concretes using air in the turbulent regime. It was then applied to various bio-receptive mix designs. The permeability of (AGBFS) porous concretes was determined for slabs made using 2 - 3.2 mm quartz aggregates at varying binder contents. The bio-receptive porous concrete's permeability decreased by 46 % when the porosity was decreased from 0.37 to 0.33 due to the addition of binder. After 40 days of growing turfgrass in bio-receptive porous concrete the material's air permeability decreased to approximately 72 % of its original value. The permeability and the form drag (inertial resistance) of 0.5 m by 0.5 m by 5 cm thick porous concrete slabs using air was evaluated at $122 \cdot 10^6 \text{ m}^{-2}$ & $5.24 \cdot 10^4 \text{ m}^{-1}$, $117 \cdot 10^6 \text{ m}^{-2}$ & $1.83 \cdot 10^4 \text{ m}^{-1}$ and $75 \cdot 10^6 \text{ m}^{-2}$ & $1.31 \cdot 10^4 \text{ m}^{-1}$ for porosities of 0.26, 0.33 and 0.37 respectively. This chapter also demonstrates the possibility of growing plants in porous concrete on a vertical surface.

Connecting Statement for Chapter 4

Chapter 3 dealt with the permeability of bio-receptive porous concretes made with alkali activated materials (AAM) at low water to binder ratios (~ 0.25 w/b). At higher water contents, cement paste starts to flow over aggregates under the action of gravity. An ideal porous concrete mix that optimizes both strength and permeability would have a water to binder ratio that will coat and clump onto aggregates evenly and not appreciably flow before the setting is complete. Research aimed at determining the effect of water to binder ratio on the material properties of alkali activated slag porous concrete is needed. Chapter 4 documents the effect of two w/b ratios on the air permeability of an alkali activated porous concretes mix design taken from *Bio-receptive ground granulated blast-furnace slag porous concrete substrate* (Hitti, 2018).

4. The Effect of Water to Binder Ratio on the Permeability of Porous Concretes

4.0. Abstract

The permeability of porous concrete cylinders (152 mm diameter by 50 mm thick) made using metallurgical slag (ECOCEM, France) activated with an aqueous solution of sodium silicate and sodium hydroxide (at 5.5 % and 1.9% weight of slag respectively) at a water to binder ratios of 0.25 and 0.35 was quantified. The viscous inertial resistance factor obtained for mixes having w/b ratio of 0.25 and 0.35 was $7.67 * 10^8 \text{ m}^{-2}$ and $2.05 * 10^8 \text{ m}^{-2}$ while the inertial resistance factor was $2.8 * 10^4 \text{ m}^{-1}$ and $5.3 * 10^4 \text{ m}^{-1}$ respectively. Increasing the w/b ratio from 0.25 to 0.35 increased permeability. The bulk density and porosity of the resulting cylinders were not significantly affected.

4.1. Introduction

As discussed in Section 1.3, increasing water to binder ratio typically decreases permeability. Aggregate size modulates the effect varying water to binder ratio has on permeability. With larger aggregates at a porosity of 50 %, (9.5 mm) varying water to cement ratio (from 0.35 to 0.45) decreased permeability by 0.2 mm s^{-1} . It decreases by 0.3 mm s^{-1} for 3.2 mm aggregate (Tun Chi et al., 2014). Confounding results were reported at lower porosities (~ 15 %): Varying water to cement ratio from 0.25 to 0.31 increased permeability by up to 5 mm s^{-1} for aggregates sized 4.75 - 9.5 mm, 9.5 - 16 mm, 16 - 19.5 mm (Yang et al., 2018). The discrepancy is likely caused by the rheological difference between paste types influencing aggregation behavior during mixing. The latter of the two studies was conducted through a lower w/b ratio range.

With regards to the effect of water to binder ratio on the permeability of alkali activated porous concrete, much less literature is available. A set of samples at 20 % porosity for which increasing water to binder ratios from 0.35 to 0.45 decreased water permeability by only 0.15 mm s^{-1} (from 4.30 to 4.21 mm s^{-1} respectively) for an aggregate size of 4.8 - 6.4 mm is reported (Tun Chi et al., 2014). This effect remains undocumented for AAMs at lower water to binder ratios. These samples are difficult to mix and often exhibit clumping. Handling of these materials in the fresh state can be challenging. It is partly due to the current unavailability of efficient rheological control agents (Provis, 2018). Higher mixing shear breaks binder clumps and results in a more

homogeneous cement distribution over the aggregate but is often only consistently achieved for smaller batches.

4.2. Materials and Methods

Molds were made from plastic piping (with an inner diameter of 6 inches) cut into sections ~ 5 cm thick. The volume and mass were calculated by water displacement and using a digital scale respectively (Section 3.2.4). The porous concrete samples were casted inside the molds and cured sealed for 4 months (refer to Figure 4.2.1 for mix design). Aggregate (Section 3.2.1) was added into a bucket and finely ground slag (Section 2.2.1) evenly dispersed over it. The bucket was shaken with a few hand taps to incorporate the slag. Activators (Section 2.2.2) were weighed and dissolved into the water used for hydrating the cement. The resulting solution was poured into the bucket containing the aggregate and slag. Ingredients were hand mixed using a small spade until a visually uniform mix was obtained.

	M1	M2
Slag (ECOCEM, France) (g)	600.0	600.0
Water (g)	130.4	190.3
Sodium Silicate (g)	32.9	32.1
Sodium Hydroxide Solution 50 % w/w (g)	23.1	23.1
Aggregate (Bernasconi) (g)	4414	4414



Figure 4.2.1: Mix design and visual appearance of porous concrete at varying water to binder ratio. Left: Mix design for two water to binder ratios (0.25: M1 and 0.35: M2). Right: Visual appearance of tested samples. The first two digits (M1 or M2) represent the mix and the second two (S1, S2 and S3) indicate unique individuals. Bernasconi is a quartz aggregate (Quarzsand, 2 – 3.2mm, Carlo Bernasconi AG, Berne, Switzerland).

The molds were placed on a plywood sheet lined with a plastic mat. Batches were evenly distributed into 3 molds and compacted after being filled halfway. Molds were sandwiched between plastic mats and 2 sheets of plywood. 1 L of water was poured onto the plywood and an open receptacle of water was placed near the molds. All samples were then placed in a plastic bag and left to cure for 4 months.

Concrete cylinders were then removed from their curing enclosure and immediately placed in the testing apparatus (a wind tunnel like the one depicted in Figure 3.2.3 bottom right). Ducting fans (ERR 25/1, MAICO, Villingen-Schwenningen, Germany) were used to subject the samples to varying pressure drops. The average velocity of air passing through the samples was measured according to ASTM standard D3464 – 96 (2014) (standard test method for average velocity in a duct using a thermal anemometer) with a hot wire thermal anemometer (TSI/Alnor 9515, TH Industrie, La Garenne-Colombes, France). Drop in the pressure across the slab was measured using two digital pressure sensors (BME680, Bosch Sensortec, Reutlingen, Germany) with an absolute accuracy of 60 Pa. The sensors were placed less than 5 cm away from the centerline of the slab inside the ducting which was connecting the fans to the sample. The ducting was made using wax-coated cardboard cylinders (6-inch diameter forms for concrete pours, Bomix, Gildeweg, Germany). Permeability coefficients were derived in accordance with Ansys's user guide version 12.0 (Ansys, Pennsylvania, United States) with air properties at 15 °C and 101.33 kPa having density equal to 1.225 kg m⁻³ and viscosity equal to 1.789 * 10⁻⁵ kg m⁻¹ s⁻¹ (Çengel and Boles, 2001). The porosity and bulk density of samples were measured according to Section 3.2.3.

4.3. Results

The viscous inertial resistance factor of 6 porous concrete samples (cylinders 52 mm thick having diameters of 152 mm) were determined using air (Figure 4.3.2 and Table 4.3.1) as described in Section 3.3.3. The 3 samples from the first mix (M1) had a water to binder ratio of 0.25 and the other 3 (M2) had a water to binder ratio of 0.35. The resulting porosity and bulk density of the two mix designs investigated are depicted in Table 4.3.1.

Table 4.3.1: Properties of porous concrete samples with two different water to binder ratios.

Sample	M1S1	M1S2	M1S3	M2S1	M2S2	M2S3
Porosity	0.39	0.39	0.38	0.27	0.36	0.32
Bulk density (kg m ⁻³)	1763	1810	1606	1654	1624	1705
Viscous inertial resistance factor (α^{-1}) (m ⁻²)	729E6	664E6	908E6	198E6	329E6	89E6
Inertial resistance (C ₂) (m ⁻¹)	3.5E4	2.9E4	1.9E4	5.8E4	4.7E4	5.3E4
w/b	0.25	0.25	0.25	0.35	0.35	0.35

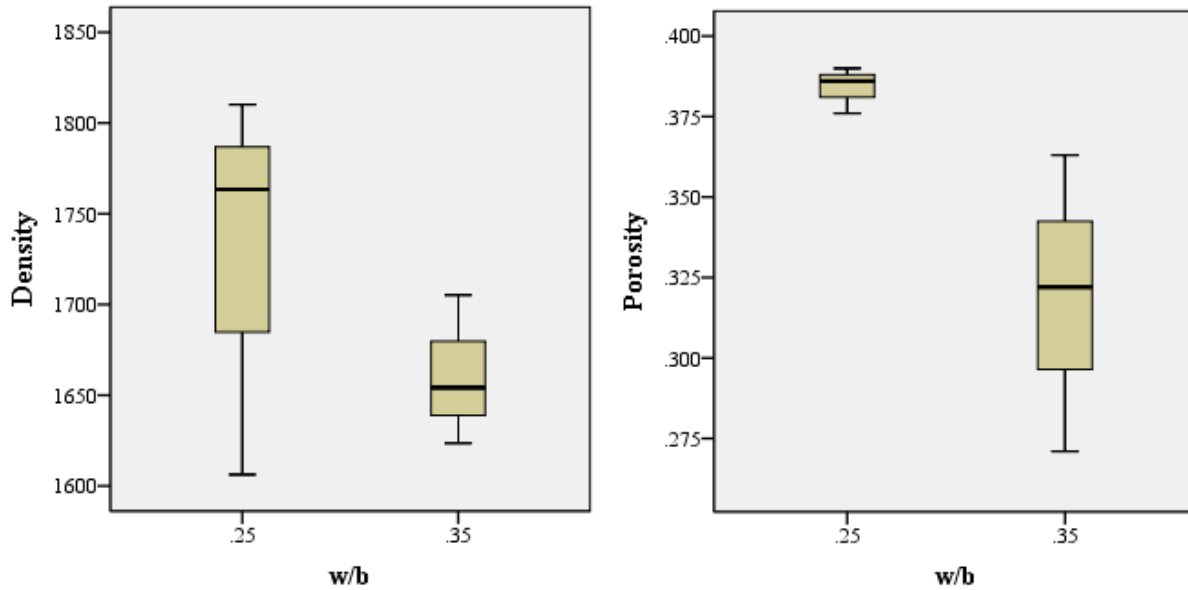


Figure 4.3.1: Porosity and bulk density of porous concretes made using two different water to binder ratios. The density is denoted as kg m⁻³.

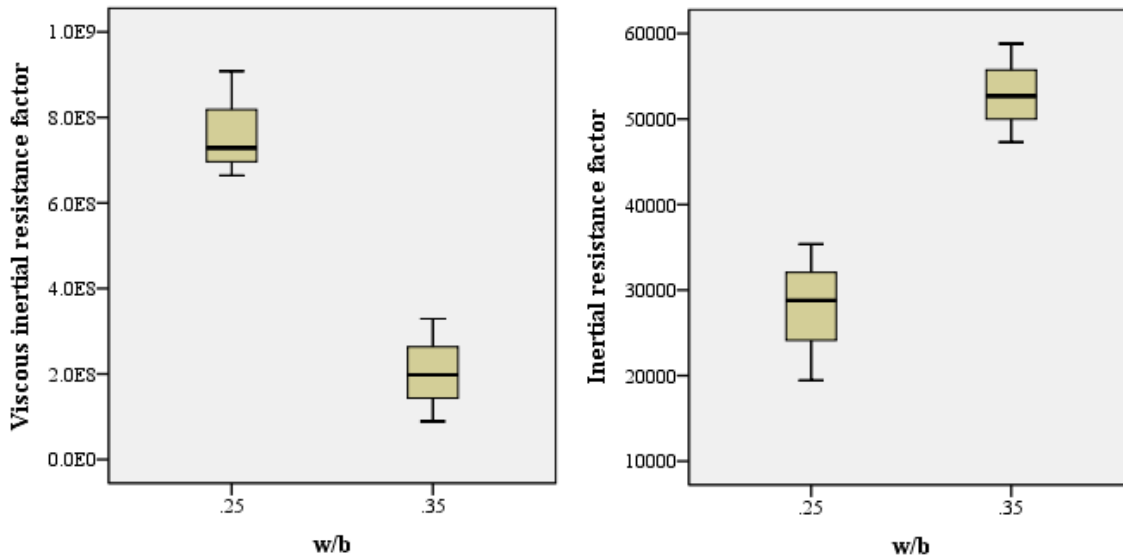
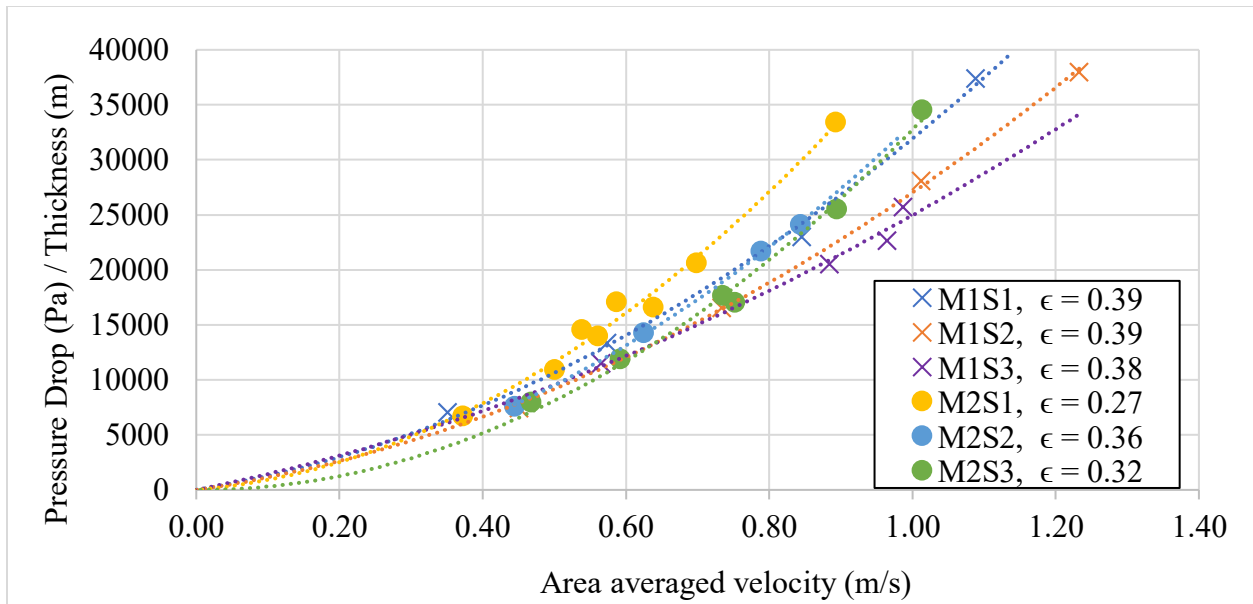


Figure 4.3.2: The effect of water to binder (w/b) ratio on the permeability of alkali activated porous concrete. The numbers beside the sample labels in the top graph are their respective porosity. Mixes M1 and M2 have w/b ratios of 0.25 and 0.35 respectively. The units for the viscous inertial resistance factor and the inertial resistance factor are m^{-2} and m^{-1} respectively.

4.4. Discussion

To assess the statistical significance of the results, ANOVAs for each dependent variable (porosity, density, resistance factors) was conducted according to water to binder ratios (groups). The tests statistics (p value) being significant at the 0.072, 0.246, 0.012, 0.005 for porosity, density, inertial resistance and viscous inertial resistance respectively (results can be found in Table A.2). Data was normally distributed and had homogeneity of variance. All variables were found to be

normally distributed across groups using Shapiro-Wilk's test of normality (Table A.3). A Levene's test as described by Olkin (1960) was used to verify the equality of variances for the data (dependent variables) obtained from the samples (all had a p value greater than .05: 0.139, 0.323, 0.602 and 0.823 for porosity, density, inertial resistance and viscous inertial resistance respectively). The effect sizes as determined by the value of ω^2 (Tomczak and Tomczak, 2014) are large (0.54, 0.79, and 0.86 for porosity, inertial resistance factor and the viscous inertial resistance factor). The change in water to binder ratio accounted for approximately 86 % of the variance in the viscous inertial resistance factor.

Increasing the water to binder ratio from 0.25 to 0.35 significantly (Table A.2) increased the air permeability for the studied mix design (3.2 mm aggregate at ~ 35 % porosity). Increasing the water to binder ratio from 0.25 to 0.35 increased the mean (Table A.1) inertial resistance factor from $2.8 * 10^4$ to $5.3 * 10^4 \text{ m}^{-1}$ while decreasing the mean viscous inertial resistance from $7.67 * 10^8$ to $2.05 * 10^8 \text{ m}^{-2}$. The values of permeability obtained fall within the range reported by others (Neithalath et al., 2010). From the visual inspection of the top graph (4.3.1) the second mix (having w/b ratio equal to 0.25) was determined to be more permeable as the measured velocities result in lower pressure drops for flows of $\sim 1 \text{ m s}^{-1}$. However, the viscous inertial resistance (the inverse of permeability) scales with velocity while the inertial resistance scales with the square of velocity. Supplementary data points at lower velocities should be considered if a more precise value is to be obtained. When comparing values with the ones of Chapter 3, viscous inertial resistances are two orders of magnitude higher for the 152 mm cylinders versus the 500 mm square slabs.

Both mixes did not differ significantly in porosity nor density (Figure 4.3.1). M1 had ~ 7 % higher mean porosity than M2. M1 had a mean porosity of 38 % which is close to the porosity of compressed, irregularly packed spheres (Song et al., 2008). A possible cause of this variation might be the differences in compaction or the material distribution during the mixing process and should be investigated further.

More clumping was observed in mixes with a w/b ratio of 0.25. After pouring concrete with a w/b ratio of 0.25 a larger portion of material remained. After pouring with a w/b ratio of 0.35 no material remained in the mixing bucket, and all fitted in the molds. Samples with a w/b ratio of 0.25 had a lower integrity, with many aggregates breaking apart after being manipulated. Future studies should include a quantitative assessment of strength and abrasion resistance for a more complete description of the physical material properties.

The decrease in the viscous inertial resistance factor at higher water to binder ratios despite an increase in the inertial resistance factor should be further investigated as it is at odds with the power law scaling relationship between viscous and inertial permeability in geologic porous media (Zhou et al., 2019). However, other artificial porous media such as metal foams can exhibit this behavior (Boomsma and Poulikakos, 2001).

4.5. Conclusion

This chapter provided insights on the effect of changing water to binder ratios on the physical material properties of a bio-receptive concrete mix. Increasing the water to binder ratio increased the permeability of alkali activated porous concretes. For the two mix designs considered, increasing water to binder ratio did not significantly affect bulk density and porosity. A recommendation is to employ mix designs having a water to binder ratio of 0.35 at ~ 30 - 35 % porosity for bio-receptive concrete (Hitti, 2018). For the mixes investigated in this study, increasing the w/b ratio from 0.25 to 0.35 decreased its inertial resistance by a factor of 2.

Connecting Statement for Chapter 5

Chapter 3 devised a procedure to determine the permeability of porous concretes using air. This technique was then employed in Chapter 4 to measure the effect of varying water to binder ratios. Chapter 5 expands on the experimental setup by incorporating air properties to study the dehydration of water from porous concrete samples. The purpose of this study is to gain insight on how this material could be used in heating and ventilating and to explore the hydration of alkali activated materials. The experiments in Chapter 5 characterize the drying mechanisms in alkali activated porous concrete mixes. Chapter 5 also determines the extent to which hydration water is bound in the alkali activated blast furnace slag.

5. Flow Through Air-Drying of Porous Concretes

5.0. Abstract

Water desorption from bio-receptive (Hitti, 2018) porous concrete cylinders (152 mm diameter by 50 mm thick) subjected to flow-through air drying is qualitatively described by considering the change in the temperature, relative humidity and pressure over time of the incoming and outgoing air stream. By immediately subjecting samples which have been curing sealed for 4 months to flow-through drying, it was determined that water in the amount of 50 % or more than the mass used in the chemical hydration of the cementitious binder remained. The largest value observed was 94 %. The difference in the concentration of the alkali used in hydration was determined as a possible cause for this discrepancy. Furthermore, the flow-through drying of concrete samples immersed in water for 15 minutes, one hour and one day, provides insight on the rate at which water infiltrates into the meso and micro porosity of the alkali activated material. For the sample studied, it took approximately the same duration (400 seconds) for water evaporation to be limited by diffusion from the binder after submersion times of 1 hour and 24 hours. Overall, the longer the submersion time, the longer it took for flow-through drying to completely remove the water from the porous concrete.

5.1. Introduction

Many drying methods such as vacuum assisted, freeze, saturated salt modified atmosphere and solvent exchange have been investigated as they relate to the resulting microstructure of cement pastes. For concrete, most drying studies are performed on solid samples using superheated steam or oven drying (Šelih et al., 1996; Vinkler and Vitek, 2016). Air drying of OPCs effects the density of only the first few mm exposed after months (Malab et al., 2009). With regards to the drying of porous concrete little literature is available (Rasiah et al., 2013).

The flow of liquids in unsaturated porous concrete occurs both at the macroscopic (mm) (Figure 1.1.1) and microscopic (μm) (Figure 5.1.1) scale. The mechanistic outline of this process is described in Section 1.7. The flow of a gas through a porous medium partially occupied by a liquid phase causes evaporation. This occurs even if the inlet gas is fully saturated due to volume expansion. This process is referred to as flow-through drying (Mahadevan et al., 2006). To date, no literature has explored the flow through drying of alkali activated porous concretes.

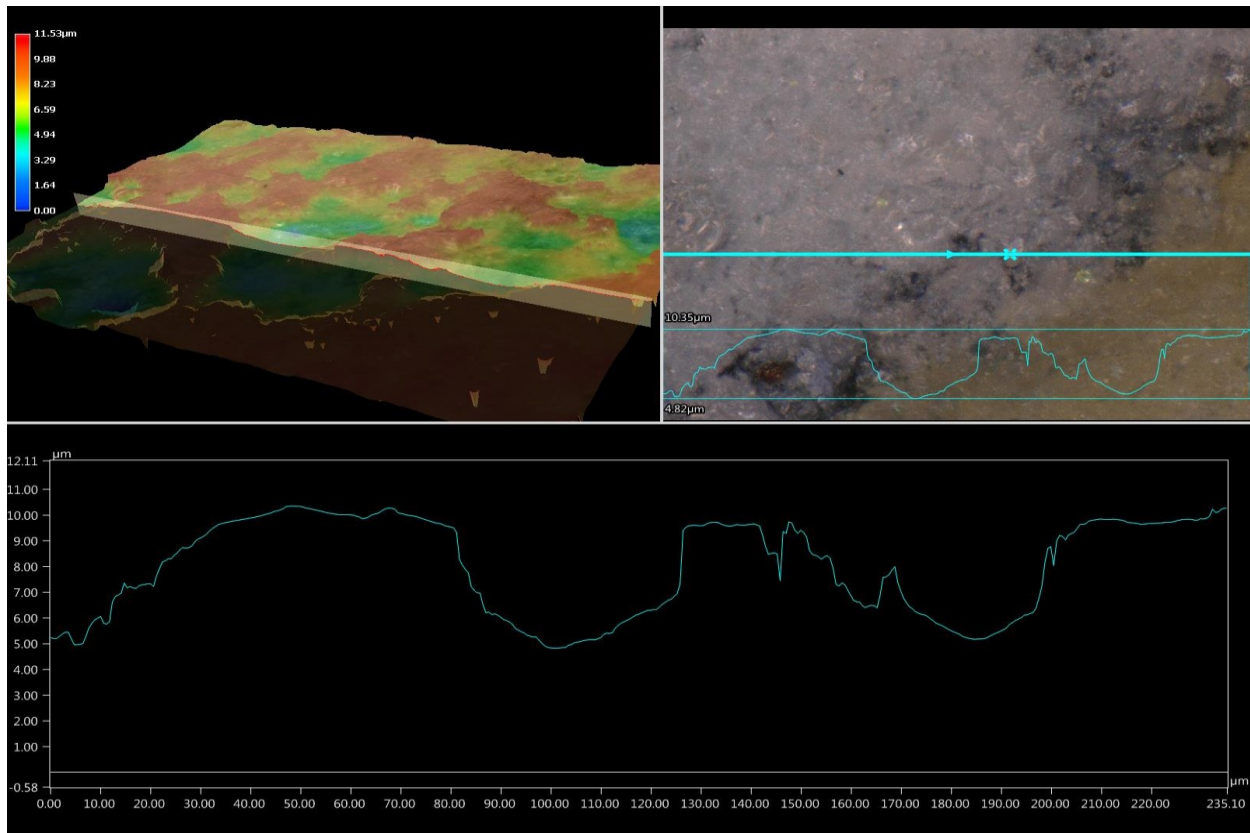


Figure 5.1.1: Microstructural profile of interfacial transition zone (quartz – alkali activated slag). The white in the top right image corresponds to alkali activated slag (ECOCEM, France) and brown to quartz (Quarzsand, 2 – 3.2mm, Carlo Bernasconi AG, Berne, Switzerland). The sample was cut with a circular saw (Minitom, Struers, Ballerup, Denmark) equipped with a high quality cut off wheel M0D13 (Struers, Ballerup, Denmark). Image was taken and processed with a digital 3D microscope (VH-ZST, Keyence, Osaka, Japan).

5.2. Materials and Methods

BME680 sensors (Bosch Sensortec, Reutlingen, Germany) are connected to a computer (Raspberry pi 3 Model B, Raspberry Pi Foundation, Cambridge, United Kingdom) and interfaced using the I2C (NXP Semiconductors, Eindhoven, Netherlands) digital communication protocol. The signals from the sensors were multiplexed using a TCA9548A low-voltage 8-channel I2C switch with reset (Texas Instruments, Dallas, Texas, United States) which enabled the use of multiple of the same sensor on the same communication bus. The conductive wire used to connect the various components had 4 cores at 22 gauge and was shielded (Belden, Missouri, United States). All voltage common collector pins of the sensors and the multiplexer were connected in parallel to the computer's 3.3-volt power output. All direct current grounds were connected in parallel with the ground pin of the computer. Serial Clock (SCL) and Serial Data (SDA) of sensors

are connected to separate channels of the multiplexer. SCL and SDA pins of the multiplexer are connected to the computer's SCL and SDA pins. A software was written in Python (Python, 3.6, Python Software Foundation, Wilmington, Delaware) to sequentially address sensors via the multiplexer and stored the retrieved information. The sensors' temperature output was calibrated according to ASTM E2877 – 12^{el} (2012) (Standard Guide for Digital Contact Thermometers). A two point calibration as described by (Mahmoudi et al., 2014) was performed on the values obtained for relative humidity. Sensors were subjected to two reference humidity values (32.8 ± 0.2 % at 25 °C and 84.2 ± 0.3 % at 25 °C using saturated salts solutions of MgCl₂ (magnesium chloride, pure, ACROS Organics, Geel, Belgium) and KCl (potassium chloride (Crystalline/Certified ACS), Fisher Chemical, New Hampshire, United States) respectively, maintained according to ASTM E104 – 02 (2012) (standard practice for maintaining constant relative humidity by means of aqueous solutions).

The sensors were used to monitor the change in air properties (pressure, temperature and relative humidity) as it flowed through porous concrete samples studied in Chapter 4. The samples were subjected to flow through drying immediately after being removed from their sealed molds (after 4 months of sealed curing) and after being submerged in water for 15 minutes, 12 hours and 24 hours. The flow of ambient air was driven by a 147 W ducting fan (ERR 25/1, MAICO, Villingen-Schwenningen, Germany) and averaged $\sim 0.6 \text{ m s}^{-1}$. An air flow was maintained until no perceivable increase in relative humidity between the inlet and outlet was being observed. The experimental setup was like the one depicted in Figure 3.2.3 (bottom right). Both sensors were located at the center of the ducting (diameter forms for concrete pours, 6-inch, Bomix, Gildeweg, Germany) connecting the fan to the porous concrete cylinder 50 mm by 152 mm (diameter) being dehydrated. Sensors were located 5 cm away from their respective interface (inlet and outlet). Temperature and humidity differences were calculated as outlet value minus inlet value, where outlet and inlet represent the property of the air before flowing through the slab and after flowing through respectively. A pressure greater than the atmospheric pressure is maintained at the inlet using the ducting fan. The approximate temperature and relative humidity of the inlet air was 22 °C and 25 % respectively.

5.3. Results

The change in masses for samples M2S2, M2S3 and M1S3 (Figure 4.2.1) was recorded (Table 5.3.1) after being subjected to flow through drying. Samples were exposed to an airflow immediately after being removed from curing (Section 4.2).

Table 5.3.1: Water remaining in alkali activated porous concrete samples after being sealed cured for 4 months. Samples starting with M1 had a w/b of 0.25 and samples starting with M2 had a w/b of 0.35.

Sample label	M1S3	M2S2	M2S3
Water removed by flow through drying (g)	47	36	43
Approximate amount of water used in casting sample (g)	50	70	70
Percent of water retained after 4 months of being cured (%)	94	51	61

The following graphs (Figures 5.3.1 - 5.3.4) describe the change in air properties at constant pressure drops through the same sample M2S2 (Figure 4.2.1) submerged for varying amounts of time under 10 cm of water.

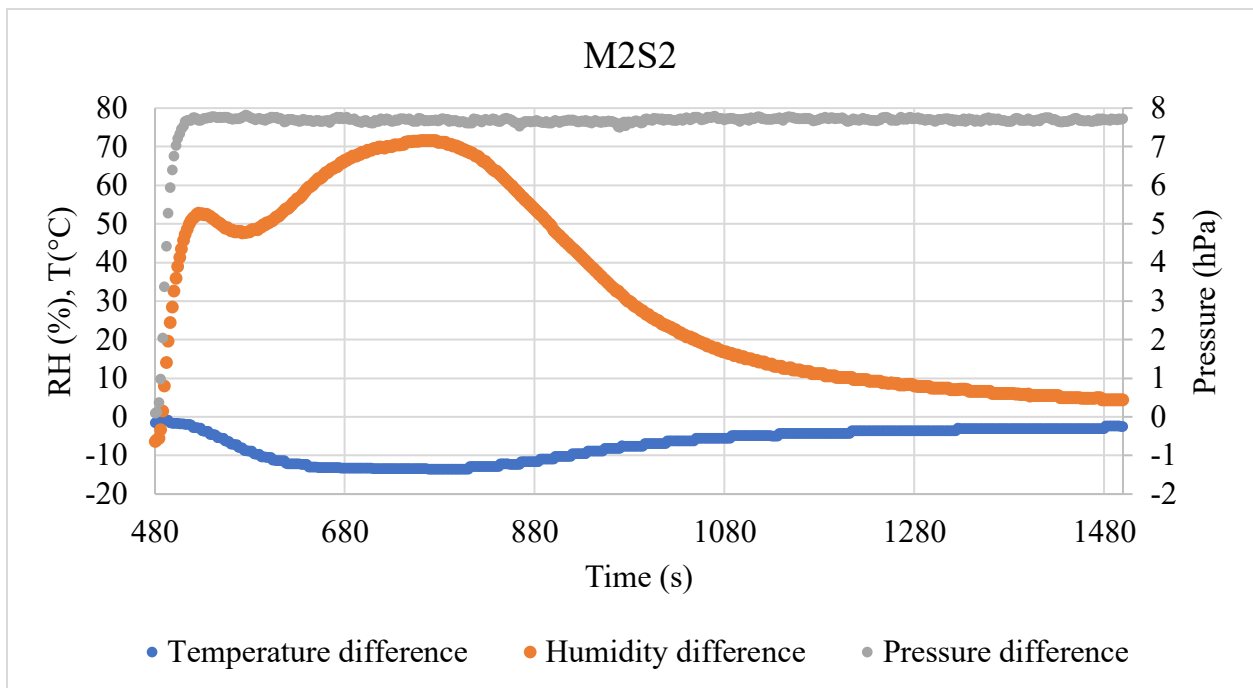


Figure 5.3.1: Removal of hydration water from alkali activated porous concrete (sample M2S2) after 4 months of sealed curing. X axis starts at 480 seconds and represents when the fan driving the airflow was switched on.

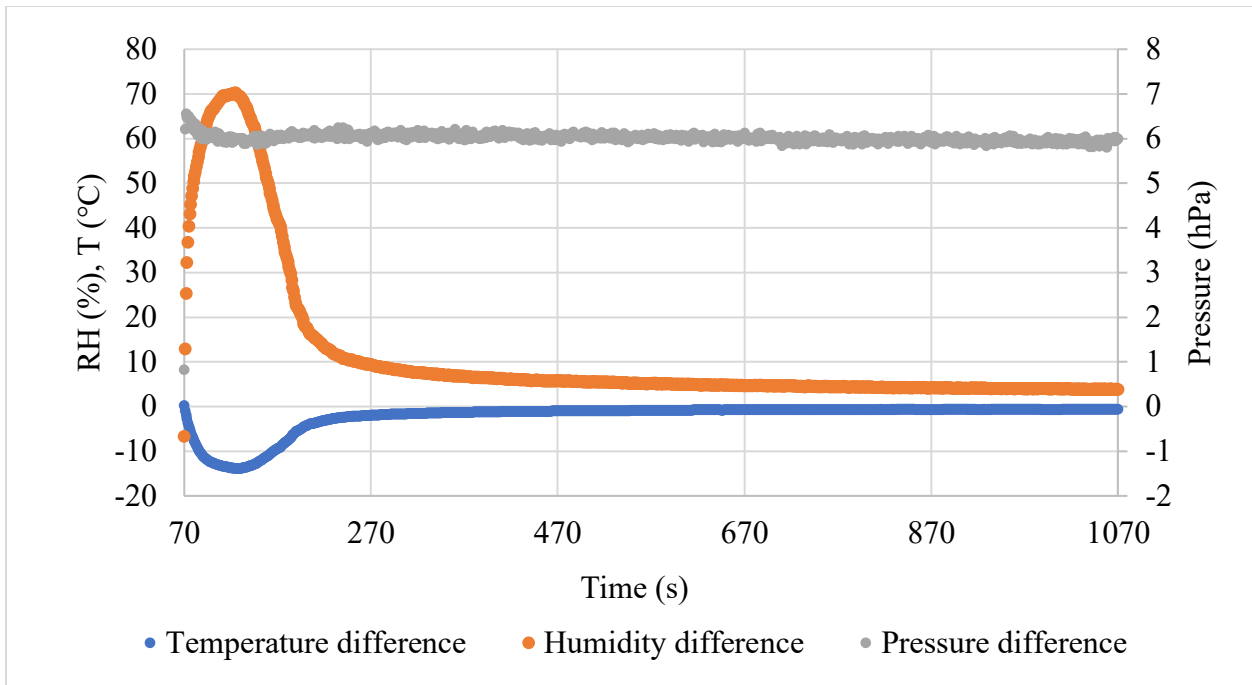


Figure 5.3.2: Removal of water retained in porous concrete sample (M2S2) after being submersed in water for 15 minutes. X axis starts at 70 seconds and represents the time when the fan driving the airflow was switched on.

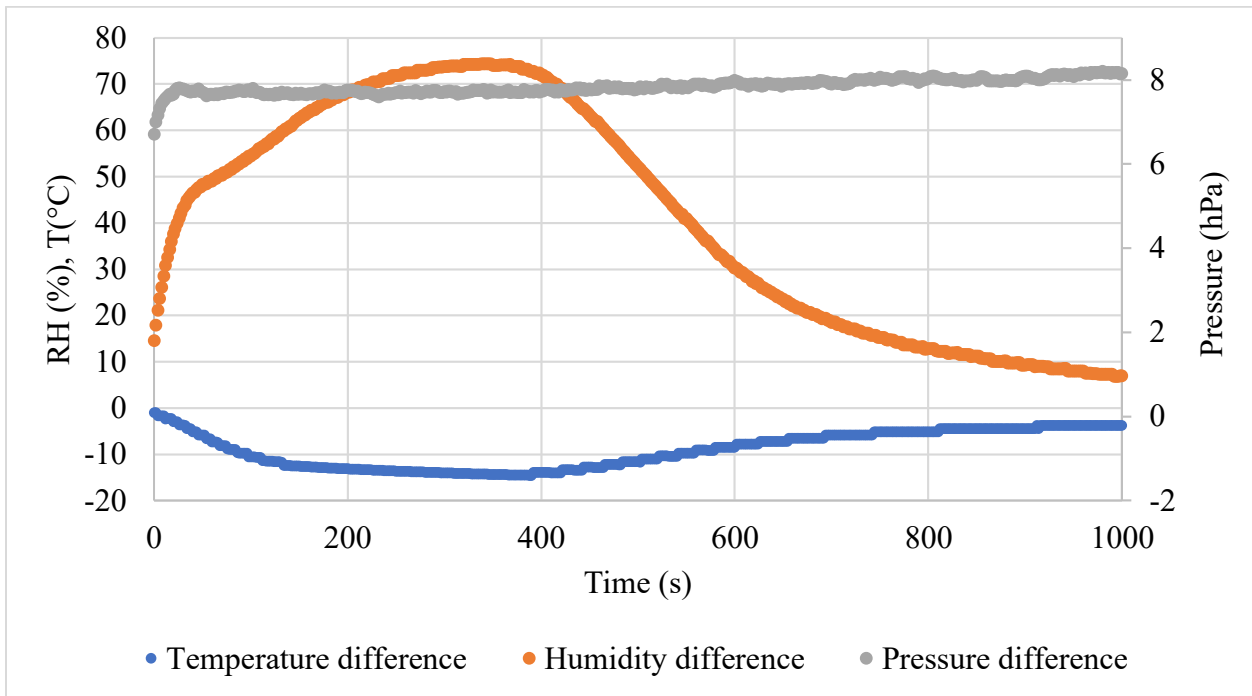


Figure 5.3.3: Removal of water retained in porous concrete sample (M2S2) after being submersed in water for 1 hour.

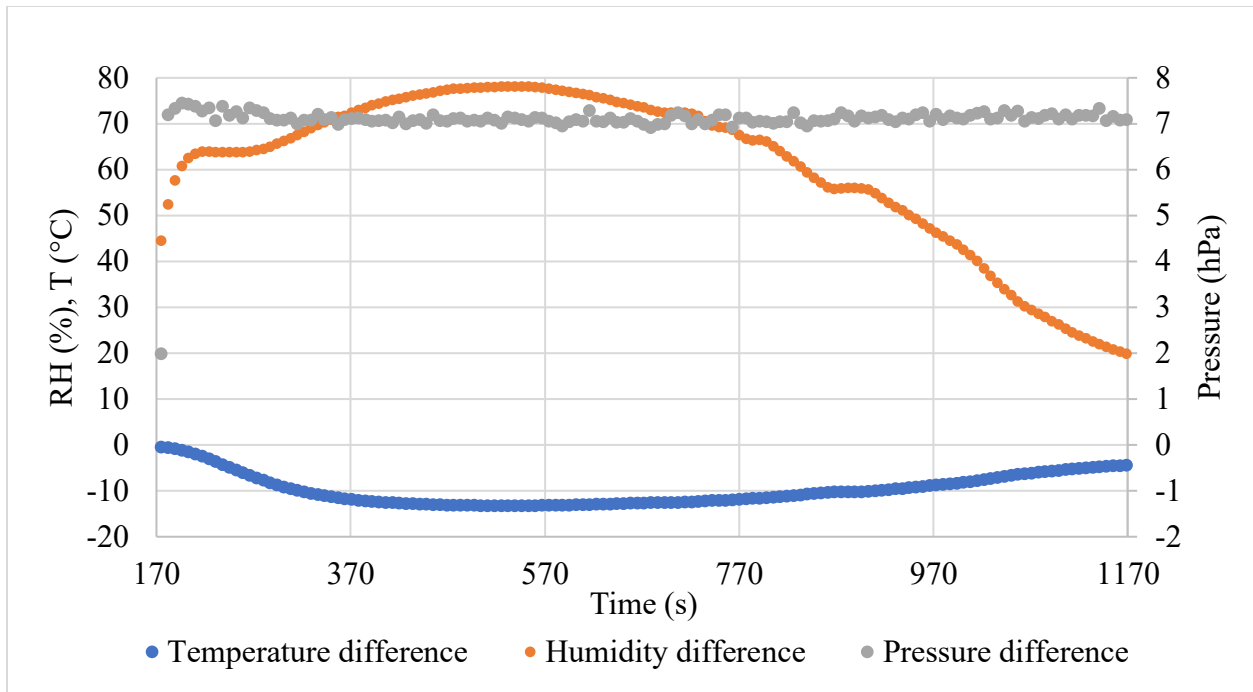


Figure 5.3.4: Removal of water retained in porous concrete sample (M2S2) after being submerged in water for 1 day. X axis starts at 170 seconds and coincides with the time at which the fan driving the airflow was switched on.

5.4. Discussion

An amount of water more than 90 % that of the water used in hydrating (water used in the mix design) sample M1S3 remained over the 4 months of curing, while more than 50 % remained for samples M2S2 and M2S3. Whether a fully hermetic seal was in place during curing was not assessed. Water might have come from outside the molds as condensate from the air. It cannot be determined that the water removed was indeed all in provenance of the mix design. Nevertheless, more water was retained for the sample having a lower w/b ratio.

From the preliminary results obtained (Figures 5.3.1 - 5.3.4), the presence of two key regimes of moisture release were observed: An initial rising rate of evaporation (initial phase), and a secondary (decaying phase) where water evaporation from the sample decreased. Notably, during the initial phase, the increasing rate of evaporation from the porous concrete likely occurred due to funicular water (Figure 1.7.1) being removed, subsequently leading to a slight increase in flow rate through the slab and more binder surface area being exposed from which evaporation occurred. A feature from this initial regime was the presence of an inflection (Figures 5.3.1, 5.3.3 and 5.3.4). The magnitude seemed to correspond with the amount of time the water was present within the porous concrete. With regards to Figure 5.3.1, two periods of decreasing relative

humidity difference of the air flowing are observed. Moreover, the decrease in air temperature lagged when compared to the slab which was only submerged for 15 minutes (5.3.2).

The secondary phase is a period in which larger connected pores no longer contained water, and the evaporation rate from the porous concrete became increasingly driven by diffusion from the binder. The physical orientation of the drying samples (circular cross-section placed parallel to the force of gravity) warrants reconsideration. The effect of gravity caused an uneven drying front to migrate from the top to the bottom of the cylinder during the drying process. Overall, increasing the time of submersion corresponded with a longer drying period. The initial phase for 1-hour submersion and 24-hour submersion (Figure 5.3.3 and 5.3.4) ended at approximately the same time (400 seconds after the start of the airflow), however, the decaying phase of the 24-hour submersion is prolonged when compared to the 1-hour indicating that water was present deeper within the micropores or that the water in the smaller pores were bound to a greater degree at the time of drying. This might be a partial explanation for the success encountered in the pre-germination soaking of bio-receptive concretes as described by Hitti (2018). As bio-receptive porous concrete dries, plants roots growing within will experience drought stress. Soaking the cement for an extended period prior to seeding will reduce the onset of drought.

An unreproducible observation occurred during the permeability measurement of a larger sample (Chapter 3). A spontaneous water release from sample 6 (Table 3.2.2) was monitored (Figure 5.4.1). This occurred after being aspirated for approximately one hour. The slab was sitting in the curing chamber (Section 3.2.2) for more than 72 hours prior to being placed in front of wind tunnel. It was being aspirated for the first time. Temperature of the air flowing through unexpectedly dropped after 4000 seconds. By considering the mass flow rate and averaging the energy transferred to air yielded ~ 680 kJ. The amount of water used in casting this sample was 0.456 kg. Evaporative cooling of 0.456 kg of water (if heat of vaporization is about 2260 kJ kg^{-1}) was calculated to result in $- 1030$ kJ. It was estimated that ~ 0.3 kg of water was evaporated from this sample (approximately 66 % of the amount of water used for hydration).

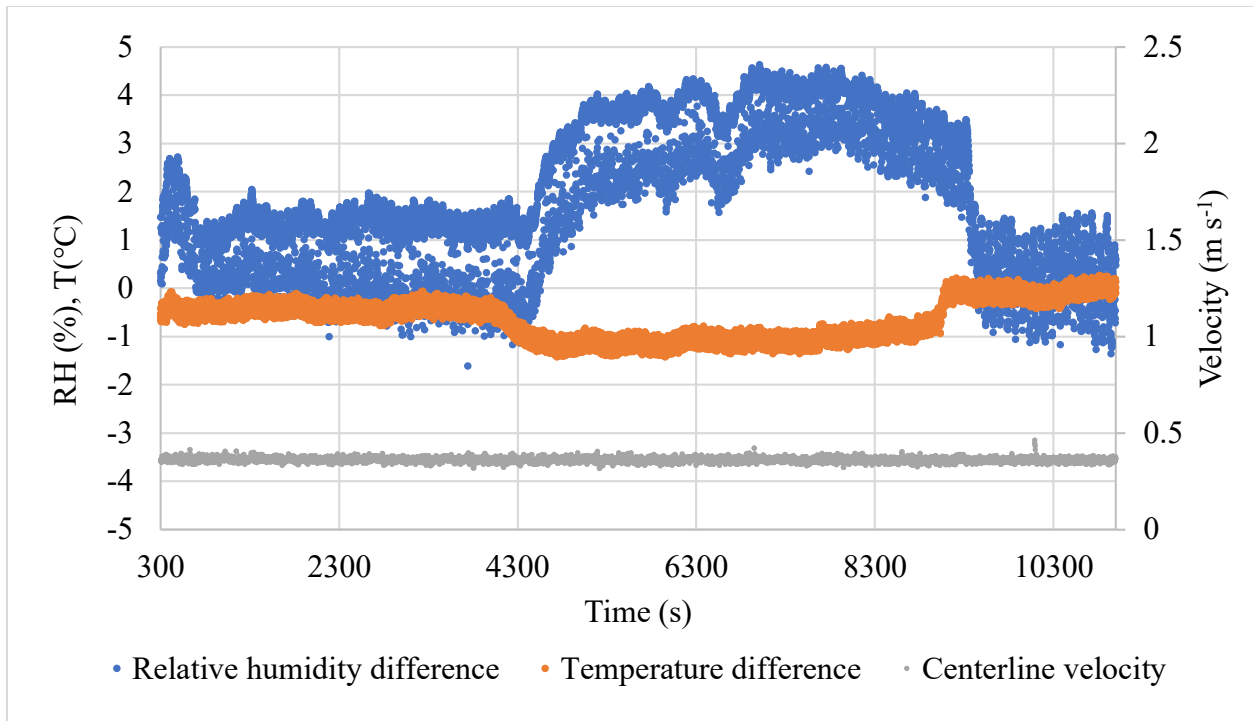


Figure 5.4.1: Evaporation of hydration water from an alkali activated porous concrete slab being aspirated.

Reasons as to why the water release occurred remains unknown. The device described in this chapter was in part designed to further recreate this observation. Replication of this event was not possible. Future testing should focus on lowering the pressure drop, varying curing conditions and testing samples which have not been curing for more than 28 days.

5.5. Conclusion

The amount of water remaining in a specific mix design of alkali activated slag developed for its enhanced plant bio-receptivity is quantified. It was determined that more than 50 % could remain if cured sealed. Flow through drying of samples provided an insight on why pre-germination soaking might be beneficial by demonstrating that water continues to infiltrate into the binder even after being submerged for 1 hour. Further standardization of this test and more replicates will be considered to determine whether this experimental setup can yield information on chemical hydration mechanisms and properties of hydraulic binders. For the bio-receptive porous concrete mix design investigated it took ~ 400 seconds for water evaporation to be limited by diffusion from the binder when subjected to flow through drying (at a pressure drop of 8 hPa with air at 25 % relative humidity and a temperature of 22 °C) after being submersed in water for 1 hour or more.

Connecting Statement for Chapter 6

Previous chapters were concerned with modelling and quantifying the physical material properties of alkali activated porous concretes. The main focus of the research was to quantify the airflow through porous concrete material with the objective of facilitating engineering design optimization. Chapter 6 introduces functionalization of porous concrete with two proof-of-concepts: One for heating and the other for cooling air.

6: Prototypes of Porous Concretes for Heating and Ventilation

6.0. Abstract

The change in temperature of an airflows through porous concrete slabs (having dimensions of 0.5 m by 0.5 m by 0.05 m) subjected to controlled conditions are considered. One scenario in which the temperature of the slab is higher than the air temperature, and another; in which a predetermined volume of water is introduced uniformly onto one of the slab's interface. For respective scenarios, the air temperatures where plotted over time to qualitatively assess the extent to which porous concrete can be used to heat and cool air.

The heat capacity of bio-receptive porous concrete (Hitti, 2018), was measured using the mix design's properties: The specific heat capacity of quartz and alkali activated slag. It was estimated to be $1384 \text{ kJ m}^{-3} \text{ }^{\circ}\text{C}^{-1}$. This value is corroborated by the energy balance when applied to the air flowing through a slab heated to $50 \text{ }^{\circ}\text{C}$.

6.1. Introduction

The thermal behavior of concrete has been investigated as a potential material for energy storage (Adeyanju, 2015). Adesina (2019) used phase change materials in concrete for releasing energy based on the temperature of the environment. The functionalization of concrete with additional components causes concern due to lack of long-term data on their effect regarding concrete durability. With proper design, such materials can provide tangible benefits without a significant reduction in the material's strength. Porous concretes can have varying thermal properties (at different mix proportions) without altering the underlying chemical composition of the cement from which it is made.

The use of porous materials can be employed to enhance forced convection heat transfer due to their extensive contact surface (solid-fluid interface). However, studies on the heat transfer in porous concrete have mainly focused on its use in pavements for reducing their heating effect. Heat islands are the result of cities replacing the natural land cover with pavement, buildings, and other infrastructure. These changes contribute to higher urban temperatures in several ways (Sabnis, 2016). While observing the behavior of porous concrete pavements it was noted that when exposed to direct sunlight they absorbed a greater amount of heat than traditional concretes (Kevern et al., 2009). The thermal properties of porous concrete such as albedo, thermal

conductivity, specific heat capacity, emissivity, and coefficient of thermal storage differ from those of traditional concretes. When used as pavements, their total smaller output heat flux can diminish the heat island effect (Liqun et al., 2017).

Two use cases of functional porous concrete were developed. The following examples employed forced convection heat transfer through the bio-receptive mix designs reported in previous chapters for heating and cooling air. The amount of energy stored in a 0.5 m by 0.5 m by 0.05 m thick heated slab is quantified by being aspirated with cooler air. In another instance the evaporative cooling from a section of a concrete slab being aspirated is considered.

6.2. Materials and Methods

6.2.1. Heated Porous Concrete Slabs

0.5 m by 0.5 m by 5 cm thick alkali activated porous concrete slabs were used (same as Chapter 3). They were heated by being placed outside in broad daylight for 5 hours. Slabs were then aspirated using the device described in Figure 3.2.3 (top left). Temperature and relative humidity of inlet and outlet air were measured using an array of thermocouples and analogue humidity sensors (Figure 3.2.3). Samples 3, 5 and 6 were aspirated until the difference in between the inlet and outlet temperature reached a value less than the absolute accuracy of the thermocouples for one minute. Measurements were recorded every second. The back-center point temperature of the slab was measured by wedging a thermocouple in the pore structure. The experiment was conducted inside of a curing chamber (Ineltec model CM – 50 m³, fabrication number 055/2006, 6.5 KW, Barcelona Spain) to ensure constant inlet temperature and relative humidity.

6.2.2. Evaporative Cooling from Porous Concrete Slabs

Alkali activated concrete sample 3 (Figure 3.2.2) was aspirated (as described in Section 3.2.5) at a constant rate of 0.6 m s⁻¹. Water was sprayed evenly onto the top 6 cm of the slab using a plastic bottle with sprayer. The mass of the sprayer was measured before and after to determine the amount of water added. The air temperature was measured before flowing through the slab and after (inlet and outlet respectively) (Figure 3.2.3). The air temperature at the outlet was measured at 7 different locations using an array of thermocouples (Figure 3.2.3). The sample was aspirated until inlet and outlet temperature did not differ by more than 1 °C for 300 seconds.

6.3. Results

6.3.1. Heated Porous Concrete

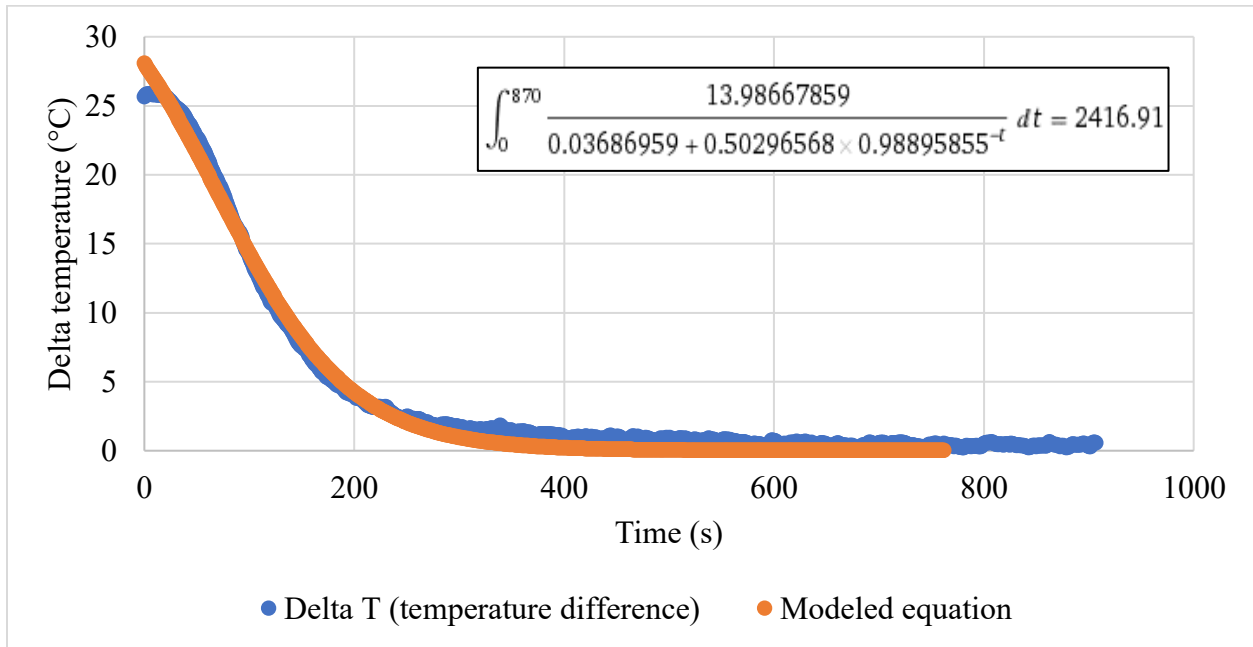


Figure 6.3.1: Temperature difference in between the outlet and inlet air flowing through a heated porous concrete slab. Centerline outlet temperature for the solar heated slab considered. Empirical data was fitted using *scipy's* (a Python (Python, 3.6, Python Software Foundation, Wilmington, Delaware) module) *optimize curve fit* method to obtain the modeled equation. The definite integral of the modeled equation was evaluated using *Wolframalpha* (Wolframalpha, Illinois, United States) from time 0 to 870. Data graphed for sample 6 of Chapter 3.

6.3.2. Evaporative Cooling from Porous Concrete Slab

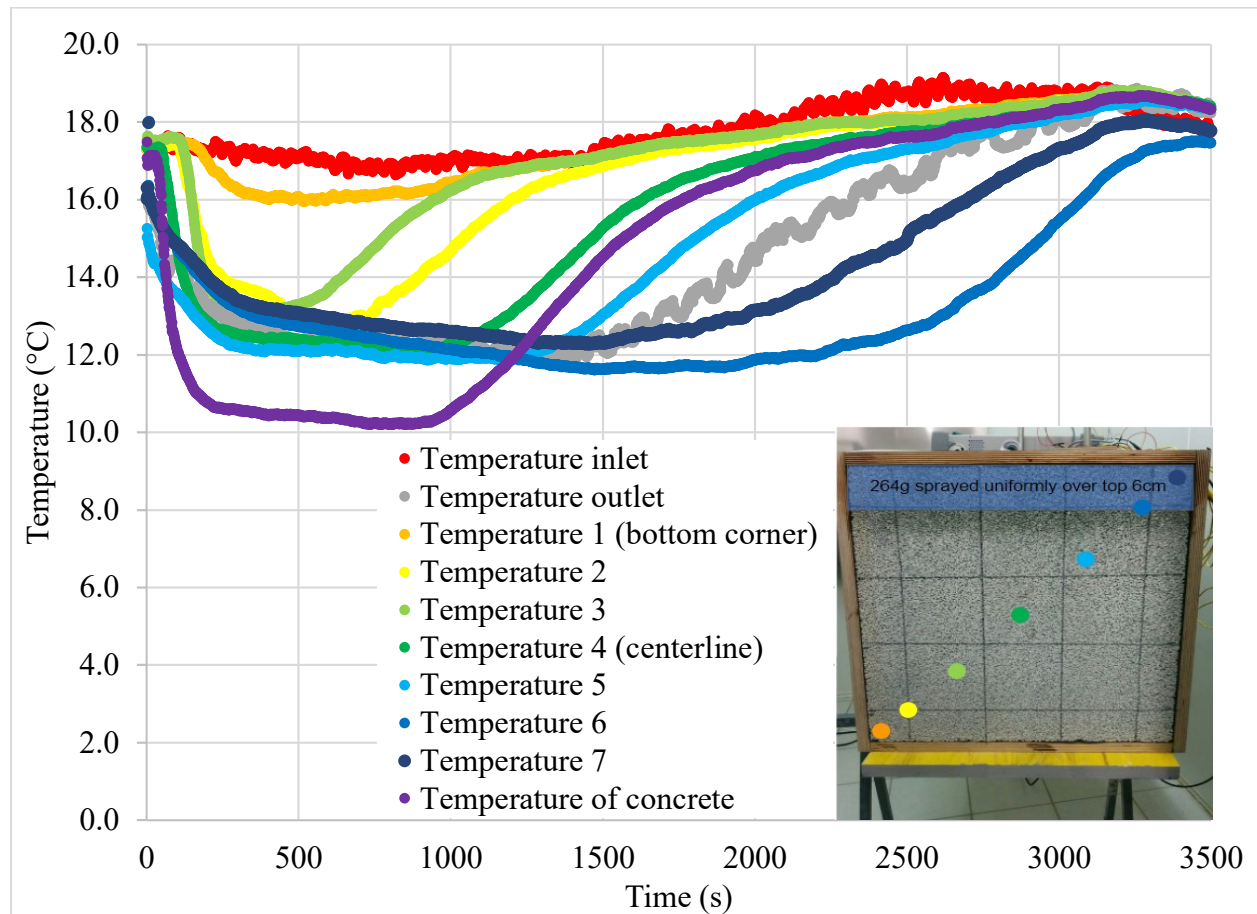


Figure 6.3.2: Evaporative cooling from a porous concrete slab after spraying top 6 cm uniformly with 264 g of water while being aspirated at $\sim 0.3 \text{ m s}^{-1}$. All temperatures are air temperatures measured using thermocouples connected to a data logger (Agilent data logger, 34970A, Keysight Technologies, Canada Inc., Mississauga, Ontario, Canada) located 5 cm away from the back (as seen in the small picture bottom right) surface. Color dots in the bottom right picture corresponds to the temperature profiles graphed.

6.4. Discussion

6.4.1. Heated Porous Concrete

The definite integral of the modeled function in equation (Figure 6.3.1) was evaluated for the period of interest. The period of interest was chosen to be the point at which the outlet temperature peaks. Multiplying the value of this definite integral with the average mass flow rate and the specific heat capacity of air resulted in $\sim 580 \text{ kJ}$ of energy transferred to the cooler air being aspirated through the sample. This value can also be calculated by considering the initial heat of the slab along with the specific heat capacities of quartz and alkali activated slag (Appendix

A.1). The mix design investigated had a volumetric heat capacity of $1384 \text{ kJ m}^{-3} \text{ }^{\circ}\text{C}^{-1}$. The two methods for calculating the energy transferred to the air flowing through the porous concrete resulted in similar values. The total energy transferred to air was approximately equal to the energy lost from the slab having values of 580 and 570 kJ respectively. Reasons for the discrepancy could have been an underestimation in the slab temperature, an overestimation of the average velocity flowing through the slab and an approximation error in fluid physical properties. When fan power consumption was discounted at 147 W (over 870 seconds), 452 kJ net was extracted from the slab as it cooled from $50 \text{ }^{\circ}\text{C}$ to $17 \text{ }^{\circ}\text{C}$.

Further studies could be conducted to determine other parameters such as convective heat transfer coefficients, thermal conductivity and heat capacity of the matrix. With a better calibrated device and an appropriate testing methodology, some of these values could be derived but is beyond the scope of this study. A conceptual attempt was focused at using a heat exchanging coil to maintain a constant slab temperature which would be of interest in some design situations (Figure 6.4.1). Technologies incorporating porous concretes should be considered in improving building heating efficiency.



Figure 6.4.1: Porous concrete heat exchanger concept. Left: The center of the slab halfway through casting. Right: Experimental setup for heat exchanging slab.

6.4.2. Evaporative Cooling from Porous Concrete Slabs

Evaporative cooling from the top of slab decreased temperature of the whole sample. The variation in temperature profiles measured on the diagonal of the outlet (Figure 6.3.2) is a result of thermal conduction. The top half of the slab reached approximately the same temperature after being aspirated for 10 minutes. Smaller temperature fluctuations along with a longer decay period

for temperature differences measured behind the wet porous concrete was observed. The time dependent temperature profiles measured behind the visually dry zones appear to be s-shaped while the other two have linear regions near the end. The latter might be a result of the water evaporation front migrating deeper within the micro porosity of the binder as highlighted in Chapter 5.

6.5. Conclusion

Approximately 450 kJ was extracted from a 0.0125 m³ solar heated bio-receptive porous concrete slab to heat interior air. Alkali activated porous concrete as a surface coating substrate to buildings could partly counter the heat island effect in major cities. This could also improve the appearance of some buildings. Future experiments should be designed to further investigating the value of the addition of alkali activated porous concrete in heating and ventilation systems. Research methods using ideal experimental conditions could determine which air input parameters should be measured. Specific setups should be optimized that target specific air properties. This data will determine the ideal incorporation of alkali activated porous concrete into current building designs.

Final Conclusions and Summary

The hydraulic binder studied in Chapter 2 was used to cast various bio-receptive concrete slabs. In Chapter 3, the air permeability of the material is determined using a custom experimental setup. The material was used as a hydroponic root-zone substrate for which the effect on permeability was quantified after 40 days of cultivating turfgrass. Chapter 4 relates one of the most important concrete mix design proportions, the water to binder ratio, to the material's permeability. The discrepancy between the results obtained for the cylindrical and cuboid samples (Chapter 3 and Chapter 4 respectively) is addressed by considering the wall effect in packed columns. Chapter 5 deals with water evaporation from the material being subjected to flow-through drying. Chapter 6 builds upon the previous experiments by using the alkali activated porous concrete for heating and cooling air. This supports the possible use of porous concrete as a functional building material for heating and ventilation.

Future research should expand on the use of vegetation concrete in buildings. Experiments should determine the added effect of different plant growth on the properties of flow-through air. Determinants such as irrigation and lighting will help with the incorporation of this material in building systems. During its use for the growing of plants, porous concrete is exposed to various conditions which are not well characterized in the traditional cement and concrete literature. Plant root growth and different nutrient solutions might impact the strength of alkali activated porous concrete.

I envisage more energy efficient future cities where grey concrete is replaced by beautiful lush green vegetation covering most building facades.

References

- Adesina, A. 2019. Use of phase change materials in concrete: current challenges. *Renewable Energy and Environmental Sustainability* 4:9.
- Adeyanju, A. A. 2015. Effects of pressure and friction parameters on a concrete bed energy storage system. *Energy Technology & Policy* 2(1):1-9.
- Aïtcin, P. C. P. P. C. 2000. Cements of yesterday and today - concrete of tomorrow. *Cement and Concrete Research* 30(9):1349-1359.
- Al-Otaibi, S. 2008. Durability of concrete incorporating GGBS activated by water-glass. *Construction and Building Materials* 22(10):2059-2067.
- Amhalhel, G., and P. Furmański. 1997. Problems of modeling flow and heat transfer in porous media. *Journal of Power Technologies* 85:55-88.
- Andres-Valeri, V., L. Juli-Gandara, D. Jato-Espino, and J. Rodriguez-Hernandez. 2018. Characterization of the infiltration capacity of porous concrete pavements with low constant head permeability tests. *Water* 10(4):480.
- Arsham, D. H., and M. Lovric. 2011. Bartlett's test. *International Encyclopedia of Statistical Science* 2:20-23.
- Babae, M., and A. Castel. 2018. Water vapor sorption isotherms, pore structure, and moisture transport characteristics of alkali-activated and Portland cement-based binders. *Cement and Concrete Research* 113:99-120.
- Banfill, P. F. G. 2003. The rheology of fresh cement and concrete - A review. In *Proceedings of the 11th International Congress on the Chemistry of Cement (ICCC) Cement's Contribution to Development in the 21st Century*. Durban, South Africa.
- Bear, J., and J. M. Buchlin. 1991. *Modelling and Applications of Transport Phenomena in Porous Media*. Springer Netherlands, Dordrecht.

- Bergmann, R., P. J. M. S. Will, and J. Ludbrook. 2000. Different outcomes of the Wilcoxon-Mann-Whitney test from different statistics packages. *The American Statistician* 54(1):72-77.
- Berryman, J. G., and S. C. Blair. 1987. Kozeny–Carman relations and image processing methods for estimating Darcy’s constant. *Journal of Applied Physics* 62(6):2221-2228.
- Boomsma, K., and D. Poulidakos. 2001. The effects of compression and pore size variations on the liquid flow characteristics in metal Foams. *Journal of Fluids Engineering* 124(1):263-272.
- Brunauer, S., and L. E. Copeland. 1964. The Chemistry of Concrete. *Scientific American* 210(4):80-93.
- Burke, S. P., and W. B. Plummer. 1928. Gas Flow through Packed Columns. *Industrial & Engineering Chemistry* 20(11):1196-1200.
- Cancio Díaz, Y., S. Sánchez Berriel, U. Heierli, A. R. Favier, I. R. Sánchez Machado, K. L. Scrivener, J. F. Martirena Hernández, and G. Habert. 2017. Limestone calcined clay cement as a low-carbon solution to meet expanding cement demand in emerging economies. *Development Engineering* 2:82-91.
- Çengel, Y. A., and M. A. Boles. 2001. *Thermodynamics : an engineering approach*. Eighth edition. ed. McGraw-Hill Education, New York.
- Chang, J. J., W. Yeh, T. J. Chung, and R. Huang. 2016. Properties of pervious concrete made with electric arc furnace slag and alkali-activated slag cement. *Construction and Building Materials* 109:34-40.
- Chen, W., and H. J. H. Brouwers. 2007. The hydration of slag, part 1: Reaction models for alkali-activated slag. *Journal of Materials Science* 42(2):428-443.
- Chindaprasirt, P., and T. Cao. 2015. 5 - Setting, segregation and bleeding of alkali-activated cement, mortar and concrete binders. In *Handbook of Alkali-Activated Cements, Mortars and Concretes*, 113-131. F. Pacheco-Torgal, J. A. Labrincha, C. Leonelli, A. Palomo, and P. Chindaprasirt, eds. Oxford: Woodhead Publishing.

- Duxson, P., A. Fernández-Jiménez, J. L. Provis, G. C. Lukey, A. Palomo, and J. S. J. van Deventer. 2006. Geopolymer technology: The current state of the art. *Journal of Materials Science* 42(9):2917-2933.
- Ergun, S. 1952. Fluid flow through packed columns. *Chemical Engineering Progress* 48:89-94.
- Ferdos, F., and B. Dargahi. 2016. A study of turbulent flow in large-scale porous media at high Reynolds numbers. Part II: Flow physics. *Journal of Hydraulic Research* 54(6):678-691.
- Garcia-Lodeiro, I., A. Palomo, and A. Fernández-Jiménez. 2015. 2 - An overview of the chemistry of alkali-activated cement-based binders. In *Handbook of Alkali-Activated Cements, Mortars and Concretes*, 19-47. F. Pacheco-Torgal, J. A. Labrincha, C. Leonelli, A. Palomo, and P. Chindaprasirt, eds. Oxford: Woodhead Publishing.
- Griffiths, R. F., and I. D. Roberts. 1999. Droplet evaporation from porous surfaces; model validation from field and wind tunnel experiments for sand and concrete. *Atmospheric Environment* 33(21):3531-3549.
- Hall, C., and W. D. Hoff. 2012. *Water transport in brick, stone, and concrete*. CRC Press, London.
- Hasan, K., and B. N. C. Hanifi. 1995. Pozzolan and cements with Pozzolan. *Pamukkale University Journal of Engineering Sciences* 1(2):121-127.
- Hemingway, B. S. 1987. Quartz; heat capacities from 340 to 1000 K and revised values for the thermodynamic properties. *American Mineralogist* 72(3-4):273-279.
- Hewlett, P. 2004. *Lea's chemistry of cement and concrete*. Elsevier, Burlington.
- Hitti, Y. 2018. Bio-receptive ground granulated blast-furnace slag porous concrete substrate,
- Hoagland, D. R. 1948. *Lectures on the inorganic nutrition of plants*. Chronica Botanica Company, Waltham, Massachusetts.
- Howe, W. L., and C. J. Hudson. 1927. Studies in porosity and permeability characteristics of porous bodies. *Journal of the American Ceramic Society* 10(6):443-448.

- Huang, C. L. D. 1979. Multi-phase moisture transfer in porous media subjected to temperature gradient. *International Journal of Heat and Mass Transfer* 22(9):1295-1307.
- Huang, J., C. Valeo, J. He, and A. Chu. 2016. The Influence of Design Parameters on Stormwater Pollutant Removal in Permeable Pavements. *Water, Air, & Soil Pollution* 227(9):311.
- Hubler, M. H., J. J. Thomas, and H. M. Jennings. 2011. Influence of nucleation seeding on the hydration kinetics and compressive strength of alkali activated slag paste. *Cement and Concrete Research* 41(8):842-846.
- Hughes, S. 2005. Archimedes revisited: A faster, better, cheaper method of accurately measuring the volume of small objects. *Physics Education* 40.
- Innocentini, M. D. M., V. R. Salvini, V. C. Pandolfelli, and J. R. Coury. 2004. Assessment of Forchheimer's equation to predict the permeability of ceramic foam. *Journal of the American Ceramic Society* 82(7):1945-1948.
- Innocentini, M. D. M., P. Sepulveda, V. R. Salvini, V. C. Pandolfelli, and J. R. Coury. 2005. Permeability and structure of cellular ceramics: A comparison between two preparation Techniques. *Journal of the American Ceramic Society* 81(12):3349-3352.
- Institute, A. C. 2005. *Specifications for Structural Concrete, ACI 301-05, with Selected ACI References: Field Reference Manual*. American Concrete Institute.
- Jansson, H., D. Bernin, and K. Ramser. 2015. Silicate species of water glass and insights for alkali-activated green cement. *AIP Advances* 5(6).
- Jiao, Z., Y. Wang, W. Zheng, and W. Huang. 2018. Effect of dosage of alkaline activator on the properties of alkali-activated slag pastes. *Advances in Materials Science and Engineering* 2018:12.
- Johansson, C. H., G. Persson, and D. o. B. R. National Research Council of Canada. 1958. Moisture absorption curves for building materials. National Research Council Canada.
- Jorge de, B., K. Rawaz, and S. Pedro Raposeiro da. 2018. Can we truly predict the compressive strength of concrete without knowing the properties of aggregates? *Applied Sciences* 8(7).

- Juenger, M. C. G., F. Winnefeld, J. L. Provis, and J. H. Ideker. 2011. Advances in alternative cementitious binders. *Cement and Concrete Research* 41(12):1232-1243.
- Keey, R. B. 1972. Chapter 7 - Drying under constant external conditions. In *Drying principles and practice*, 178-203. R. B. Keey, ed: Pergamon.
- Kevern, J. T., V. R. Schaefer, and K. Wang. 2009. Temperature behavior of pervious concrete systems. *Transportation Research Record* 2098(1):94-101.
- Khale, D., and R. Chaudhary. 2007. Mechanism of geopolymerization and factors influencing its development: a review. *Journal of Materials Science* 42(3):729-746.
- Khudhair, M., B. El Hilal, and A. Elharfi. 2018. Review on chemical (organic) admixtures in the cementitious materials. *Journal of Material and Environmental Sciences* 9(6):1722-1734.
- Kia, A., H. S. Wong, and C. R. Cheeseman. 2017. Clogging in permeable concrete: A review. *Journal of Environmental Management* 193:221-233.
- Kia, A., H. S. Wong, and C. R. Cheeseman. 2018. Defining clogging potential for permeable concrete. *Journal of environmental management* 220:44-53.
- Kim, H.-H., and C.-G. Park. 2016. Performance evaluation and field application of porous vegetation concrete made with by-product materials for ecological restoration projects. *Sustainability* 8(4):294.
- Kovac, M., and A. Sicakova. 2017. Changes of strength characteristics of pervious concrete due to variations in water to cement ratio. *IOP Conference Series: Earth and Environmental Science* 92:012029.
- Kowalski, S. J. 2007. *Drying of porous materials*. Springer, Dordrecht.
- Lee, K.-H., and K.-H. Yang. 2016. Development of a neutral cementitious material to promote vegetation concrete. *Construction and Building Materials* 127:442-449.
- Liqun, H., L. Yangyang, Z. Xiaolong, D. Shaowen, L. Zhuangzhuang, and H. Hao. 2017. Temperature characteristics of porous portland cement concrete during the hot summer Session. *Advances in Materials Science and Engineering* 2017:10.

- Macdonald, I. F., M. S. El-Sayed, K. Mow, and F. A. L. Dullien. 1979. Flow through porous media-the ergun equation revisited. *Industrial & Engineering Chemistry Fundamentals* 18(3):199-208.
- Mahadevan, J., M. M. Sharma, and Y. C. Yortsos. 2006. Flow-through drying of porous media. *AIChE Journal* 52(7):2367-2380.
- Mahmoudi, Z., M. Johansen, J. Christiansen, and O. Hejlesen. 2014. Comparison Between One-Point Calibration and Two-Point Calibration Approaches in a Continuous Glucose Monitoring Algorithm. *Journal of diabetes science and technology* 8.
- Malab, S., A. Benaissa, S. E. Boundraa, and S. Aggoun. 2009. Drying kinetics of self-compacting concrete. *Turkish Journal of Engineering & Environmental Sciences* 33(2):135-145.
- Marolf, A., N. Neithalath, E. Sell, K. Wegner, W. Weiss, and J. Olek. 2004. Influence of aggregate size and gradation on acoustic absorption of enhanced porosity Concrete. *ACI Materials Journal* 101(1):82-91.
- Mehta, D., and M. C. Hawley. 1969. Wall effect in packed columns. *Industrial & Engineering Chemistry Process Design and Development* 8(2):280-282.
- Mishra, K., Y. Zhuge, and W. Karunasena. 2013. Clogging mechanism of permeable concrete: A review.
- Montes, F., and L. Haselbach. 2006. Measuring hydraulic conductivity in pervious concrete. *Environmental Engineering Science* 23(6):960-969.
- Mosthaf, K., R. Helmig, and D. Or. 2014. Modeling and analysis of evaporation processes from porous media on the REV scale. *Water Resources Research* 50(2):1059-1079.
- Neamitha, M., and T. M. Supraja. 2017. Influence of Water Cement Ratio and The Size of Aggregate on The Properties Of Pervious Concrete. *International Refereed Journal of Engineering and Science* 6(4):9-19.
- Neithalath, N., D. P. Bentz, and M. S. Sumanasooriya. 2010. Predicting the permeability of pervious concrete: Advances in characterization of pore structure and transport properties. *Concrete International* 32(5):35-40.

- Nowak, R. 2016. Estimation of viscous and inertial resistance coefficients for various heat sink configurations. *Procedia Engineering* 157:122-130.
- Oh, R.-O., S.-S. Cha, S.-Y. Park, H.-J. Lee, S.-W. Park, and C.-G. Park. 2014. Mechanical properties and water purification characteristics of natural jute fiber-reinforced non-cement alkali-activated porous vegetation blocks. *Paddy and Water Environment* 12(S1):149-156.
- Olkin, I. 1960. *Contributions to probability and statistics; essays in honor of Harold Hotelling*. Stanford studies in mathematics and statistics, 2. Stanford University Press, Stanford, Calif.
- Ostertagová, E., O. Ostertag, and J. Kováč. 2014. Methodology and Application of the Kruskal-Wallis Test. *Applied Mechanics and Materials* 611:115-120.
- Pacheco-Torgal, F., J. Castro-Gomes, and S. Jalali. 2008. Alkali-Activated Binders: A Review: Part 1. Historical Background, Terminology, Reaction Mechanisms and Hydration Products. *Construction and Building Materials* 22(7):1305-1314.
- Palacios, M., P. Banfill, and F. Puertas. 2008. Rheology and setting of alkali-activated slag pastes and mortars: Effect of organic admixture. *ACI Materials Journal* 105:140-148.
- Pan, Z., P. Z. Tao, Y. Cao, and R. Wuhrer. 2018. Measurement and prediction of thermal properties of alkali-activated fly ash/slag binders at elevated temperatures. *Materials and Structures* 51.
- Perre, P. 2010. Multiscale modeling of drying as a powerful extension of the macroscopic approach: Application to solid wood and biomass processing. *Drying Technology* 28:944-959.
- Piasta, W., and B. Zarzycki. 2017. The effect of cement paste volume and w/c ratio on shrinkage strain, water absorption and compressive strength of high performance concrete. *Construction and Building Materials* 140:395-402.
- Provis, J. L. 2018. Alkali-activated materials. *Cement and Concrete Research* 114:40-48.
- Provis, J. L., A. Palomo, and C. Shi. 2015. Advances in understanding alkali-activated materials. *Cement and Concrete Research* 78:110-125.
- Provis, J. L., and J. S. J. Van Deventer. 2014. *Alkali Activated Materials : State-of-the-Art Report, RILEM TC 224-AAM*. Springer, Dordrecht.

- Quinn, H. 2014. A reconciliation of packed column permeability data: Deconvoluting the Ergun papers. *Journal of Materials* 2014.
- Rasiah, S., J. Kaabi, A. Mohammad, and Singh. 2013. Permeability and drying of pervious concrete pavers.
- Rasiah, S., and S. Kassis. 2014. Effect of supplementary cementitious materials on the properties of pervious concrete with fixed porosity.
- Sabnis, G. M. 2016. *Green building with concrete: Sustainable design and construction*. Second edition. ed. CRC Press, Boca Raton.
- Sandoval, G. F. B., I. Galobardes, R. S. Teixeira, and B. M. Toralles. 2017. Comparison between the falling head and the constant head permeability tests to assess the permeability coefficient of sustainable Pervious Concretes. *Case Studies in Construction Materials* 7:317-328.
- Schulz, R., N. Ray, S. Zech, A. Rupp, and P. Knabner. 2019. Beyond Kozeny–Carman: Predicting the permeability in porous media. *Transport in Porous Media* 130(2):487-512.
- Šelih, J., A. C. M. Sousa, and T. W. Bremner. 1996. Moisture transport in initially fully saturated concrete during drying. *Transport in Porous Media* 24(1):81-106.
- Shapiro, S. S., and M. B. Wilk. 1965. An analysis of variance test for normality (complete samples). *Biometrika* 52(3-4):591-611.
- Shi, C., and R. L. Day. 1995. A calorimetric study of early hydration of alkali-slag cements. *Cement and Concrete Research* 25(6):1333-1346.
- Shi, C., P. V. Krivenko, and D. M. Roy. 2006. *Alkali-activated cements and concretes*. 1 ed. CRC Press.
- Shokri, N., P. Lehmann, and D. Or. 2010. Evaporation from layered porous media. *Journal of Geophysical Research: Solid Earth* 115(B6).
- Sobieski, W., and Q. Zhang. 2014. Sensitivity analysis of Kozeny-Carman and Ergun equations. *Technical Sciences* 17(3):235-248.

- Song, C., P. Wang, and H. A. Makse. 2008. A phase diagram for jammed matter. *Nature* 453(7195):629-632.
- Sudimac Budimir, S., N. D. Cukovic Ignjatovic, and D. M. Ignjatovic. 2018. Experimental study on reducing temperature using modular system for vegetation walls made of perlite concrete. *Thermal Science* 22:1059.
- Sun, Z., X. Lin, and A. Vollpracht. 2018. Pervious concrete made of alkali activated slag and geopolymers. *Construction and Building Materials* 189:797-803.
- Tang, W., E. Mohseni, and Z. Wang. 2018. Development of vegetation concrete technology for slope protection and greening. *Construction and Building Materials* 179:605-613.
- Tänzer, R., A. Buchwald, and D. Stephan. 2015. Effect of slag chemistry on the hydration of alkali-activated blast-furnace slag. *Materials and Structures* 48(3):629-641.
- Tashima, M. M., L. Soriano, M. V. Borrachero, J. Monzó, and J. PayÁ. 2013. Effect of curing time on microstructure and mechanical strength development of alkali activated binders based on vitreous calcium aluminosilicate (VCAS). *Bulletin of Materials Science* 36(2):245-249.
- Tomczak, M., and E. Tomczak. 2014. The need to report effect size estimates revisited. An overview of some recommended measures of effect size. 21:19-25.
- Tro, N. J., T. D. Fridgen, and L. Shaw. 2014. *Chemistry: A molecular approach*. Canadian ed. ed. Pearson Canada, Toronto.
- Tun Chi, F., Y. Weichung, C. Jiang Jhy, and H. Ran. 2014. The influence of aggregate size and binder material on the properties of pervious concrete. In *Advances in Materials Science and Engineering*.
- Turner, I., and A. S. Mujumdar. 1997. *Mathematical modeling and numerical techniques in drying technology*. Marcel Dekker, New York.
- Vinkler, M., and J. L. Vitek. 2016. Drying concrete: Experimental and numerical modeling. *Journal of Materials in Civil Engineering* 28(9):04016070.

- Wang, S.-D. 2000. Alkali-activated slag: Hydration process and development of microstructure. *Advances in Cement Research* 12(4):163-172.
- Wang, S.-D., X.-C. Pu, K. L. Scrivener, and P. L. Pratt. 1995. Alkali-activated slag cement and concrete: a review of properties and problems. *Advances in Cement Research* 7(27):93-102.
- Welch, B. L. 1951. On the comparison of several mean values: An alternative approach. *Biometrika* 38(3/4):330-336.
- Winnefeld, F., M. Ben Haha, G. Le Saout, M. Costoya, S.-C. Ko, and B. Lothenbach. 2014. Influence of slag composition on the hydration of alkali-activated slags. *Journal of Sustainable Cement-Based Materials* 4.
- Xi, F., S. J. Davis, P. Ciais, D. Crawford-Brown, D. Guan, C. Pade, T. Shi, M. Syddall, J. Lv, L. Ji, L. Bing, J. Wang, W. Wei, K.-H. Yang, B. Lagerblad, I. Galan, C. Andrade, Y. Zhang, and Z. Liu. 2016. Substantial global carbon uptake by cement carbonation. *Nature Geoscience* 9(12):880-883.
- Xiao, J., L. Tong, C. Deng, P. Bénard, and R. Chahine. 2010. Simulation of heat and mass transfer in activated carbon tank for hydrogen storage. *International Journal of Hydrogen Energy* 35(15):8106-8116.
- Xu, P., A. P. Sasmito, and A. S. Mujumdar. 2019. *Heat and mass transfer in drying of porous media*. CRC Press.
- Yang, H., R. Liu, Z. Zheng, H. Liu, Y. Gao, and Y. Liu. 2018. Experimental study on permeability of concrete. *IOP Conference Series: Earth and Environmental Science* 108(2):022067.
- Yang, K.-H., A.-R. Cho, and J.-K. Song. 2012. Effect of water-binder ratio on the mechanical properties of calcium hydroxide-based alkali-activated slag concrete. *Construction and Building Materials* 29:504-511.
- Yinghong, Q., Y. Haifeng, D. Zhiheng, and H. Jiang. 2015. Water permeability of pervious concrete is dependent on the applied pressure and testing methods. In *Advances in Materials Science and Engineering*.

- Yoon, S., D. E. Macphee, and M. S. Imbabi. 2014. Estimation of the thermal properties of hardened cement paste on the basis of guarded heat flow meter measurements. *Thermochimica Acta* 588:1-10.
- Zami-Pierre, F., R. de Loubens, M. Quintard, and Y. Davit. 2016. Transition in the flow of power-law fluids through isotropic porous media. *Phys Rev Lett* 117(7):074502.
- Zhao, M., Y. Jia, L. Yuan, J. Qiu, and C. Xie. 2019. Experimental study on the vegetation characteristics of biochar-modified vegetation concrete. *JCBM Construction and Building Materials* 206:321-328.
- Zhong, R., and K. Wille. 2016. Compression response of normal and high strength pervious concrete. *Construction and Building Materials* 109:177-187.
- Zhong, R., M. Xu, R. Vieira Netto, and K. Wille. 2016. Influence of pore tortuosity on hydraulic conductivity of pervious concrete: Characterization and modeling. *Construction and Building Materials* 125:1158-1168.
- Zhou, J.-Q., Y.-F. Chen, L. Wang, and M. B. Cardenas. 2019. Universal relationship between viscous and inertial permeability of geologic porous media. *Geophysical Research Letters* 46(3):1441-1448.

Appendix

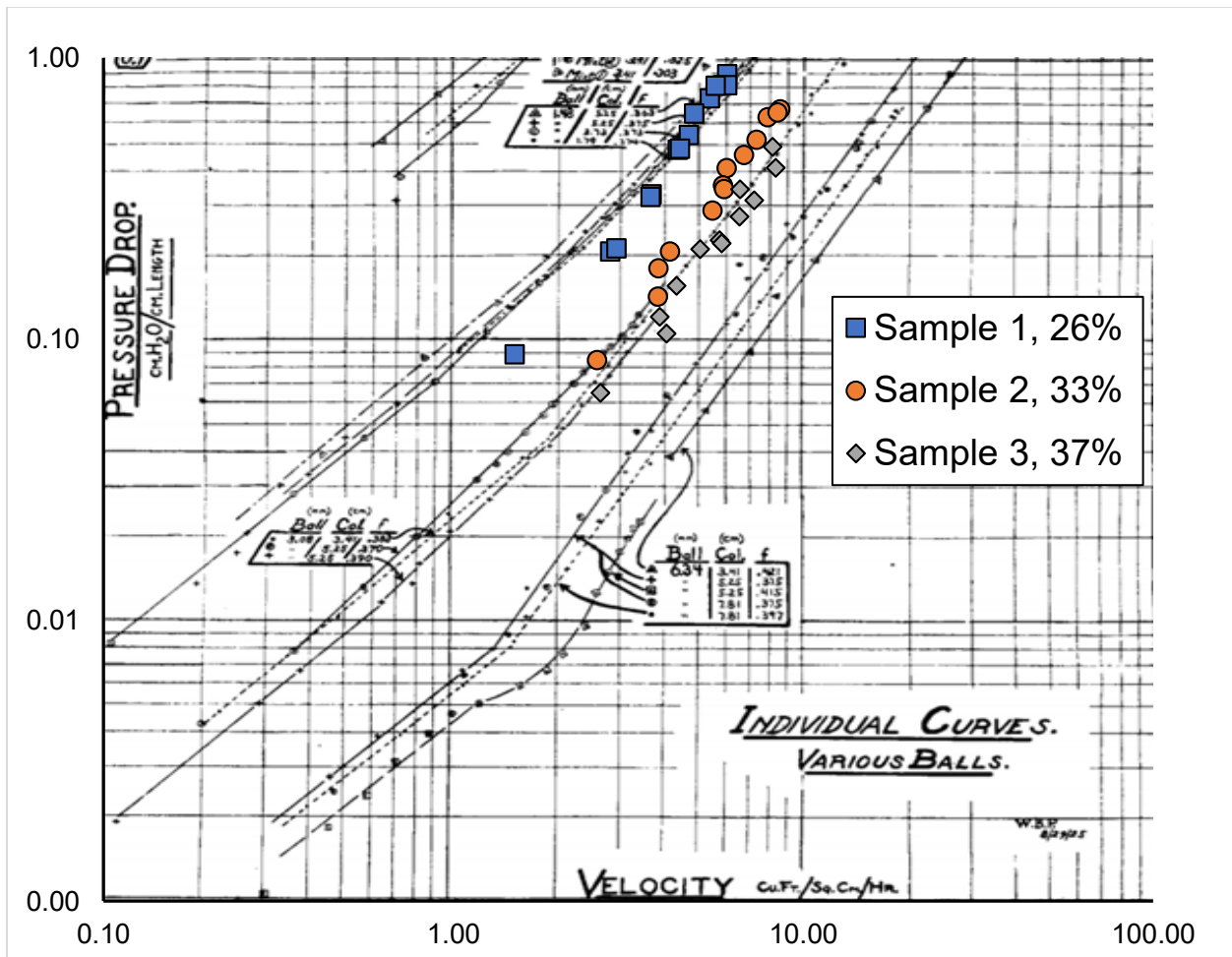


Figure A.1: Comparison of permeabilities obtained for various mixes of porous concretes to published values for sphere packs. Porous concretes made with 2 - 3.2 mm quartz aggregate (Quarzsand, 2 - 3.2mm, Carlo Bernasconi AG, Berne, Switzerland) overlaid on data of sphere packed columns. Sample 3 having a porosity of 37 % behaved as a packed bed of lead shot having 3 mm diameter. When the porosity was reduced to 26 % (due to additional binder content in mix) the slab had a permeability akin to 1.5 mm diameter sphere packs.

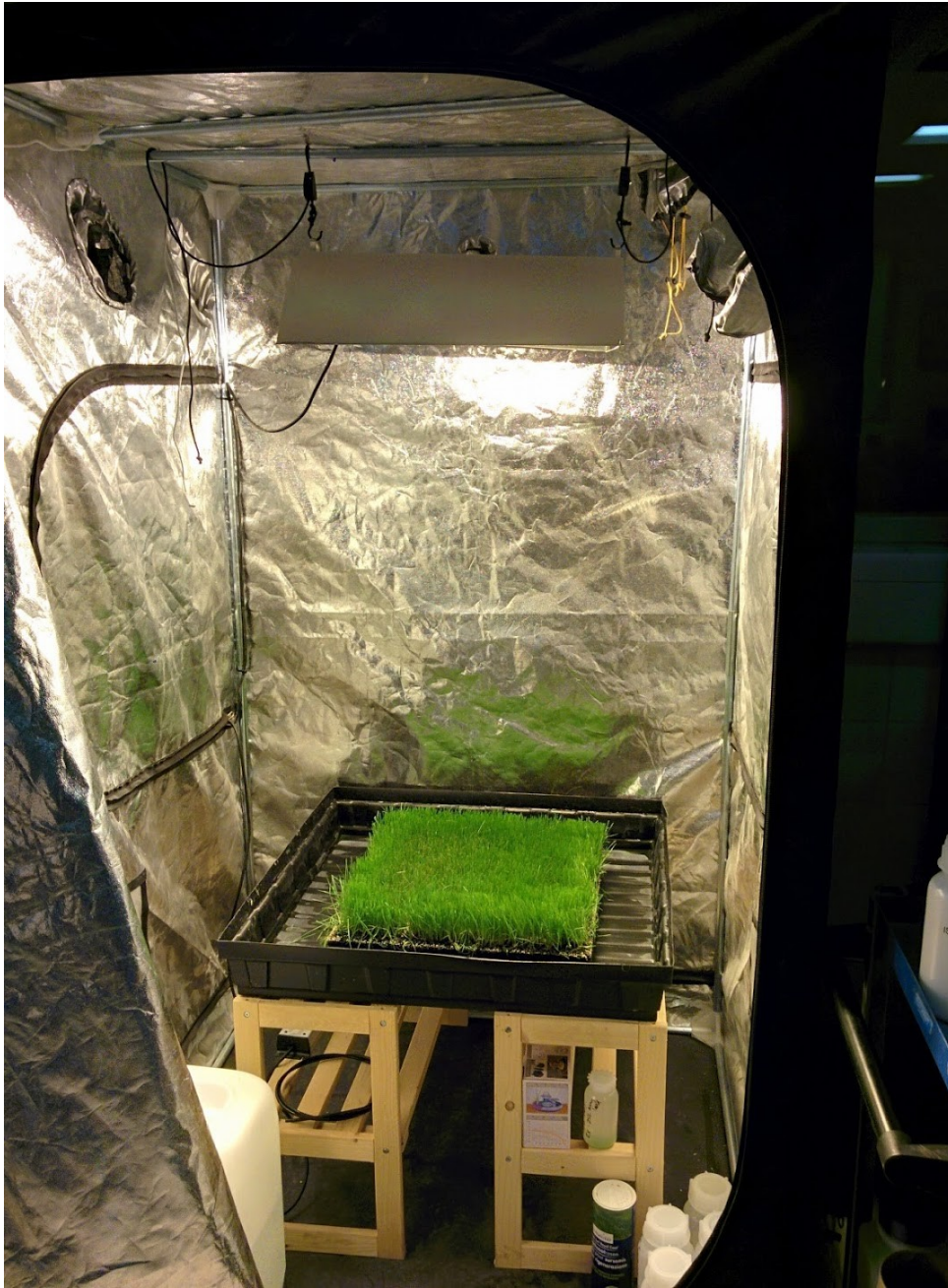


Figure A.2: Experimental setup for the growth of grass on porous concrete.

	N	Mean	Std. Deviation	Std. Error	95% Confidence Interval for Mean		Minimum	Maximum
					Lower Bound	Upper Bound		
Porosity	.25	.3840	.00721	.00416	.3661	.4019	.38	.39
	.35	.3187	.04609	.02661	.2042	.4332	.27	.36
	Total	.3513	.04638	.01893	.3027	.4000	.27	.39
Inertial Resistance Factor (m ⁻¹)	.25	27873	7998	4618	8005	47742	19456	35373
	.35	52923	5759	3325	38618	67229	47290	58800
	Total	40398	15070	6152	24583	56213	19456	58800
Viscous Inertial Resistance Factor (m ⁻²)	.25	767000000	126360595	72954324	453102880	1080897120	7E+8	9E+8
	.35	2053000000	120216347	69406940	-93333960	503933960	88900000	3E+8
	Total	4861500000	326832763	133428917	143160050	829139950	88900000	9E+8
Density (kg m ⁻³)	.25	1727	107	62	1461	1992	1606	1810
	.35	1661	41	24	1559	1763	1624	1705
	Total	1694	81	33	1609	1779	1606	1810

Table A.1: Descriptive statistics for alkali activated porous concrete cylinders made using different water to binder ratios. Analysis performed using SPSS (IBM SPSS Statistics, 23, IBM, New York, United States).

Porosity	Between Groups	.006	1	.006	5.884	.072
	Within Groups	.004	4	.001		
	Total	.011	5			
Inertial Resistance Factor(m^{-1})	Between Groups	941253750	1	941253750	19.381	.012
	Within Groups	194267479	4	48566869		
	Total	1135521229	5			
Viscous Inertial Resistance Factor (m^{-2})	Between Groups	473260335E+9	1	473260335E+9	31.116	.005
	Within Groups	60837940E+9	4	15209485E+9		
	Total	534098275E+9	5			
Density ($kg\ m^{-3}$)	Between Groups	6456	1	6456	.984	.377
	Within Groups	26236	4	6559		
	Total	32692	5			

Table A.2: One-way analysis of variance (ANOVA) for alkali activated porous concrete cylinders made using different water to binder ratios. Analysis performed using SPSS (IBM SPSS Statistics, 23, IBM, New York, United States).

Average cross-sectional velocity (m s ⁻¹)	Pa m ⁻¹	Sample label
0.29	3200	1
0.37	5200	1
0.43	7000	1
0.47	7820	1
0.48	8540	1
0.22	2000	1
0.29	3120	1
0.35	4600	1
0.48	7800	1
0.23	2050	1
0.35	4640	1
0.39	6200	1
0.44	7760	1
0.2	820	2
0.33	2000	2
0.44	2800	2
0.48	3960	2
0.3	1740	2
0.47	3440	2
0.3	1380	2
0.47	3330	2
0.21	628.6	3
0.34	1514.3	3
0.4	2042.9	3
0.31	1171.4	3
0.45	2200	3
0.32	1021.4	3

Table A3: Data used in Chapter 3 to conduct the independent-samples Kruskal-Wallis test.

	Mix	Shapiro-Wilk		
		Statistic	df	Sig.
Porosity	.25	.942	3	.537
	.35	.996	3	.880
Inertial resistance factor	.25	.990	3	.810
	.35	.999	3	.930
Viscous inertial resistance factor	.25	.932	3	.497
	.35	.997	3	.900
Density	.25	.995	3	.865
	.35	.983	3	.751

Table A.4: Shapiro-Wilk's tests of normality. The units for the viscous inertial resistance factor, the inertial resistance factor and density are m^{-2} and m^{-1} , and $kg\ m^{-3}$ respectively. Analysis performed using SPSS (IBM SPSS Statistics, 23, IBM, New York, United States)

List A.1: Solar heated porous concrete assumptions and calculations

The energy released from the experiments represented in Figure 6.3.1 was considered. The calculations describe the amount of energy involved in cooling sample 6 (Table 3.2.2) from 50 °C to 17 °C.

- No energy was transferred by radiation and no energy was transferred by conduction from the slab to the frame fastening it to the wind tunnel.
- The area perpendicular to the flow of air was equal to the surface area of the sample (0.25 m²).
- The air properties were constant at: $\rho = \text{density}_{\text{air}} \sim 1.2 \text{ kg m}^{-3}$; Isobaric heat capacity of air ($c_{p_{\text{air}}}$) $\sim 1.0 \text{ kJ kg}^{-1} \text{ K}^{-1}$.
- There was a constant inlet air velocity 0.80 m s⁻¹. The volumetric flow rate was equal to the area perpendicular times the constant inlet air velocity: 0.2 m³ s⁻¹.
- The mass flow rate was defined as follows: $\dot{m} = \lim_{\Delta t \rightarrow 0} \frac{\Delta m}{\Delta t} = \frac{dm}{dt}$ where: \dot{m} = mass flow rate (kg s⁻¹); m = mass (kg); t = time (s).
- $\dot{m} = \text{volumetric flow rate} * \rho = 0.2 \text{ m}^3 \text{ s}^{-1} * 1.2 \text{ kg m}^{-3} = 0.24 \text{ kg s}^{-1}$.
- The centerline temperature of the air (5 centimeters away from the slab) was considered as the average for all the fluid flowing through at a given moment in time.
- The quartz aggregate had a heat capacity $\sim 0.730 \text{ kJ kg}^{-1} \text{ K}^{-1}$ (Hemingway, 1987).
- The hydrated cement's specific heat capacity was $\sim 1.28 \text{ kJ kg}^{-1} \text{ K}^{-1}$ (Yoon et al., 2014).
- The alkali activated slag's specific heat capacity was $\sim 2.5 \text{ kJ kg}^{-1} \text{ K}^{-1}$ (Pan et al., 2018).
- The volume of the slab was 0.0125 m³
- The mass of binder (alkali activated slag (ECOCEM, France)) was 1.40 kg.
- The mass of aggregate was 18.9 kg.
- The time period of interest (figure 21) was modeled as a function.
- The integral from time t_0 to t_{870s} was equal to 2417 $\text{deltat} * dt$ (where $\text{deltat} = \text{outlet}_{\text{temperature}} - \text{inlet}_{\text{temperature}}$).

The energy released could then be calculated as follows: $\text{Energy}_{\text{released}} = 0.24 \text{ kg s}^{-1} * 1.0 \text{ kJ kg}^{-1} \text{ K}^{-1} * 2417 \text{ deltaT dt} = 580 \text{ kJ}$

This can also be calculated from the slab's physical properties and temperature using their specific heat capacity as follows:

Temperature at the beginning $t_{\text{slab}_0} = 50 \text{ °C}$ and at the end $t_{\text{slab}_f} = 17 \text{ °C}$.

Change in energy of the slab = $(0.730 \text{ kJ kg}^{-1} \text{ °C}^{-1}) * 18.9 \text{ kg} + 2.5 (\text{kJ kg}^{-1} \text{ °C}^{-1}) * 1.4 \text{ kg} * (50 \text{ °C} - 17 \text{ °C}) = 570 \text{ kJ}$.